# Semiannual Technical Summary

Seismic Discrimination

31 December 1972

Prepared for the Advanced Research Projects Agency
under Electronic Systems Division Contract F19628-73-C-0002 by

Lincoln Laboratory

MASSACHUSETTS INSTITUTE OF TECHNOLOGY

LEXINGTON, MASSACHUSETTS
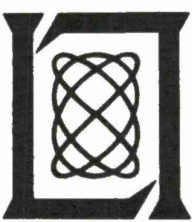
MASSACHUSETTS INSTITUTE OF TECHNOLOGY

LINCOLN LABORATORY

SEISMIC DISCRIMINATION

SEMIANNUAL TECHNICAL SUMMARY REPORT
TO THE
ADVANCED RESEARCH PROJECTS AGENCY

1 JULY – 31 DECEMBER 1972

ISSUED 2 MARCH 1973

LEXINGTON   MASSACHUSETTS

ABSTRACT

Studies of new array data are reported, with particular emphasis
on the array NORSAR. Models for approach angle anomalies at
LASA are presented. Further evidence for deep mantle lateral
heterogeneity is given. Detailed analyses have been made of
earthquakes in Eurasia. A microbarographic noise study has
been completed. Continued progress is reported in the bulletin
production from the month of intensive seismic analysis.

CONTENTS

SUMMARY

This is the eighteenth Semiannual Technical Summary report of the Lincoln Laboratory Seismic Discrimination Group. Our work is aimed at the solution of seismological problems concerned with the detection, location and identification of seismic events in order to provide technological background that would be needed in discussions of a test-ban treaty. We have rapid access to digital data from the large arrays LASA, NORSAR and ALPA in addition to film data from the World-Wide Network.

NORSAR has now been in full operation for more than a year and we have devoted considerable effort to studying its short period P-wave characteristics. These include a greater degree of incoherence and amplitude fluctuation from site to site than is observed at LASA. Our first concern has been to accumulate a sufficient body of data to see whether there are any clear patterns to these fluctuations. It seems at first sight that there are not. Evidence is presented that sources relatively close to one another have substantially different amplitude patterns across NORSAR. We foresee that an important effort in the near future will be an attempt to determine the extent to which fluctuations can be modeled in a geophysically satisfying way. Many seismic source regions are within 30° of NORSAR, and accurate location of these requires a good understanding of the $dT/d\Delta$ curve in this range. This is the distance range, however, for which we expect most variability owing to crustal and upper mantle lateral heterogeneity. We report newly measured $dT/d\Delta$ values in this range and remark on the similarity of the curve to that for Western North America.

Work is in progress on the time delays within subarrays at NORSAR. This is to consider the problem of whether beaming within individual subarrays needs to be more sophisticated than a simple plane wave approach.

Collaboration with the scientific staff of NORSAR continues at a high level. The most recent visitor to NORSAR, Mr. Sheppard, is now in the process of compiling an extensive set of time corrections for subarrays of NORSAR. This will be important for two reasons: (1) it will contribute to the refinement of locations with NORSAR and (2) it will enable us to search for the sort of propagation anomalies which were found at LASA and associated with heterogeneity in the middle and deep mantle.

If anisotropy in elastic properties exists in the crust and upper mantle — a frequent conjecture as yet only sparsely documented — it might be possible to use an array to look at surface wave velocity variability as a function of azimuth. A search has been made for anisotropy both at LASA and NORSAR, but the results so far emphasize the very serious problem of separating anisotropy from heterogeneity both within the array and beyond it. Frequency dependence of the approach angle of Rayleigh waves to LASA is associated with continental complexity to the west of the array.

An attempt is reported to invert the large set of ($dT/d\Delta$, Azimuth) data collected from individual subarrays at LASA by placing a highly corrugated interface at depth. This surface cannot be ascribed to any particular depth beneath the array, but if it were associated with the Moho it could be mapped out in an approximate form.

An alternative approach to the problem of interpreting this data set is to treat the scatter in the data as being indicative of a medium with scattering properties describable by a Chernov-type model. This technique is demonstrated and it is shown how certain parameters of a random medium could be inferred from the data. Further, the impact of a random element on seismic

array techniques for event location is discussed. Some events at LASA appear more coherent than others, and in one particular case of an incoherent event we have been able to identify two separate P-waves arriving simultaneously at the array from substantially divergent directions. We believe that this multipathing evidence, rather similar to that obtained some time ago for Rayleigh waves, may lead us to further interpretation of the middle mantle as a laterally heterogeneous medium. Work has advanced on an extensive travel time survey of the mantle using deep focus earthquakes. It is possible to map some regions of the mantle, particularly near the core boundary, which have seismic velocities differing significantly from the mean. A study has been completed of the contribution of S-waves to the coda of a P arrival. It has been possible to infer a structure (probably at the sediment-hard rock interface) which could generate such P-S converted energy.

A survey of focal mechanisms of Eurasian earthquakes is under way. This, it is hoped, will give us a clearer understanding of the events against which we have to discriminate in that region. It may also assist us in the explanation of so-called "anomalous" events which fail the $M_s:m_b$ discriminant. Our initial results highlight the extraordinary diversity of mechanisms away from well-defined plate boundaries. A special study has been completed of a large Persian earthquake for which parameters such as stress drop, dimensions and slip could be inferred. Also reported are the statistics of a major earthquake swarm for which many singular properties have been noted. Comparison is made of the energy release time profile with recent work of Knopoff on stochastic seismicity. A deep focus earthquake in the Hindu Kush region has been examined for its rather unusual suppression of the depth phase pP. Without this phase, there would be grounds for suspicion over this event, but the long period phase sP helps to confirm the network-determined depth. Further examination of a Siberian earthquake by means of time-domain analysis of WWSSN seismograms is described.

Work on the correlation between microbarographic and long period seismic noise has been completed. It is possible to suppress seismic noise by several dBs with cross-correlation techniques, but doing this on a routine basis requires continued re-evaluation of cross correlation functions as the coupling between atmosphere and ground is dependent on wind speed and direction. Burial of instruments at 200 m may be in the long run a more economical way of suppressing this noise. The question of optimal monitoring of surface waves at distances of less than 20 degrees is under consideration. We report signal and noise characteristics at LASA when explosions at NTS are observed. At this distance (12°) the signal-to-noise ratio appears relatively constant from 12 to 20 seconds.

Work on the International Seismic Month continues to progress. At the moment, we are examining in great detail the detection logs of the LASA and NORSAR arrays in conjunction with all other single station data in order to look for credible events to add to our present bulletin. Substantial interactive computer aid is now provided by a new system called DADS modeled on our experience with the display console.

Finally, we report two more general seismological studies performed in the laboratory in the last 6 months. A study of core reflections PcP has shown the constraints within which core/mantle boundary models must lie. Work on free oscillation has shown the value of using the focal mechanism of an earthquake in extracting spectral peaks. Comparison of peaks from the Alaskan and Colombian quakes shows systematic and significant divergences which probably have to be associated with mantle heterogeneity.

<div align="right">D. Davies</div>

GLOSSARY

ALPA	Alaskan Long-Period Array
CGS	United States Coast and Geodetic Survey
DADS	Data Analysis and Display System
LASA	Large Aperture Seismic Array, Montana
ISM	International Seismic Month
NORSAR	Norwegian Seismic Array
NOS	National Ocean Survey
NTS	Nevada Test Site
SATS	Semiannual Technical Summary
WWSSN	World-Wide Standard Seismographic Network
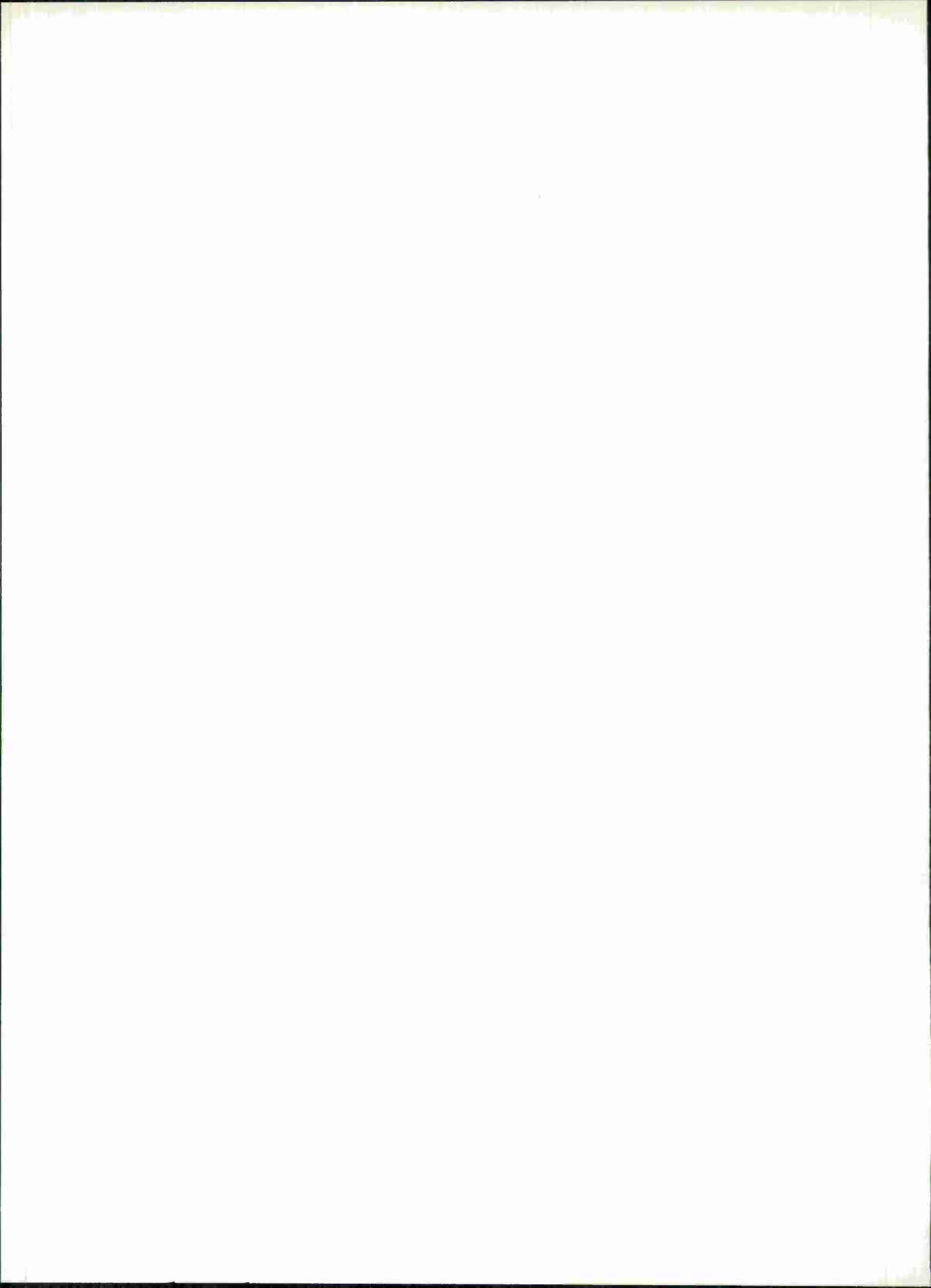
I. ARRAY STUDIES

A. SHORT-PERIOD AMPLITUDE AND WAVEFORM STUDIES AT NORSAR

Variations of short period amplitudes and waveforms across NORSAR are being studied as part of the NORSAR evaluation program. Although the data are complex and often inconsistent, some general conclusions can be made.

Examination of individual sensors within subarrays shows that subarray amplitudes are controlled by the amount of complex scattering of incoming waves by the crust under NORSAR. Subarrays which have high amplitudes have coherent waveforms within each subarray. Low amplitude subarrays on the other hand often have incoherent waveforms with complex multiple arrivals in the waveform codas. Interestingly enough, on both low and high amplitude subarrays, the center seismometer trace is often very coherent with the steered subarray beam. This suggests that center sensors can be used in place of subarray beams for routine seismic analysis of events, provided the signal-to-noise ratio (SNR) is adequate.

TABLE I-1

EVENTS USED IN NORSAR SHORT-PERIOD STUDY

Event	Date	Origin Time (GMT)	Region	Azimuth (deg)	Distance (deg)	Depth (km)	Magnitude (m_b)
1	2-21-72	19:34:50	Alaska Peninsula	−6.2	63.3	60D	5.7
2	8-16-71	04:58:00	Szechwan Province	71.8	67.1	33N	5.5
3	6-30-71	03:56:57	Eastern Kazakh	73.2	39.0	0G	5.4
4	5-25-71	04:02:58	Eastern Kazakh	74.0	38.7	0G	5.2
5	6-15-71	22:15:50	Kirgiz-Sinkiang border region	82.0	45.3	33N	5.1
6	8-4-71	01:59:03	Hindu Kush	93.7	44.8	206	5.0
7	6-26-71	22:23:29	Afghanistan-USSR border region	94.7	44.9	127	5.0

Here we give an example of these results for a high frequency, impulsive event, a presumed explosion in Eastern Kazakh, on 25 May 1971, with origin time 04:02:58 GMT. Other data for this event are given in Table I-1. P-wave beams at each subarray were formed by aligning the individual sensors. The peak-to-trough beam amplitudes (A/T) were measured and normalized by their geometric mean across NORSAR. These amplitudes are plotted in dB relative to their geometric mean in Fig. I-1. Center sensor amplitudes are also plotted relative to their geometric mean. In spite of a variation of 20 dB, that is, an amplitude fluctuation of 10, across the whole NORSAR, the center sensors are nearly always within 1 or 2 dB of the beam amplitudes. Also shown in Fig. I-1 is the SNR at 2 Hz measured for each subarray beam. The fact that the

1

SNR pattern closely follows the signal amplitude pattern demonstrates that true P-wave fluctuations are being measured, not problems with seismometer gain or coupling with the ground. For this event, subarrays which have high amplitudes, such as 4C and 6C, have very coherent signals within each subarray. Figure I-2 shows the individual sensors and subarray beams for 4C and 6C, as examples. Figure I-3 shows similar traces of two, low-amplitude subarrays, 7B and 8C. Within each subarray the relative gains of single sensors and beams are preserved.

There are significant differences between the high and low amplitude subarrays shown here. The individual traces of 4C and 6C in Fig. I-2 are very coherent with rapidly decaying codas in the 5.0-sec window indicated. The first arrivals are impulsive and the largest in the window. The first arrivals on subarrays 7B and 8C in Fig. I-3 are weak and the codas very complex showing distinct multiple arrivals with different phase velocities from the first motions. This suggests that the waves have been backscattered by complex inhomogeneities under the array, the energy being distributed among complex arrivals in the coda. The center sensors, 7B0 and 6C0, correlate quite well with the corresponding subarray beams. Correlation coefficients were computed between individual sensors and the subarray beams using 5 sec of data. Over the frequency band 1.5 to 3.5 Hz, 7B0 and the 7B beam have a correlation coefficient of 0.89, whereas 8C0 and the 8C beam have a correlation coefficient of 0.87. Other sensors have correlation coefficients as low as 0.31 with the subarray beam. This indicates that the arrivals in the coda are correlated over at least the spacing between subarray sensors (~3 km), and that, qualitatively, center sensors can be taken as approximations to the subarray beam.

Under this assumption, amplitude fluctuations for seven events were measured using the center sensors. These events are listed clockwise by azimuth in Table I-1. Except for event 1, the azimuths sample a narrow sector which includes the Eastern Kazakh test site in the USSR. Amplitudes were measured and divided by the geometric mean of each event over the whole array. Steered beams across NORSAR are displayed in Fig. I-4, to indicate the variety of complexity and period of the events.

Figures I-5 through -11 are contour maps of amplitude fluctuation across NORSAR for the seven events. The amplitudes are contoured in dB above the geometric mean of each event, with a contour interval of 2 dB. Superposed on each map is an arrow which extends from the 1A subarray along the event azimuth.

The most interesting feature of these maps is the pocket of low amplitudes which appears on all but two of the contour maps. This pocket moves about over NORSAR for different events, which suggests that it may be caused by inhomogeneities deep in the crust or upper mantle, at least several times deeper than the distance between subarrays. However, if we put a hypothetical obstacle at depth to block out and scatter the incoming waves, the movement of the low amplitude pattern with azimuth does not seem to be consistent for these events. Another difficulty is the consistency of amplitude patterns for events with equal azimuths. Figures I-10 and -11 show contour maps for two Hindu Kush events which differ in depth by more than 100 km. The amplitude patterns are quite similar, event 7 in Fig. I-11 showing a slightly deeper pocket than event 6 in Fig. I-10. Each event shows a consistent increase in amplitude of at least 15 dB from subarrays 1A to 3C, in the northeasterly direction. Since the two events have different depths, the amplitude patterns must be associated with structure under NORSAR, rather than source variations.

Lacoss[1] analyzed a large population of beamed subarray amplitudes generated by the Event Processor at NORSAR. One important conclusion of the study was that the large amplitude fluctuations across NORSAR are often, but not always, repeatable for events from the same region.

As a counter example, the two presumed explosions, events 3 and 4, in Figs. I-7 and -8, respectively, do <u>not</u> give similar amplitude fluctuations, in spite of being very close in azimuth and distance from NORSAR. As shown in Fig. I-4, the beam for event 4 is high frequency and impulsive, and similar in frequency content to the Hindu Kush events. Except for subarrays 4C and 6C, which have high amplitudes, the contour map for event 4 is quite similar to those for events 6 and 7. Event 3, however, seems to have a complex, low frequency component in the source function, as shown in Fig. I-4. The amplitudes were measured on the second pulse, which seems to contain interfering pulses on single sensors. Clearly, amplitude patterns from such an event cannot be attributed only to structure under NORSAR.

Event 2 is a Chinese earthquake which has an azimuth close to that of events 3 and 4, but is 30° further away from NORSAR. The contour map for this event is shown in Fig. I-6. In this case, the low amplitude region is displaced to the north relative to the pattern of event 4 in Fig. I-8. This is not easily explained by the small difference in azimuth between the two events.

These examples illustrate the complexity of the amplitude fluctuations at NORSAR. Considerably more data must be examined before the causes of the fluctuations can be systematically described or explained.

<div align="right">C. W. Frasier</div>

B. $\frac{dT}{d\Delta}$ MEASUREMENTS USING NORSAR IN THE DISTANCE RANGE FROM 0 to 30°

In order to use NORSAR to detect and locate events in the western Soviet Union, it is necessary to use P-waves recorded at distances less than 30°, which are subject to various complications caused by the fact that the travel time curve is multi-valued and regionally varying. Failure to account for these effects will lead to large location errors and could even cause one event to be mistaken for several events in different places. Therefore, we have begun "calibrating" the upper mantle in the vicinity of NORSAR by making dT/dΔ measurements for P waves at distances less than 30°. Figure I-12 shows the data obtained so far, together with the data measured by Johnson[2] using the extended Tonto Forest array in Arizona, and a theoretical curve appropriate to western North America. No attempt has been made to apply any corrections for the effects of the structure beneath the array. This will be done, and azimuth as well as dT/dΔ anomalies will be considered, after more measurements have been made.

Already, it is apparent that the structure of the upper mantle is not grossly different in Europe than it is in western North America. The only obvious anomalies in the NORSAR data are low dT/dΔ values between 1000 and 2000 km, probably indicative of higher velocities in the upper 250 km in Scandinavia, and a few scattered points between 9 and 10 sec/deg (where the North American data are sparse). When a greater number of data have been analyzed at greater length, smaller scale structural details may emerge.

<div align="right">B. R. Julian</div>

C. TIME DELAYS WITHIN NORSAR SUBARRAYS

There are at least two important respects in which short period P-wave data recorded at NORSAR differ from those recorded at LASA: much higher frequencies are often observed and events of interest are often much closer to the array. NORSAR's "window" for high frequencies is potentially one of its most valuable characteristics, but in order to take advantage of it, time corrections for the individual sensors must be accurately known. Otherwise, the high frequencies may be degraded by the process of beamforming. This is obviously true for the array as a whole, but it is less clear whether delays within individual subarrays also need to be considered.

<div align="center">3</div>

Figure I-13 illustrates that they do, at least in some cases. It shows beams of the P wave from a deep Hindu Kush earthquake formed using a single subarray (2B), using both hand-picked time delays and delays calculated assuming a plane wavefront with the velocity and azimuth determined by fitting the arrival times at all the subarrays. The second beam has clearly distorted the waveform to an extent which could hamper its usefulness in source mechanism studies.

In order to determine the seriousness of this problem, time delays have been measured at all NORSAR sensors for 12 events with clearly recorded, impulsive P waves. The distribution of these signals in slowness space (Fig. I-14) was chosen to be as wide as possible, so that the variations in the delays would be extreme.

Figure I-15 shows the expected spectral loss caused by beamforming as a function of the root-mean-square (rms) time error. It illustrates, for example, that if we wish the degradation of the signal to be less than 5 dB at all frequencies less than 5 Hz, then the rms time error must be 0.03 sec, or less. (This calculation is based upon the assumption that the signals from the individual sensors are identical. In reality, incoherence would unavoidably degrade real signals even further.) Since short-period NORSAR data are digitized at 0.05 sec intervals, under the best imaginable circumstances timing errors would be approximately uniformly distributed between −0.025 and +0.025 sec and the rms error would be slightly less than 0.015 sec.

The distribution of the rms errors determined from the measured times is given by the histogram in Fig. I-16(a). Roughly half the sensors have rms errors greater than 0.04 sec, so it is clear that some sort of time corrections are needed if full advantage is to be taken of high frequency signals. Figure I-16(b) shows the improvement in distribution which can be obtained by using a constant time correction (independent of velocity and azimuth) for each sensor. Still nearly 40 percent of the sensors have rms errors exceeding 0.04 sec. The improvement which may be gained with distance and azimuth dependent corrections is presently being investigated.

<div style="text-align: right;">B. R. Julian</div>

D. EVALUATION OF NORSAR TIME ANOMALIES

A data base for the study of the NORSAR P-wave time anomalies has been collected. These data were collected from plotted outputs of the event processor runs at NORSAR between mid 1971 and mid 1972. The initial selected population consisted of all events reported, both on the PDE cards and on the NORSAR station bulletins, with a quality rating of 1 or 2. From this group of over 1600 events, a final data base of 721 events was chosen as meeting recording quality for reliable delays. Each event in the initial group was examined for proper delays, as recorded in the subarray beam alignment on the output plots of the event processor. If any errors in alignment were observable on the plots, then these data were corrected before punching the data on cards. The data recorded on cards include all event information and array delays. In this manner, a collection of events recorded at NORSAR over a 13 month period was examined, corrected and punched on cards that now consist of the data base for NORSAR subarray time anomaly study.

Since 60 percent of these events in the final population need some corrections made to the delays determined by the event processor, the entire data base has been entered into the DADS system reported in Sec. V-B. This system has features which will facilitate the updating of corrections required for the population. Additional events will be added as soon as sufficient numbers of NORSAR event recordings are received.

<div style="text-align: right;">R. M. Sheppard</div>

E.   CHARACTERISTICS OF 10 TO 40 SECOND RAYLEIGH WAVES
     AT LASA AND NORSAR

The frequency-wavenumber spectra of vertical, long-period LASA and NORSAR recordings
of Rayleigh waves have been computed to determine the propagation effects due to crustal struc-
ture along the paths to and beneath the arrays.   High resolution analysis[3] was used to obtain
the greater angular resolution and accuracy that the method provides over standard techniques.
Phase velocity curves for both arrays were determined.   Lateral refraction as a function of
wavelength for the path NTS to LASA was examined.   Velocity anisotropy of the crust beneath
NORSAR was investigated.   Multipaths from various epicenters to NORSAR were also determined.

The data base for LASA is presented in Table I-2.   It is composed of seven NTS explosions
and two regional earthquakes.   More detailed information on the explosions may be found in
Springer and Kinnaman.[4]   The explosions were chosen because they have virtually identical epi-
centers, thus propagation effects between NTS and LASA could be detailed.   The two earthquakes
were added to complete the measurement of the local phase velocity curve.   The data base for
NORSAR is presented in Table I-3.   These events were picked because they are well distributed
in azimuth, thus the effect of the structure beneath this array could be determined.

For each event, a high resolution horizontal wavenumber power spectrum at a set of periods
spanning the 10- to 40-sec band was computed and contoured.   The wavenumber where the peak
(or peaks in cases of multipathing) of the spectrum occurred was determined, yielding the azimuth
and phase velocity of the particular period component of the Rayleigh wave.   Care was taken in
excluding windowed energy from neighboring periods with higher power making use of the sensi-
tivity function of the filter used to isolate the period under study.   The peak wavenumber was
chosen to be at the geometrical center of the 2-dB contour.   The local maximum point in the
wavenumber spectrum always fell within one differential wavenumber unit of the chosen point.

Table I-4 presents the phase velocity data for LASA and NORSAR.   Each point represents
the average of 9 values for LASA and 6 values for NORSAR.   Accuracy is a function of period,
being about ±0.05 for short periods and monotonically increasing to ±0.1 for longer periods.
Figure I-17 is a plot of the LASA values superimposed on average curves for mid-continent and
basin-range structures.[5]   The jump in the curve near 20 sec indicates a rise in the shear veloc-
ity in the middle crust.   Otherwise, the curve tends to average the basin-range and mid-continent
curves.   Figure I-18 gives the NORSAR curve plotted with an average shield curve[5] and a curve
for Finland.[6]   The most distinctive feature is the dip in phase velocity near 35 sec.   Waves with
this period sense the uppermost mantle so that lower than normal shield shear velocities may
exist there.   The NORSAR area does deviate from most shield areas in that a Permian pluton
fills the large Oslo graben on which the array is partially located.   In general, these data deter-
mined for NORSAR and LASA, represent the highly accurate measurements that can be made
over relatively short paths (LASA spans approximately one wavelength of a 40-sec Rayleigh wave)
by combining direct digital recording of an array of identical instruments with numerical
techniques.

Julian[1] has demonstrated via ray-theoretical calculations how surface waves will be re-
fracted by lateral inhomogeneities in the crust.   The path between NTS and LASA is geologically
complicated in that it passes near to or within the Great Nevada Basin, the Snake River Down-
warp and the Colorado Plateau.   Each of these geologic provinces has different velocity struc-
tures[7] so that the transition zones may act as refractors to Rayleigh waves.   Further, any de-
flection of a Rayleigh-wave wavefront will be frequency dependent, since the velocity differences

5

TABLE I-2

DATA BASE FOR LASA RAYLEIGH-WAVE STUDY

Event	Date	Time (GMT)	Latitude (° N)	Longitude (° W)	Depth (km)	Distance (degs to LASA)	Azimuth	Location	Magnitude, m_b (NOS)
Earthquake	8-9-67	13:26:50	39.9	104.7	5	7	170	Denver	5.3
Zaza	9-27-67	17:00:00	37.1	116.1	0	12	221	Yucca	—
Earthquake	10-4-67	10:22:30	38.5	112.1	18	9	210	Utah	5.2
Lanpher	10-18-67	14:30:00	37.1	116.1	0	12	221	Yucca	—
Rickey	6-15-68	16:00:00	37.3	116.4	0	12	223	Pahute Mesa	—
Sled	8-29-68	22:45:00	37.3	116.4	0	12	223	Pahute Mesa	—
Purse	5-7-69	13:45:00	37.3	116.4	0	12	223	Pahute Mesa	5.8
Hutch	7-16-69	14:55:00	37.1	116.1	0	12	221	Yucca	5.6
Pipkin	10-8-69	14:30:00	37.3	116.4	0	12	223	Pahute Mesa	5.5

TABLE I-3

DATA BASE FOR NORSAR RAYLEIGH-WAVE STUDY

Date	Time (GMT)	Latitude (°N)	Longitude (°E)	Depth (km)	Distance (degs to NORSAR)	Azimuth (deg)	Location	Magnitude, m_b	
								NOS	NORSAR
6-15-71	22:15:50	41.4	79.2	N	44	85	Kirgiz, SSR	5.1	4.4
7-11-71	20:13:34	37.2	36.8	9	29	131	Turkey	5.2	4.4
12-7-71	12:04:57	55.1	−54.4	N	34	291	E. of Labrador	5.4	4.6
12-16-71	18:39:55	77.9	17.8	N	18	5	Svalbard Region	5.0	4.2
12-22-71	07:05:24	47.9	48.2	0	25	102	Western Kazakh	6.0	5.6
3-21-72	23:12:06	35.8	14.8	N	30	171	Mediterranean Sea	4.6	4.4

TABLE I-4

APPARENT PHASE VELOCITIES

Period (sec)	Phase Velocity (km/sec)	
	LASA	NORSAR
9	3.11	—
11	3.25	—
12	3.26	3.45
14	3.29	3.50
16	3.27	3.50
18	3.35	3.60
20	3.56	3.60
22	3.57	—
24	3.62	—
25	—	3.80
30	3.70	—
33	—	3.80
40	3.85	4.10

between provinces change with depth and different frequency Rayleigh waves are sensitive to different depths. Figure I-19 shows the azimuthal data as a function of period for the 7 NTS explosions. The two lines are the theoretical great circle azimuths to LASA from Pahute Mesa and Yucca Flat. The waves arrive about 10 degrees north of the great circle path at short periods, swinging gently to the south until the azimuth is about 10 degrees to the south of the theoretical path at longer periods. Such behavior is reasonable for a path that crosses a transition zone between two provinces, where the crust has an opposite phase velocity contrast for short period waves compared to longer period waves. In Fig. I-17 it is seen that the mid-continent and basin-range phase velocity curves merge at short periods with the mid-continent values higher at longer periods, thus the longer period waves should be pulled to the south as observed.

While lateral refraction of surface waves indicates laterally heterogeneous structure along the propagation path, the variation of phase velocity as a function of the azimuth of an event indicates heterogeneity beneath the array. Figure I-20 plots the azimuth of the arrival of the 20-sec component of the Rayleigh waves for the NORSAR events. Figure I-21 shows the measured phase velocity of 20- and 16-sec waves for the various azimuths. The peak in the power spectrum of all the events is near 20 sec, so that windowing has not influenced those measurements. The accuracy of the data is indicated by the scatter of the values at 16 sec. Thus, there appears to be a P-SV velocity anisotropy beneath the array. The amount is about 5 to 10 percent, which is comparable to the 7 percent found by Wickens and Pec[8] and Boore[9] for 40-sec Love waves (SH) on the Canadian shield. The most likely cause of anisotropy is the heterogeneous crustal structure beneath NORSAR.[10]

A final observation on Rayleigh waves concerns multipathing of the events recorded at NORSAR. Two of the events were scanned at 4 min after the initial Rayleigh wave arrival. The wavenumber spectra are given in Figs. I-22 and -23. The first part of each figure shows the initial arrival. The latter parts show later arrivals coming in at various azimuths. The arrival coming from the north in Fig. I-22 cannot be related to any crustal discontinuity. The LASA and

8

NORSAR bulletins contain no event which might have produced the wave. Therefore, it probably comes from the original event. Its genesis is puzzling. The other arrival can be related to the continental margin off Britain, and the later arrival in Fig. I-23 can be associated with the Black Sea depression. A note of interest is that no multipaths were observed for periods longer than 18 sec, implying that the phenomenon is associated with upper crustal heterogeneity.

T. Landers

F. AN EQUIVALENT SCATTERING SURFACE

It is of considerable importance to explain the structure within the earth which is causing the P-wave amplitude and slowness anomalies presented in the last SATS.[1] One of the simplest explanations is to attribute the cause of the anomalies to a single complex, or corrugated, interface, which is postulated to exist in the vicinity close to LASA. Such an approach has been taken in a simple form by Greenfield and Sheppard,[11] as well as by several other workers. Another approach entails the description of the crust and upper mantle structure under LASA as a random medium which can be characterized by a correlation distance, as discussed in detail in Sec. II-B. Nevertheless, there is a certain simplicity involved in the description by means of a single corrugated interface, even though the random medium approach appears preferable, if we try to account both for amplitude and phase anomalies. In addition, there are several very interesting properties that can be ascribed to such an equivalent scattering surface. It is for these reasons that a discussion of an equivalent scattering surface is now given. This discussion also helps to link the present work with that which has been done previously by other workers, such as Greenfield and Sheppard.[11]

It was observed that the average curves for azimuth deviation (AZDEV), and the slowness correction (SLOCOR) data in Figs. III-3(a) and (b), respectively,[1] resemble the results that would be obtained for a single, or possibly multiple-parallel, plane-dipping interface. Thus, an attempt was made to find a plane-dipping interface which would produce values for AZDEV and SLOCOR that would fit best the average values found in this figure. This fit was performed by using a least-squares procedure as follows. The dip angles (DIP) and the azimuths of the up-dip direction (AZUPDIP) for a set of plane-dipping interfaces were specified, as well as the velocity ratio, which was allowed to vary between 0.70 and 0.95; i.e., V_C/V_M varied between these limits, where V_C and V_M are the compressional velocities in the crust and mantle, respectively. For each DIP and AZUPDIP, and for each event, for which the true azimuth and angle of incidence in the mantle are known, the computational procedure of Niazi[12] was used to find AZDEV and SLOCOR. These values were then subtracted from the corresponding average values, shown in the aforementioned figure, for each event. A sum of squares of such differences was found by summing the squares of these differences for each of the 31 events, with the SLOCOR values scaled up by a constant multiplier, so that they are comparable to the AZDEV values. The best fitting plane interface is defined as the one with the DIP and AZUPDIP for which the minimum sum of squares is obtained. The results of this computation are shown in Fig. I-24(a) for a velocity ratio of 0.75. In this figure, the contours of constant sum of squares are shown vs DIP and AZUPDIP. The level of each contour is given in dB relative to the minimum value of the sum of squares. Thus, the point labeled zero dB in Fig. I-24(a) corresponds to the best fitting plane interface, for which we find DIP = 11 degrees and AZUPDIP = 150 degrees. The manner in which AZDEV and SLOCOR vary as a function of azimuth for the 31 events, for

9

the best fitting plane interface, is shown in Figs. I-24(b) and (c), respectively. It is interesting to compare these results with those in Figs. III-3(a) and (b), respectively, in Ref. 1.

Another interesting observation is that the DIP and AZUPDIP for the best fitting plane interface agree very well with the corresponding parameters for the corrugated surface proposed by Greenfield and Sheppard[11] for a velocity ratio of 0.75. In fact, the direction of strike for both sets of results is the same. This agreement is quite remarkable, and encouraging, in view of the different measurement techniques which were employed in each case.

A best fitting plane interface was found for other velocity ratios and the results are given in Table I-5. The AZUPDIP remains approximately the same for all velocity ratios considered, while the DIP increases rapidly as the velocity ratio approaches unity. This latter result is to be expected. There is, of course, no way that the velocity ratio can be known with any certainty. However, some seismic refraction work done by Borchert and Roller[13] at LASA indicates that a velocity contrast of 0.75 is a reasonable assumption.

TABLE I-5

PARAMETERS OF BEST FITTING, PLANE-DIPPING
INTERFACE FOR VARIOUS VELOCITY RATIOS

Velocity Ratio	Dip Angle (deg)	Azimuth of Up-Dip Direction (deg)
0.70	9	150
0.75	11	150
0.80	13	160
0.85	19	160
0.90	27	160
0.95	44	160

The results presented previously for AZDEV and SLOCOR were used to compute the dip angles and azimuths of the up-dip direction, for a set of plane-dipping interfaces, each of which is assumed to be responsible for the measured anomalies at each subarray and for each event. The computational procedure employed is new and represents an inverse to Niazi's method.[12] The computations were performed for various velocity ratios between 0.70 and 0.95; i.e., V_C/V_M varied between these limits. It should be noted that it was not always possible to find a solution for DIP and AZUPDIP for each pair of anomalies (AZDEV and SLOCOR) which were measured. However, it was possible to find such a solution in the great majority of cases.

The DIP and AZUPDIP obtained for a velocity ratio of 0.75 are shown plotted vs the true azimuth in Figs. I-25(a) and (b), respectively. In addition, a mean, or average, curve is drawn in these figures, where the average is taken over the nine values obtained within the subarrays for each event. The average curves for DIP and AZUPDIP in Figs. I-25(a) and (b) vary quite randomly about an overall average of 25.1 and 157.4 degrees, respectively. Some values of DIP can be as high as 75 degrees. In addition, there does not seem to be any correlation between the values of DIP and AZUPDIP.

It has been shown that the values for DIP and AZUPDIP, corresponding to the AZDEV and SLOCOR data, tend to scatter considerably about their mean values. This makes it difficult to discuss these quantities in a deterministic sense. It appears more useful to treat DIP and AZUPDIP as random variables which assume values in an appropriate sample space. The sample

spaces for DIP and AZUPDIP consist, of course, of the real line between 0 and 90, and the real line between 0 and 360 degrees, respectively. We now show how to compute the theoretical probability distribution functions (PDF) for DIP and AZUPDIP, and how these compare with the empirical distribution functions (EDF) for these quantities.

In order to derive the PDFs for DIP and AZUPDIP, we will use some well-known results developed by Longuet-Higgins[14] in the study of random sea waves, or random surfaces, as well as results due to Middleton.[15] It was assumed that the particular structure under LASA that is causing the P-wave anomalies is a complicated corrugated surface which can be described as the sum of a planar surface plus a random surface. This planar surface corresponds to the best fitting plane interface described previously. The random surface is assumed to be a sample function from an isotropic, Gaussian, random process with zero mean, cf., Longuet-Higgins.[14] Using these assumptions, as well as some results of Longuet-Higgins[14] and Middleton (pp. 411-418)[15] it was shown that the probability density functions for the local slope α and AZUPDIP Θ of the random surface are given by

$$p_S(\alpha) = (2\alpha/M)\exp[-(\alpha^2 + \alpha_o^2)/M]\,I_o(2\alpha\alpha_o/M) \quad , \quad \alpha \geqslant 0$$

$$= 0 \quad , \quad \alpha < 0 \quad ,$$

$$p_A(\Theta) = (1/2\pi)\exp(-a_o^2)\left(\{1 + \sqrt{\pi}\,a_o\cos(\Theta - \Theta_o)\exp[a_o^2\cos^2(\Theta - \Theta_o)]\}\right.$$

$$\left. \times \{1 + \mathrm{erf}[a_o\cos(\Theta - \Theta_o)]\}\right) \quad , \quad 0 \leqslant \Theta \leqslant 2\pi$$

where $I_o(x)$ is the zero-order modified Bessel function of the first kind, $\mathrm{erf}(x)$ is the error function, α_o and Θ_o are the slope and AZUPDIP, respectively, for the best fitting plane interface, $M = \overline{\alpha^2} - \alpha_o^2$, and $a_o = \alpha_o/M$ where $\overline{\alpha^2}$ denotes the expectation, or average, of the random variable α^2. The PDFs for α and Θ can be obtained from the probability density functions given above in the usual manner. It should also be noted that if $\alpha_o = 0$, the PDFs for α and Θ reduce to the Rayleigh and uniform distributions, respectively, cf., Davenport and Root.[16] The local dip δ is related to the local slope α in the standard way, i.e., $\delta = \tan^{-1}(\alpha)$. Thus, the PDF for δ can also be found from the PDF for α, but it is convenient to work only with the PDF for α.

The EDFs for α and Θ were computed from the AZDEV and SLOCOR data using the procedure mentioned previously, and the results are shown in Figs. I-26(a) and (b), respectively, for a velocity ratio of 0.75. The EDF for α can be used to estimate $\overline{\alpha^2}$, i.e., its mean-square value, from which the value for M and a_o can be obtained using the above equations, since α_o is known, i.e., $\alpha_o = \tan(11°) = 0.19$, cf., Table I-5. The PDFs for α and Θ can then be computed using the equations given previously, and the results are given in Figs. I-26(a) and (b). It is seen from this figure that there is reasonably good agreement between the EDFs and PDFs. This means that the DIP and AZUPDIP results obtained from the AZDEV and SLOCOR data at LASA correspond closely to the results which would be obtained if one were to measure the local DIP and AZUPDIP of a Gaussian random surface which is superimposed on a planar surface.

An attempt was made to describe graphically the random surface discussed previously, and the computations employed are described briefly. A velocity ratio of 0.75 was chosen and a 60- × 60-km region placed symmetrically about the A0 subarray at LASA was considered. A master plane was taken passing arbitrarily at 50 km beneath subarray A0 with a DIP and AZUPDIP of 11 and 150 degrees, respectively. This plane corresponds to the best fitting plane-dipping

interface discussed previously. The direction cosines of the seismic rays in the crust were computed from the AZDEV and SLOCOR data using the procedure mentioned previously. These rays were then traced back to their point of intersection with the master plane. In the vicinity of these points, the master plane was modified to have a local DIP and AZUPDIP, which are computed from the AZDEV and SLOCOR data. The resulting surface was then smoothed once with a standard, five-point smoothing scheme. This smoothed surface is shown in Fig. I-27, which gives the contours of constant depth (in km) as a function of the x- and y-coordinates. A three-dimensional view of the surface is depicted in Figs. I-28(a-d). The viewing angle is 30 degrees, relative to the vertical z-axis, and the rotation angles are 30, 120, 210 and 300 degrees, as indicated in Figs. I-28(a-d), respectively.

<div align="right">J. Capon</div>

REFERENCES

1. Seismic Discrimination SATS, Lincoln Laboratory, M.I.T. (30 June 1972), DDC AD-748304.

2. L. R. Johnson, "Array Measurements of P Velocities in the Upper Mantle," J. Geophys. Res. 72, 6309 (1967).

3. J. Capon, "Analysis of Rayleigh Wave Multipath Propagation at LASA," Bull. Seismol. Soc. Am. 60, 1701-1731 (1970), DDC AD-716084.

4. D. L. Springer and R. L. Kinnaman, "Seismic Source Summary for U.S. Underground Nuclear Explosions, 1961-1970," Bull. Seismol. Soc. Am. 61, 1073-1098 (1971).

5. J. Brune, "Surface Waves and Crustal Structure," in The Earth's Crust and Upper Mantle, Geophysical Monograph 13, 230-242 (Am. Geophysical Union, 1969).

6. I. Noponen, M. Porkka, S. Pirhonen and U. Luosto, "The Crust and Mantle in Finland," J. Phys. Earth 15, 19-24 (1967).

7. D. Hill and L. Pakiser, "Crustal Structure between the Nevada Test Site and Boise, Idaho, from Seismic-Refraction Measurements," in The Earth Beneath the Continent, Geophysical Monograph 10, 391-419 (Am. Geophysical Union, 1966).

8. A. Wickens and K. Pec, "A Crust-Mantle Profile from Mould Bay, Canada, to Tucson, Arizona," Bull. Seismol. Soc. Am. 58, 1821-1831 (1968).

9. D. Boore, "Finite Difference Solutions to the Equation of Elastic Wave-Propagation, with Application to Love Waves over Dipping Interfaces," Ph. D. Thesis, M.I.T., 184-193 (1970).

10. R. Kanestrom, "The Dip of the Moho Beneath NORSAR," University of Bergen, Norway (1969).

11. R. J. Greenfield and R. M. Sheppard, "The MOHO Depth Variations under the LASA and Their Effect on $dT/d\Delta$ Measurements," Bull. Seismol. Soc. Am. 59, 409-420 (1969).

12. M. Niazi, "Corrections to Apparent Azimuths and Travel-Time Gradients for a Dipping Mohorovicic Discontinuity," Bull. Seismol. Soc. Am. 56, 491-509 (1966).

13. C. A. Borcherdt and J. C. Roller, "Preliminary Interpretation of a Seismic-Refraction Profile Across the Large Aperture Seismic Array, Montana," NCER-2, U. S. Geological Survey, Menlo Park, California (1967).

14. M. S. Longuet-Higgins, "Statistical Properties of an Isotropic Random Surface," Phil. Trans. Roy. Soc. London A 250, 157-174 (1957).

15. D. Middleton, An Introduction to Statistical Communication Theory (McGraw-Hill Book Co., New York, 1960).

16. W. B. Davenport, Jr. and W. L. Root, An Introduction to the Theory of Random Signals and Noise (McGraw-Hill Book Co., New York, 1958).
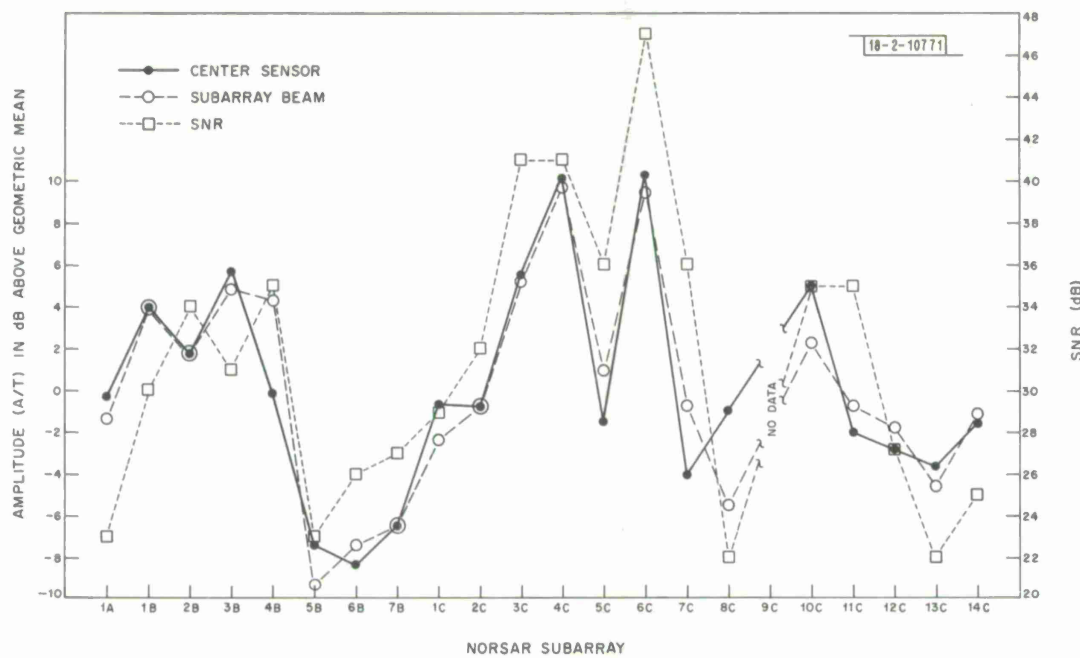
Fig. I-1.   P-wave amplitudes at NORSAR subarrays for a presumed explosion in Eastern Kazakh, 25 May 1971.   SNR at 2 Hz is also shown.
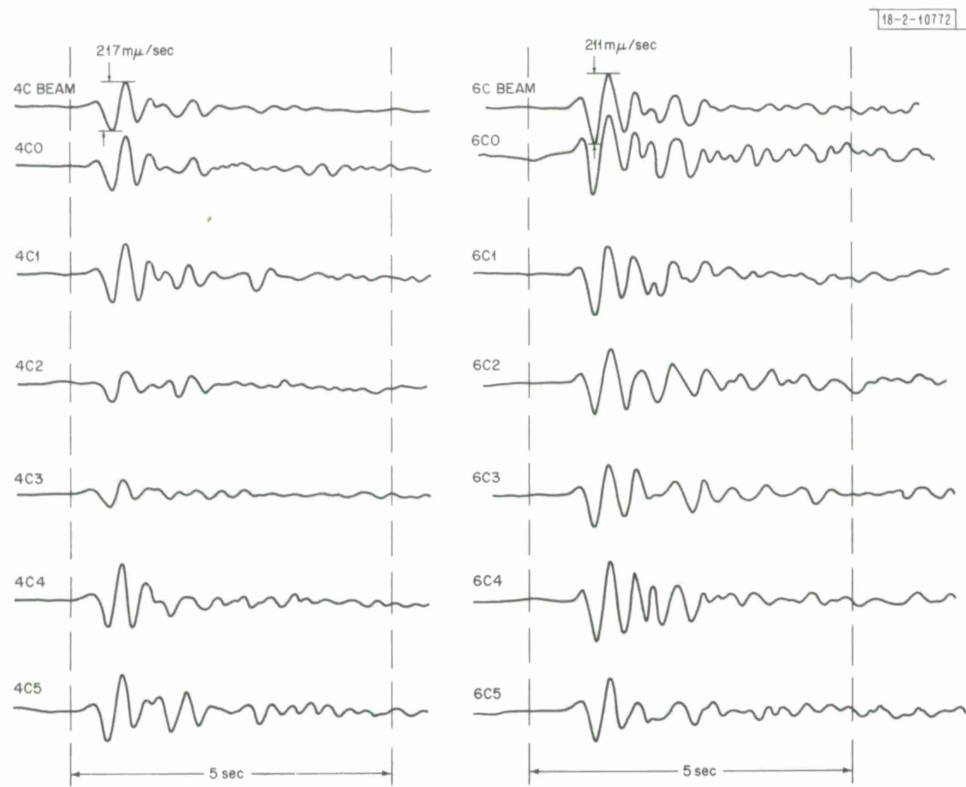

Fig. I-2.   P-waves at sensors of two high amplitude NORSAR subarrays for presumed explosion of 25 May 1971 in Eastern Kazakh.   Subarray beams are also displayed.

18-2-10773
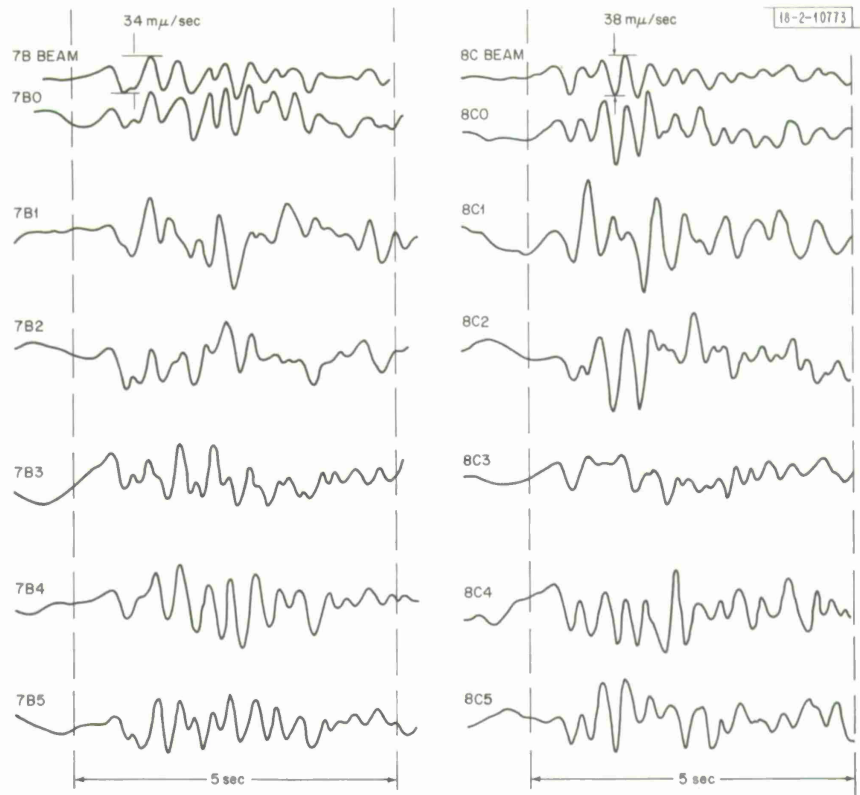
Fig. I-3. P-waves at sensors of two low-amplitude NORSAR subarrays for same event as in Fig. I-2.


18-2-10774
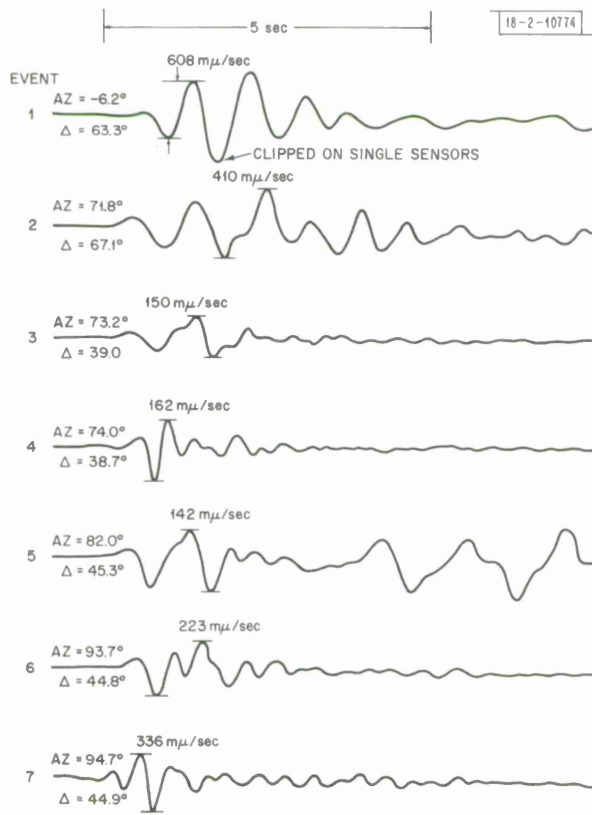
Fig. I-4. NORSAR steered beams of seven events using center sensors. Events 3 and 4 are presumed explosions in Eastern Kazakh.

14
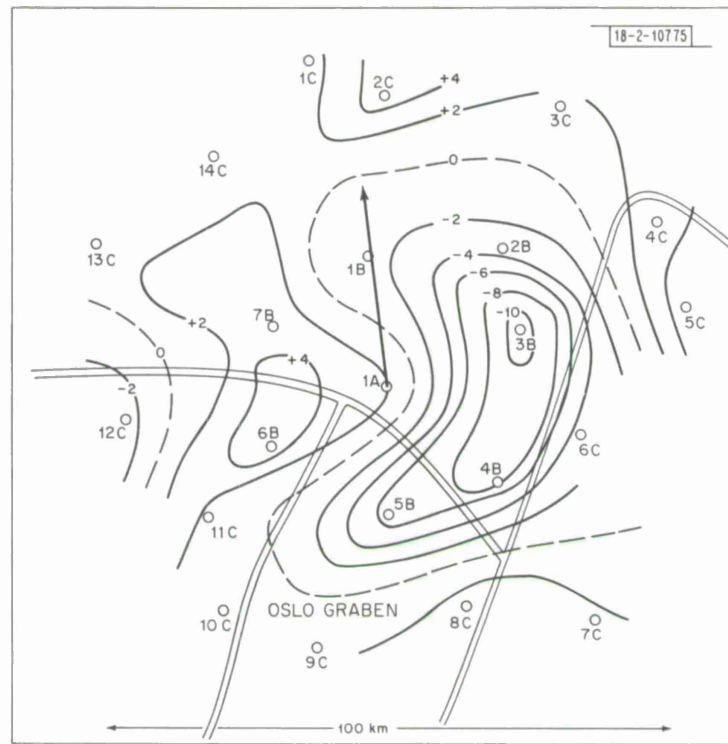
Fig. I-5.   NORSAR amplitude for event 1. Azimuth = $-6.2°$, $\Delta = 63.3°$.
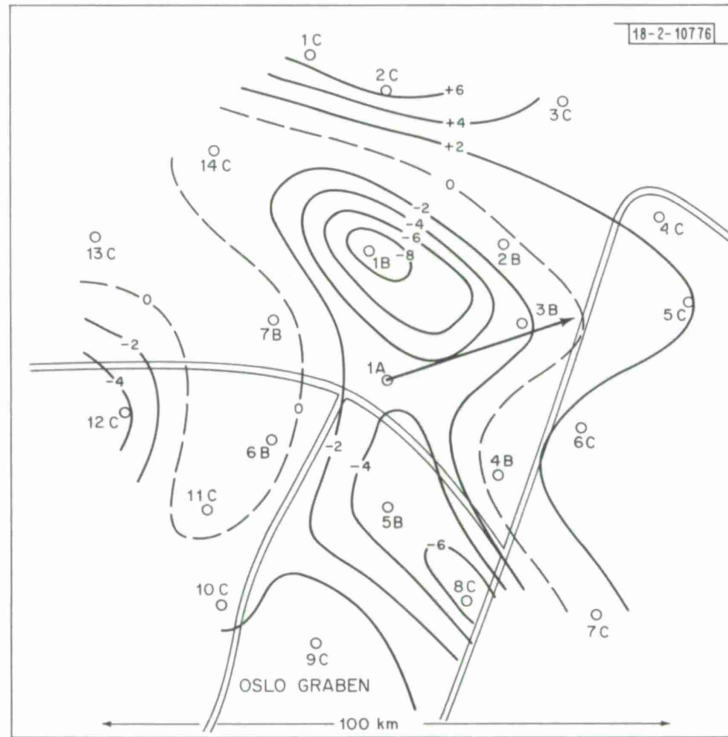
Fig. I-6.   NORSAR amplitude for event 2.   Azimuth = $71.8°$, $\Delta = 67.1°$.
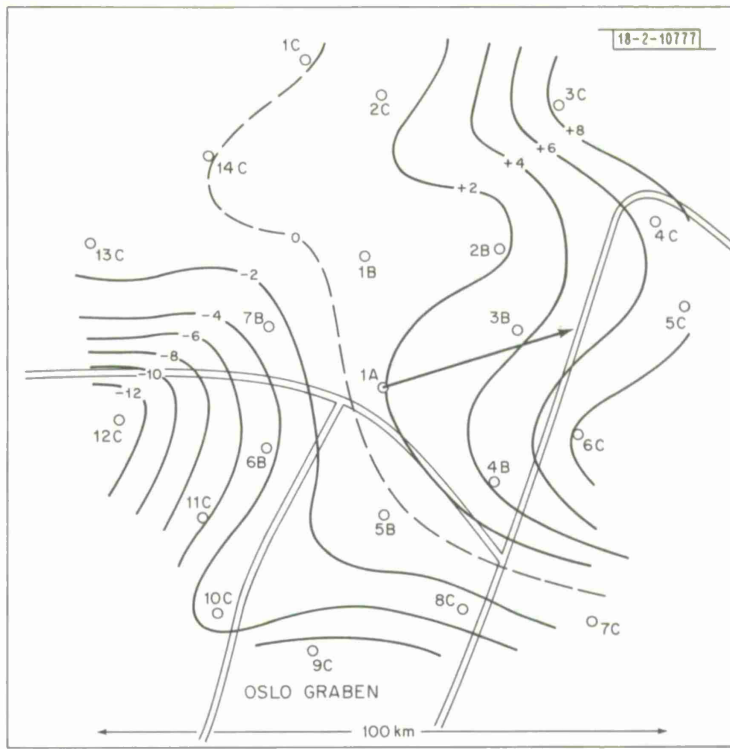
Fig. I-7.   NORSAR amplitude for event 3.   Azimuth = 73.2°,   Δ = 39.0°.
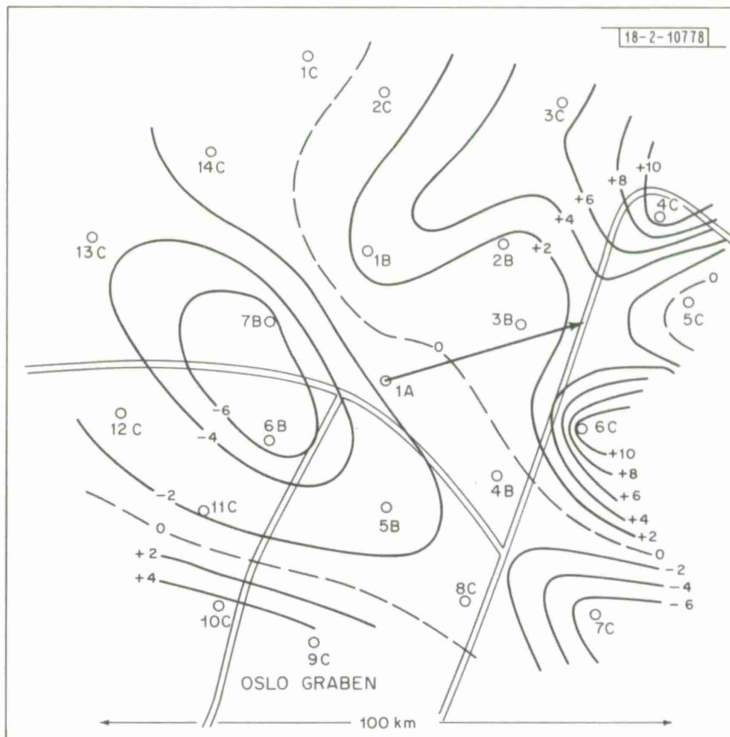
Fig. I-8.   NORSAR amplitude for event 4.   Azimuth = 74.0°,   Δ = 38.7°.

16
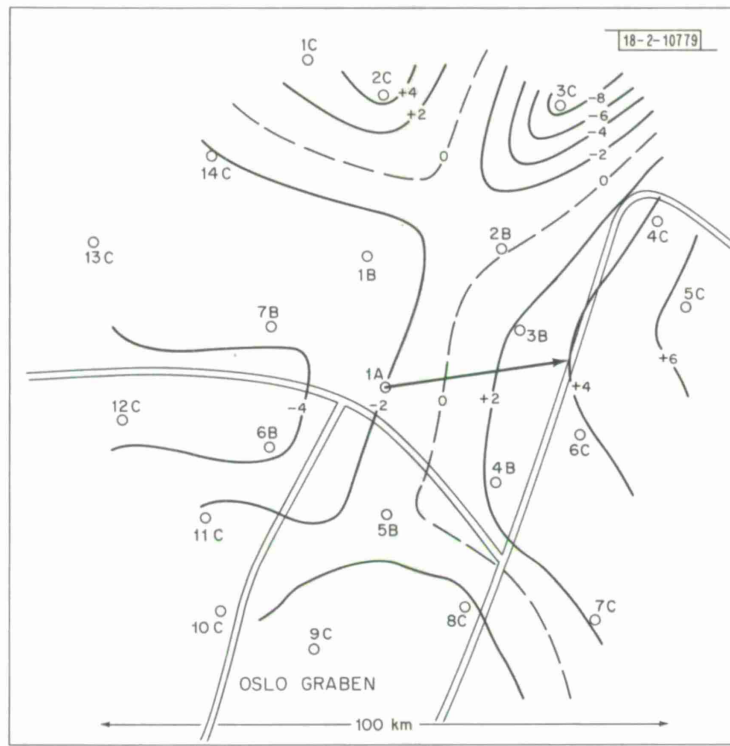
Fig. I-9.   NORSAR amplitude for event 5.   Azimuth = 82.0°,   Δ = 45.3°.
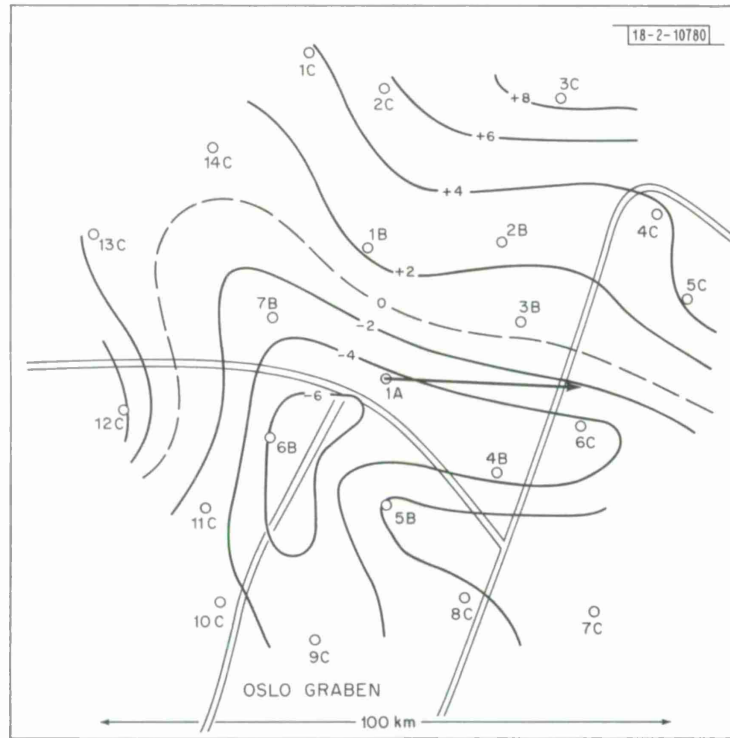
Fig. I-10.   NORSAR amplitude for event 6.   Azimuth = 93.7°,   Δ = 44.8°.

17
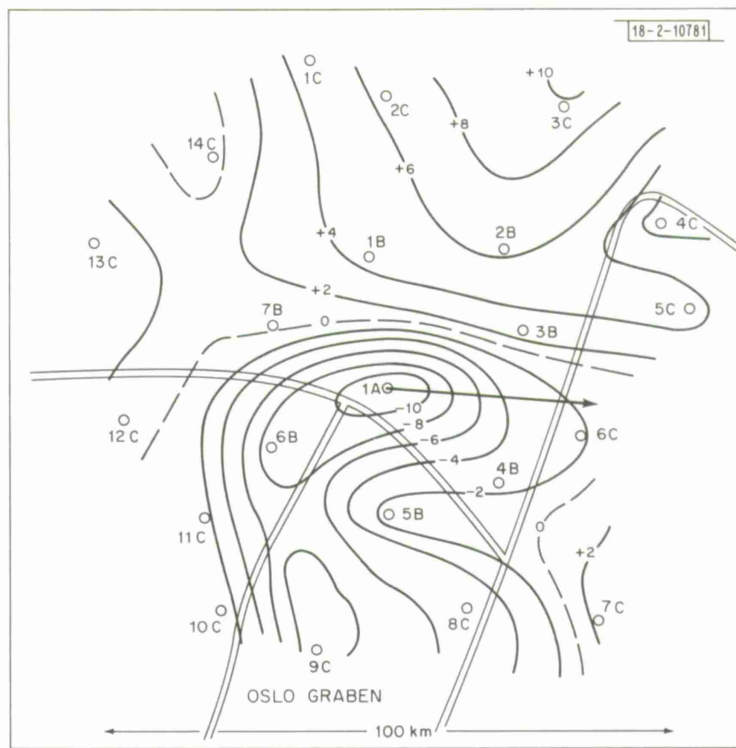
Fig. I-11. NORSAR amplitude for event 7. Azimuth = 94.7°, Δ = 44.9°.
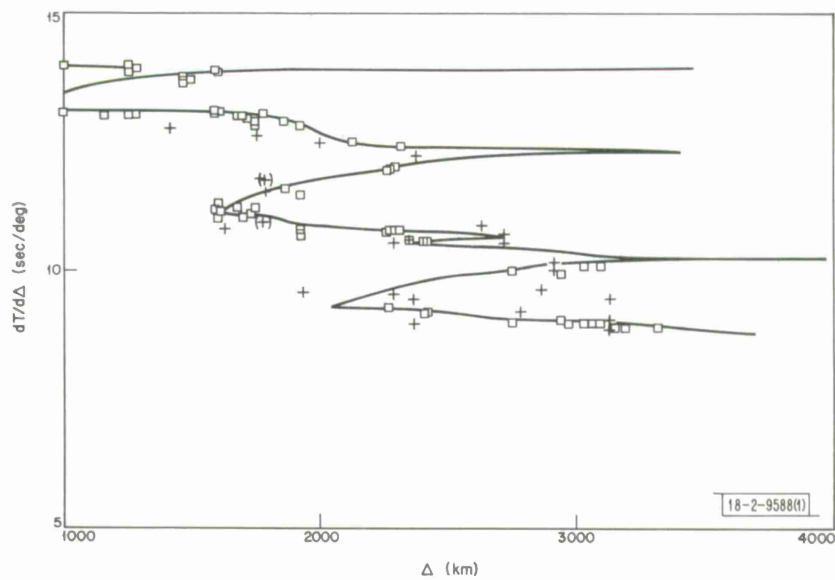
Fig. I-12. dT/dΔ values measured at NORSAR (crosses) together with data of Johnson[2] and calculated curve for model WNA fitted to Johnson's data and nuclear explosion travel times within western North America.
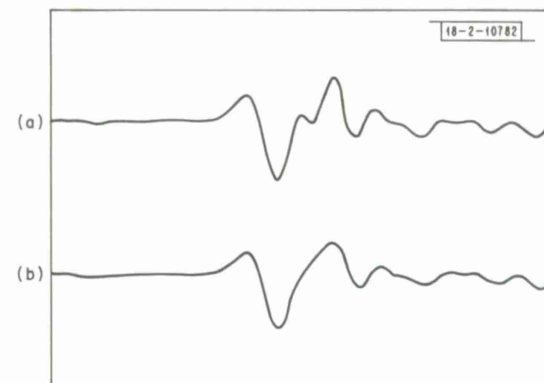
Fig. I-13. Beams formed using a single NORSAR subarray (2B) of the P wave from a deep Hindu Kush earthquake: (a) with hand-picked time delays; (b) with delays calculated for a plane wave.
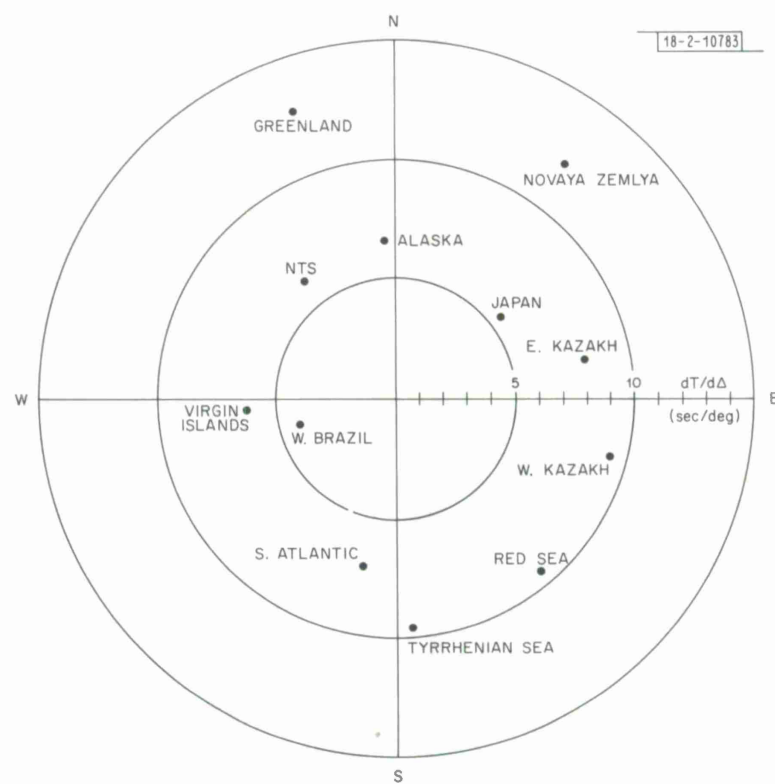

Fig. I-14. Distribution in slowness space of events used to measure sensor delays.
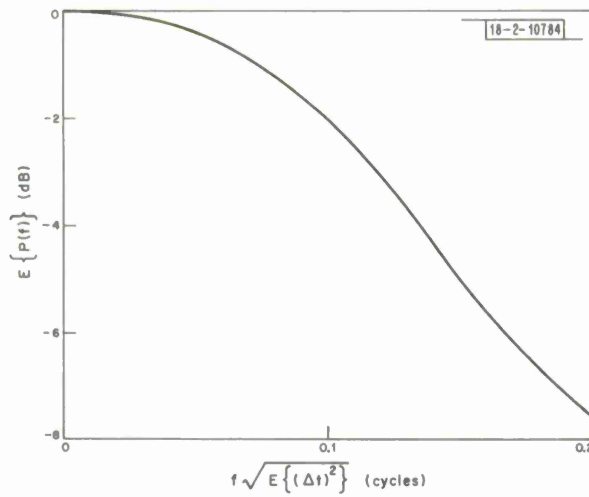
Fig. I-15. Expected spectral degradation as a function of rms time error for perfectly coherent signals. (E means expectation; f is frequency; ΔT is the timing error; P(f) is the "transfer function" for beamforming.)

(a)

(b)
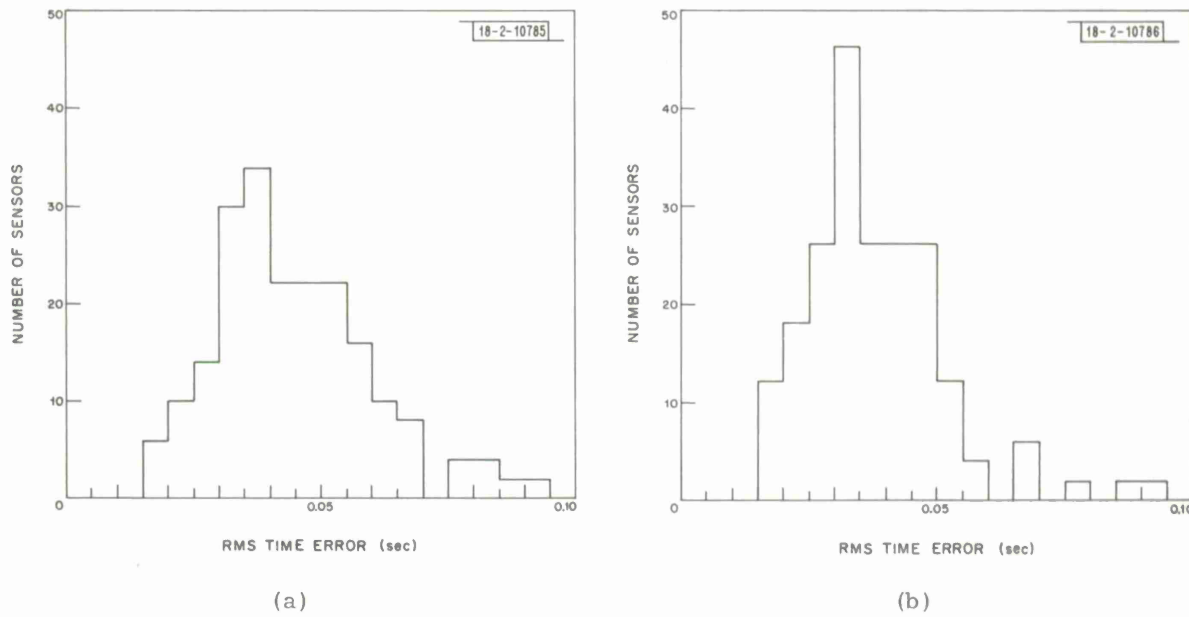
Fig. I-16. Distribution of rms time errors. (a) Observed distribution for individual NORSAR sensors. (b) Distribution to be expected if a constant time correction is used.
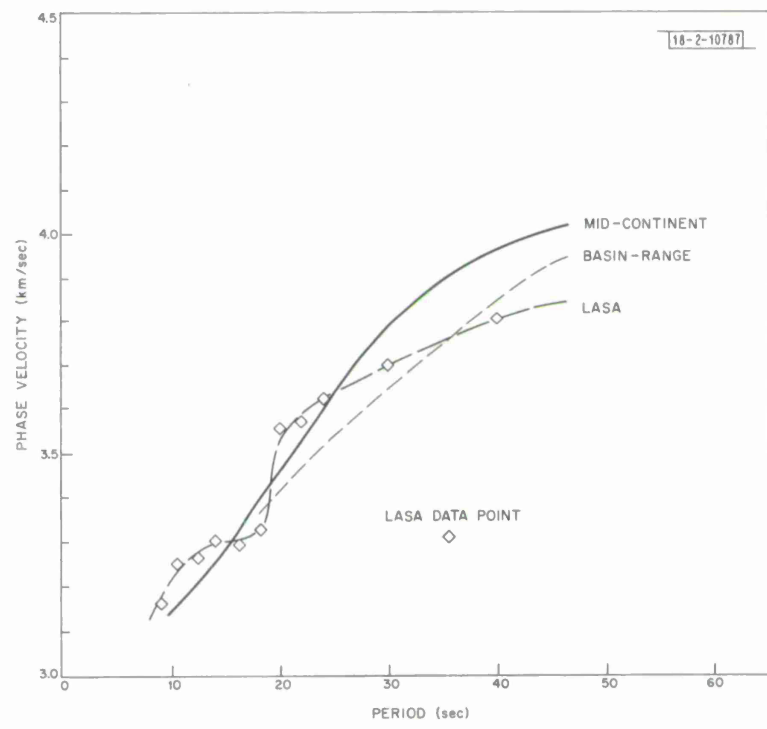
Fig. I-17.   Phase velocity curve for LASA.

21
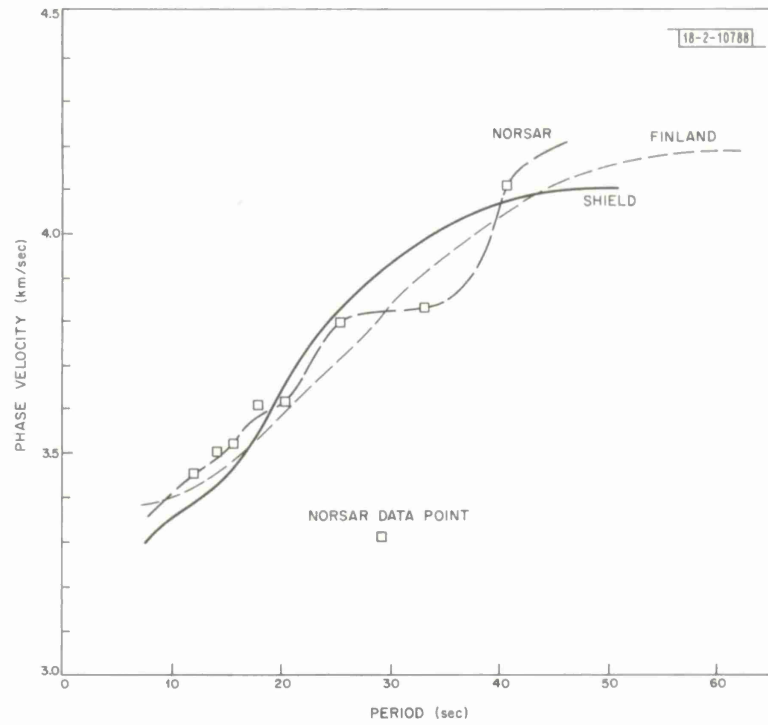
Fig. I-18.   Phase velocity curve for NORSAR.
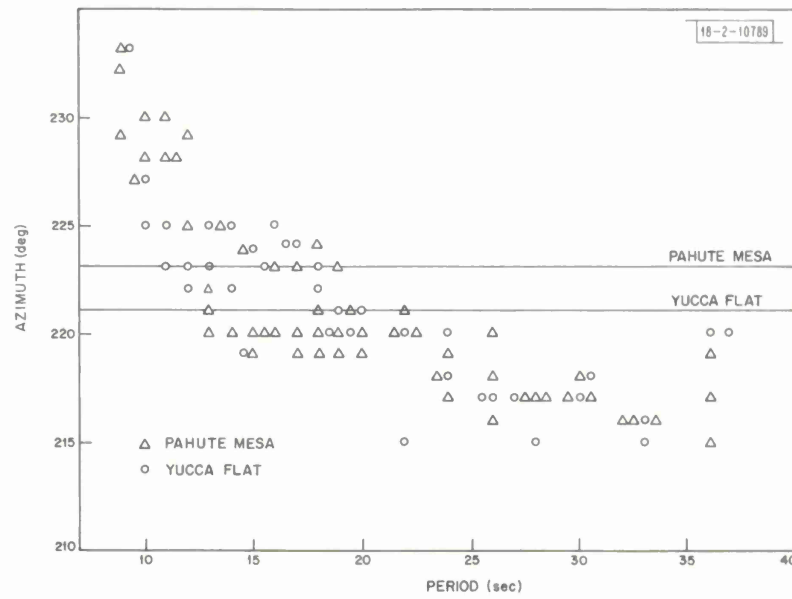
Fig. I-19.   Azimuth of arrival of Rayleigh waves at LASA from NTS as a function of period.

22
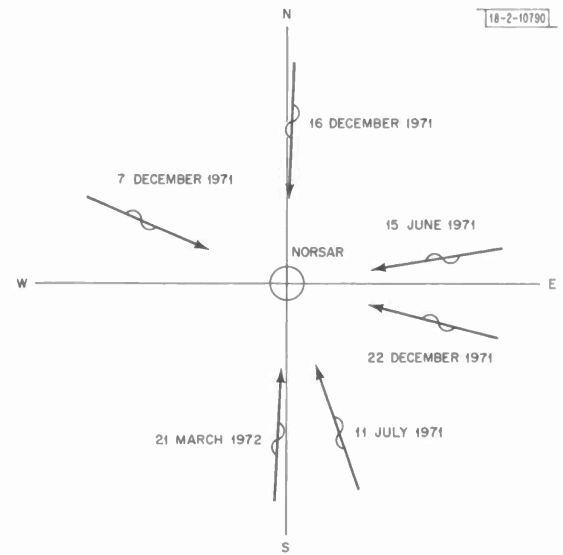
Fig. I-20. Azimuth of arrival of 20-sec component of Rayleigh wave for each NORSAR event.
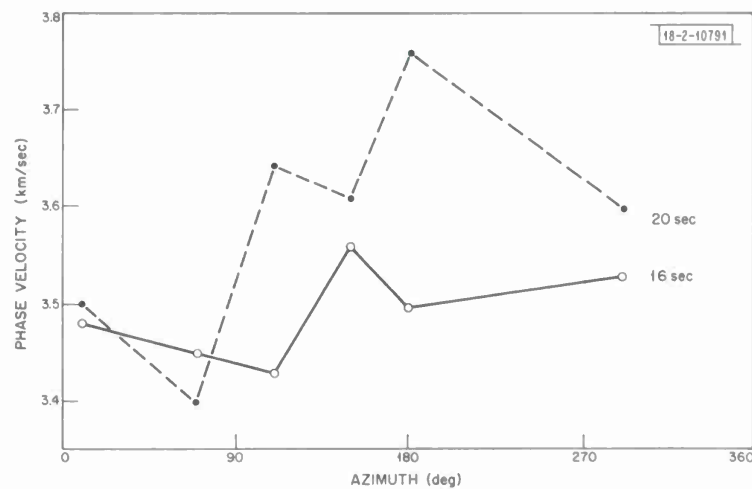
Fig. I-21. Phase velocity for 16- and 20-sec Rayleigh waves at NORSAR as a function of azimuth.

23
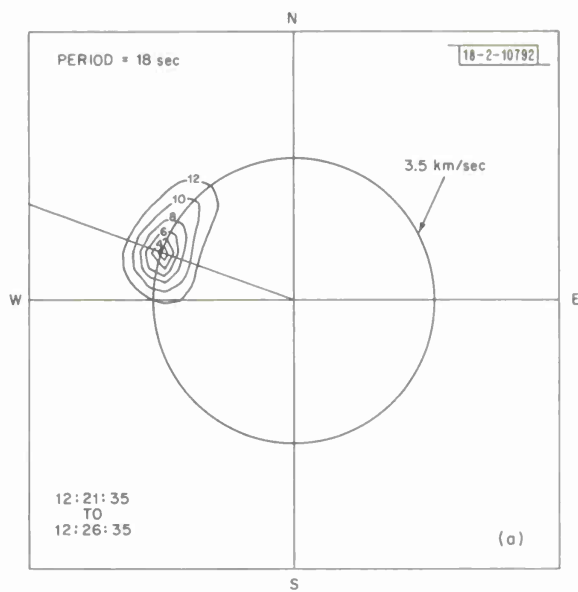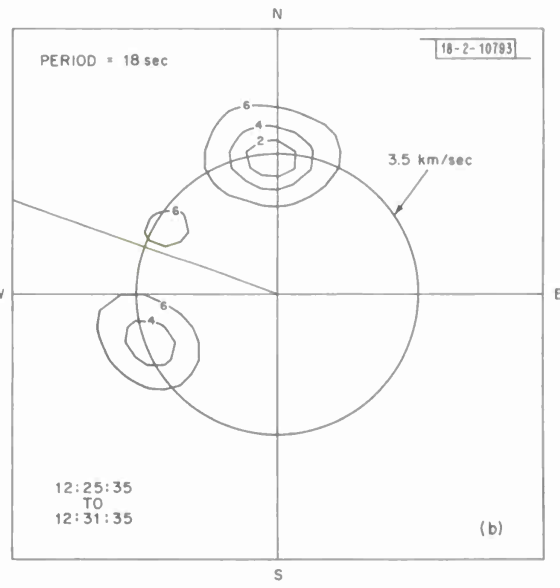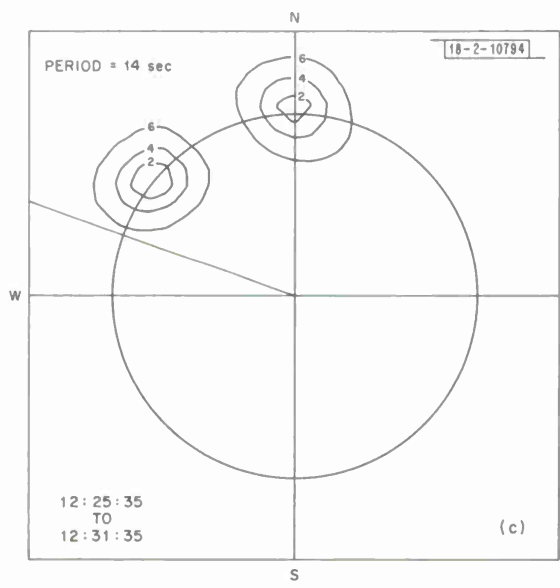
Fig. I-22. Wavenumber spectra for 14- and 18-sec Rayleigh waves at NORSAR from event of 7 December 1971. Plot (a) shows main arrival; plots (b) and (c), for data 4 minutes later, show multipath arrivals.

24
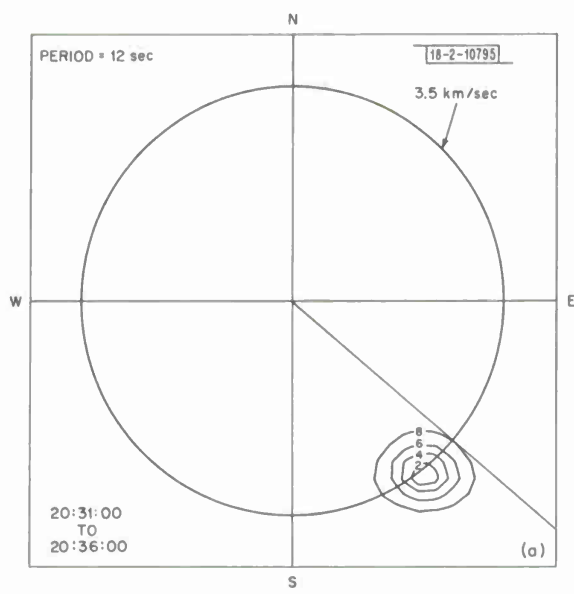
(a)
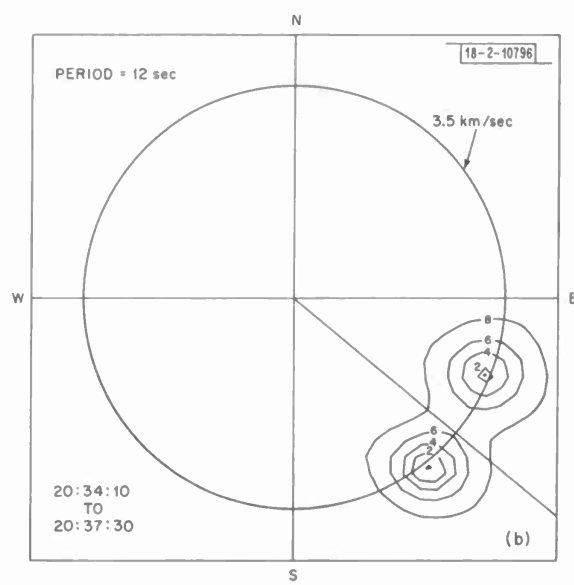
(b)

Fig. I-23. Wavenumber spectra for event of 11 July 1971 at NORSAR.
Plot (a) shows main arrival; plot (b), for data 3 min. 10 sec later,
shows a multipath.
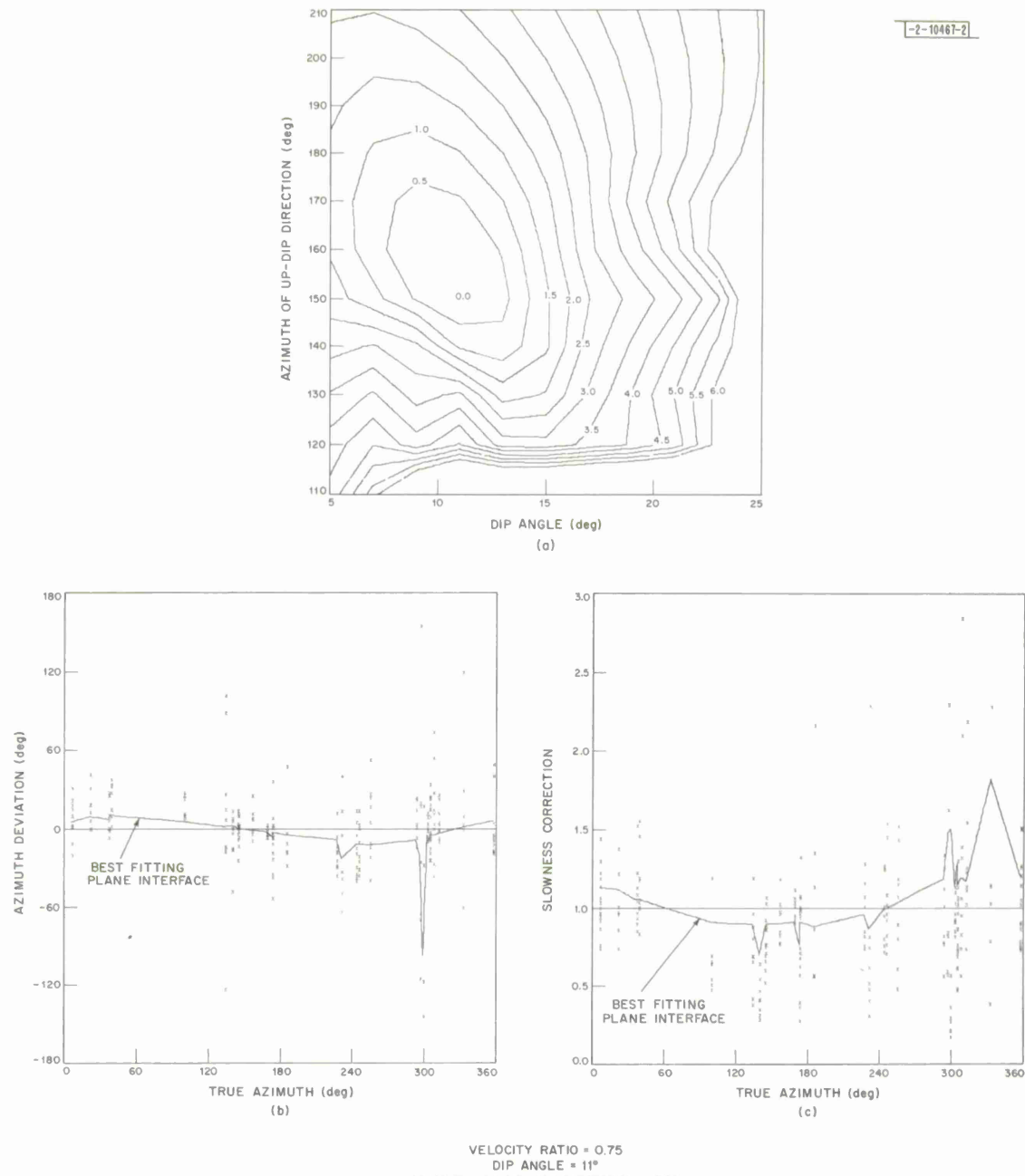
Fig. I-24. Determination of parameters of best fitting plane dipping interface.
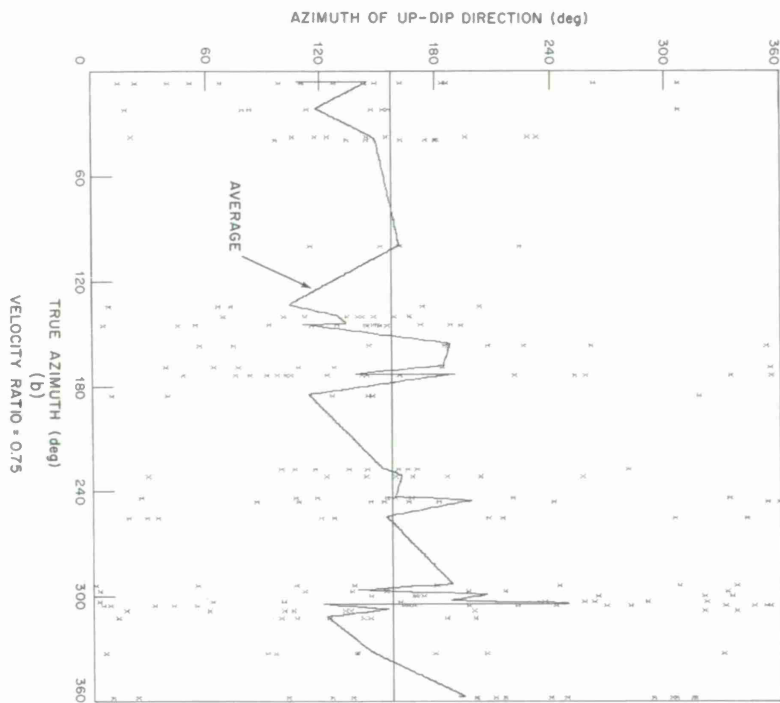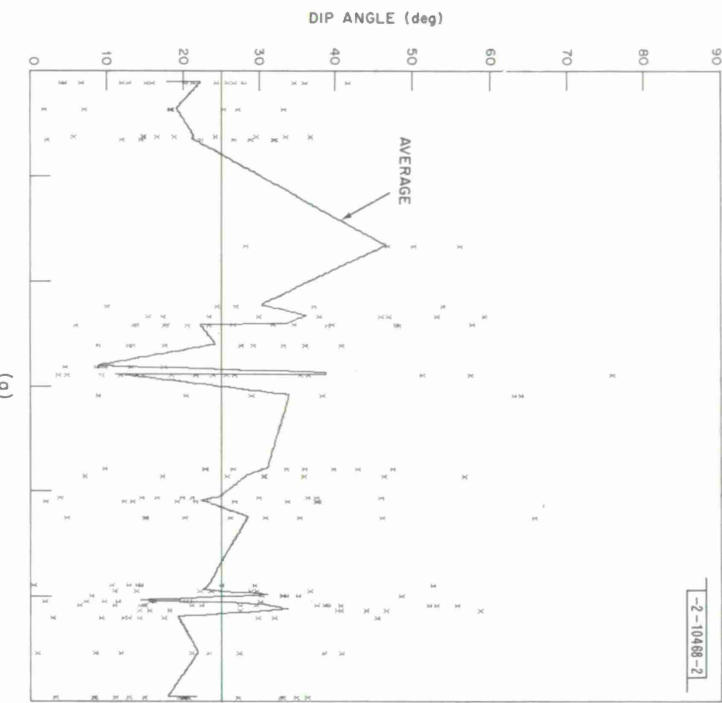
Fig. I-25.   Dip angle and azimuth of up-dip direction vs true azimuth.

27
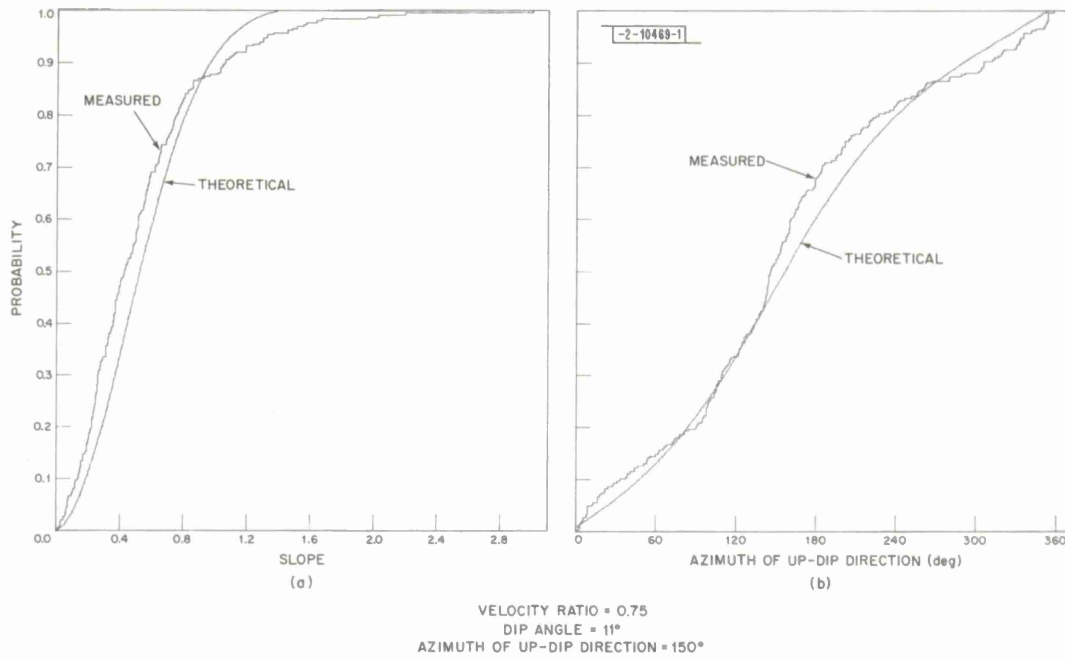
Fig. I-26. Comparison of empirical distribution functions of slope and azimuth of up-dip direction with theoretical cumulative distribution functions.
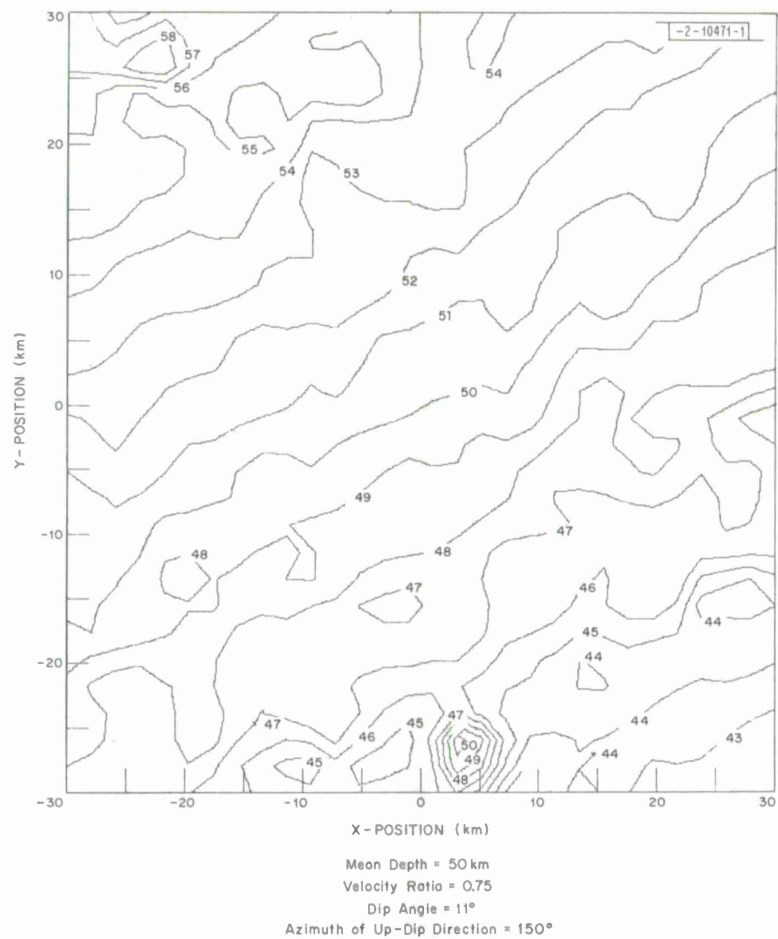
Fig. I-27.   Contour plot of depth vs x- and y-coordinates for equivalent scattering surface.
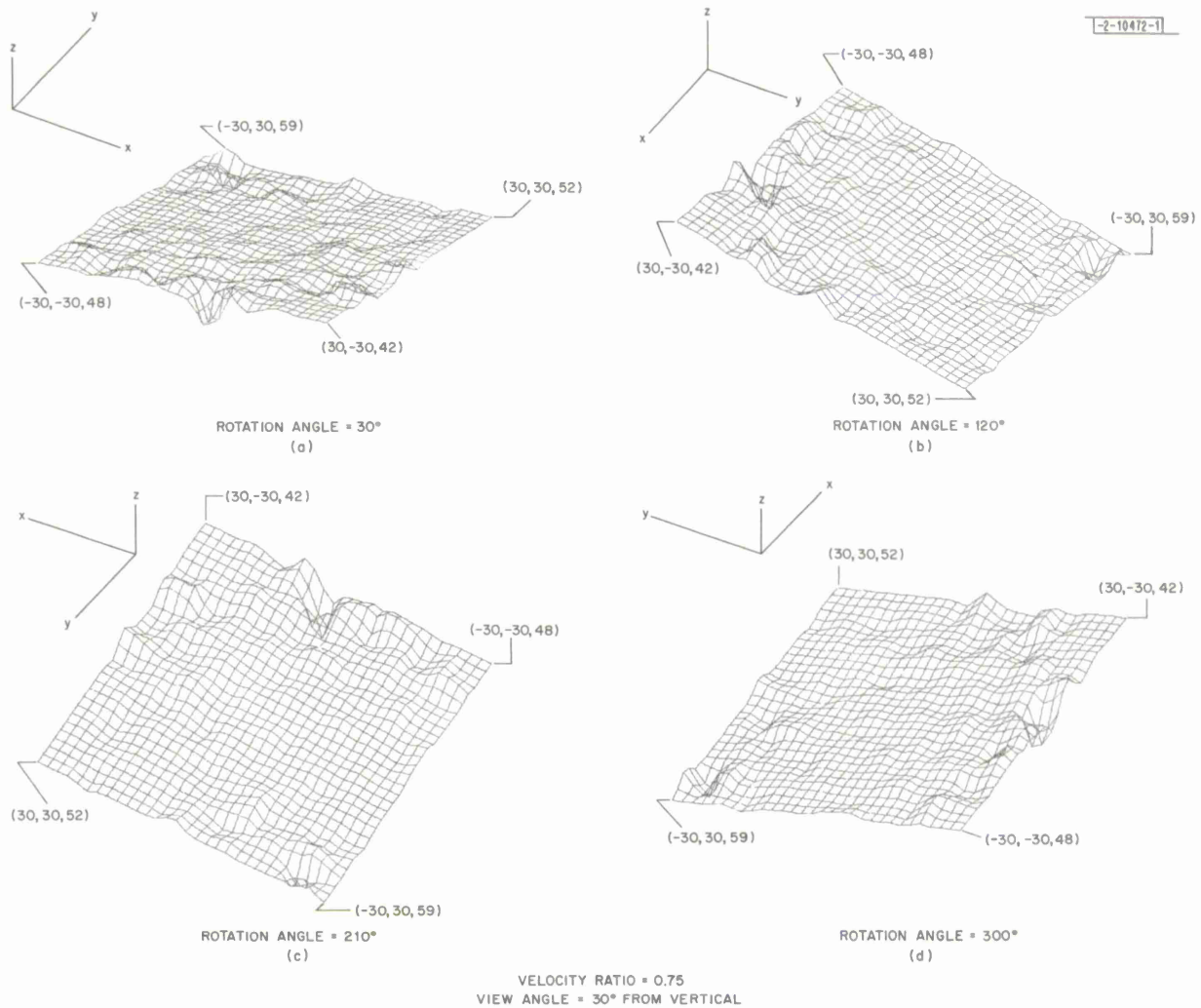
Fig. I-28.   Three-dimensional views of equivalent scattering surface.

II. EARTH STRUCTURE

A. REPRESENTATION OF APPROACH ANGLE ANOMALIES

Approach angle anomalies have been measured for P-wave signals at LASA observed during the first 5 sec after the onset time. These anomalies were obtained within the nine subarrays comprising the A-, B-, and C-rings at LASA, and the results were presented in the previous SATS.[1] Azimuth deviation (AZDEV) and slowness (or dT/dΔ) correction (SLOCOR) data were plotted vs the true azimuth of the epicenter of the event. It was pointed out that this type of presentation of the results held certain advantages in the interpretation of the data.

We can, however, represent the anomalies in a circular diagram in a way used by Manchee and Weichert[2] and Vinnik and Nikolayev.[3] This approach entails the plotting of the anomalies as a series of arrows in (dT/dΔ, Azimuth) space. The tail of the arrow represents the dT/dΔ and azimuth measured for the incoming P-wave signal at the array, and its head represents the dT/dΔ and azimuth that would be obtained from the true, or in this case CGS, location and the J-B tables. This method has been applied recently by Davies and Sheppard[4] to the study of the P-wave slowness anomalies at LASA. They have termed the resultant presentation the "array diagram."

It was shown by Manchee and Weichert,[2] that if the anomaly were caused by a plane-dipping interface located directly under the array, the array diagram would consist of a set of error vectors whose magnitudes are all approximately the same and which all point in the direction of the dip of the interface. Thus, the effects of a sloping interface can be determined from the array diagram by fitting a constant vector to the error vectors in the diagram.

Additional results in the interpretation of the array diagram are due to Davies and Sheppard.[4] They point out that a smoothly varying distribution of arrows, all approximately of equal length and pointing in the same direction, would indicate a bias introduced beneath the array. The reason for this is that all ray paths from the various event epicenters to LASA must traverse the same structure under the array. This result is slightly different from that of Manchee and Weichert,[2] mentioned previously, in that the anomaly caused by a smooth distribution of arrows, although due to structure under the array, need not be caused by a plane-dipping interface. In addition, Davies and Sheppard point out that the spatial rate of variation of the error vectors can be associated with heterogeneities at certain depths in the earth. The more rapid these spatial variations become, the more distant from LASA the heterogeneities must be placed to explain the anomalies. The reason for this can be easily seen on the basis of the separation of the ray paths from the various event epicenters to LASA.

In view of the power of the presentation contained in the array diagram, the P-wave anomalies measured within subarrays at LASA have been displayed in "subarray diagrams" and the results for the B-ring are given in Figs. II-1(a-d). The four diagrams in Fig. II-1 are typical of the nine subarray diagrams obtained. There are certain regularities seen both within each diagram and amongst the several diagrams. For instance in all diagrams there is a tendency for the arrows to line up in a NW-SE direction. This suggests that dipping structures of some sort underlie each subarray, and that these structures are moderately persistent across the whole of the C-ring. This is shown quite clearly for instance by the similarity of all diagrams to a subarray average diagram [Fig. II-2(a)], being the average of nine subarrays. Figure II-2(b) shows the mean vector of Fig. II-2(a) applied uniformly to all sources, and Fig. II-2(c) shows the

theoretical effect of a single dipping interface with a strike of 46° to 226° and a dip of 11° (veloc-ity contrast at interface is 0.75:1). This is used only as an example. Niazi's computational pro-cedure[5] has been used. The result agrees quite favorably with the corresponding results of 11° and 330° found by an alternative method, cf., Sec. I-F.

Davies and Sheppard[4] found that the mean error vector for their array diagram pointed north and had a magnitude of 0.25 sec/deg. It is possible to show that this error vector could be as-cribed to a plane-dipping interface under LASA with dip of about 3° and direction of dip at an azimuth of 0°.

It is encouraging to note that there are certain similarities between the subarray average diagram given in Fig. II-2(a) and the array diagram for the full LASA given in Fig. 1 of Ref. 4. However, the fact that there are differences can be explained by the following reasons:

(1)   The effect of the random part of the local crust and upper mantle structure at LASA is greater in the subarray average diagram than in the LASA diagram (cf., Sec. II-C).

(2)   The subarray average diagram represents an average taken over a circular area of the Moho of about 30 km in diameter, while the array diagram averages over a circle of 200 km diameter. Thus, the effect of a possibly warped Moho (if the Moho is the prime interface) under LASA may be seen in the subarray average diagram, but not in the array diagram.

(3)   The array diagram is based on a least-squares fit of a plane wave to arrival times measured from the first motion of the P-wave. As a result, this diagram pertains to the high-frequency part of the P-wave spectrum. The subarray average diagram was obtained at a frequency of 0.8 Hz. In addition, there may be some effects due to frequency windowing in the results reported here that do not appear in the array diagram.

<div align="right">J. Capon
D. Davies</div>

B.   CHARACTERIZATION OF CRUST AND UPPER MANTLE STRUCTURE UNDER LASA AS A RANDOM MEDIUM

An analysis has been made of the P-wave slowness and amplitude anomalies within the sub-arrays at LASA. The method of measurement was described in the last SATS.[1] These anomalies were measured for the P-waves of 31 events located at various azimuths and distances from LASA. They were obtained within the subarrays contained in the A-, B-, and C-rings at LASA, so that a total of 279 observations were taken. The data were observed on the short-period ver-tical seismometers at LASA. The frequency used in the measurement was 0.8 Hz, so that the wavelength of the P-wave is about 10 km, assuming the average compressional velocity is about 8 km/sec.

A model has been proposed to explain the cause of the P-wave anomaly data, in which the crust and upper mantle structure under LASA is characterized as a random, or Chernov-type, medium.[6] This model seems to be quite successful in explaining the P-wave anomaly data and a description of these results is now presented. In order to do this, it is necessary to present a brief review of some of the results due to Chernov concerning wave propagation in a random medium. Although these results are derived for the case of wave propagation in a liquid, or gaseous, medium, it may be shown that they can be used for an elastic medium with only minor modifications.

The index of refraction for the random medium is the random function $\mu(x, y, z)$ defined as

$$\mu(x, y, z) = [c(x, y, z)/c_o(x, y, z)] - 1 \quad ,$$

where $c(x, y, z)$ is the velocity and $c_o(x, y, z)$ is the average velocity, i.e., $c_o(x, y, z) = \bar{c}(x, y, z)$. In addition, it is assumed that only small variations from homogeneity exist; i.e., the mean-square value of the relative index of refraction is much less than unity

$$\overline{\mu^2}(x, y, z) \ll 1 \quad .$$

If the random process is statistically isotropic, then the correlation coefficient, N, depends only on the distance, r, between the points (x_1, y_1, z_1), (x_2, y_2, z_2). A particularly useful correlation coefficient, which was assumed for the random medium in the analysis, is the Gaussian correlation coefficient, given by

$$N(r) = \exp(-r^2/a^2) \quad ,$$

where a is known as the correlation distance.

The propagation of a wave in a medium with random inhomogeneities leads to fluctuations of the amplitude and phase characteristics of the wave field due to the superposition of the scattered waves and the primary wave. There is a dependence between the fluctuations of the characteristics of the wave field and the fluctuations of the relative index of refraction. Thus, it is feasible to relate the statistical properties of the wave field to the statistical properties of the ensemble of random media. Hence, it is possible, by measuring the amplitude and phase characteristics, to determine several parameters which are important in the description of the random medium. A comprehensive set of such results has been given by Chernov.[6] The particular model assumed by Chernov is shown in Fig. II-3. A uniform plane wave is propagating in the left half-space, $x < 0$, which is homogeneous, i.e., contains no random inhomogeneities. This wave is termed the direct or homogeneous wave, and enters the right half-space, $x \geqslant 0$, which is inhomogeneous and contains random inhomogeneities. The wavenumber, in rad/km, and frequency, in rad/sec, of the wave in the left half-space are denoted by k and ω, respectively. Thus, we have $k = \omega/c_o = 2\pi/\lambda$, where λ is the wavelength in km.

It is assumed that there are two receivers located at the coordinates (L, 0, 0) and (L, 0, ℓ) as shown in Fig. II-3. An essential role in the theory is played by the wave parameter D defined as: $D = 4L/ka^2$. It is assumed that large-scale inhomogeneities exist in the random medium, i.e., $ka \gg 1$, and also that $L \gg a$.

The amplitude fluctuation, B, is defined as: $B = \ln(A/A_o)$, where A_o is the amplitude of the wave in the left half-space and $A = A(x, y, z)$ is the amplitude of the wave field at the point (x, y, z) in the right half-space. The phase fluctuation, S, is defined as the phase of the wave field in the right half-space relative to that of the homogeneous wave. The ratio of the mean-square fluctuations of phase and amplitude, $\overline{B^2}/\overline{S^2}$, was of importance in the analysis. Using the results of Chernov (pp. 82-83), we have

$$\frac{\overline{B^2}}{\overline{S^2}} = \frac{1 - \frac{1}{D} \tan^{-1}(D)}{1 + \frac{1}{D} \tan^{-1}(D)}$$

In addition, the crosscorrelation coefficient between the amplitude and phase fluctuations was derived by Chernov (pp. 85-89), as

$$R_{bs} = \overline{BS}/(\overline{B^2}\,\overline{S^2})^{1/2}$$

$$= 1/2\,\ln(1+D^2)/\{D^2 - [\tan^{-1}(D)]^2\}^{1/2} \quad .$$

The autocorrelation of the amplitude, as well as phase, fluctuations in the direction which is longitudinal to the direction of wave propagation in the left half-space, i.e., in the direction of the x-axis, was also computed by Chernov (pp. 89-95). These correlations were computed between two receivers, or sensors, located at the coordinates $(L_1, 0, 0)$ and $(L_2, 0, 0)$. It was shown that both the amplitude and phase fluctuations are practically completely correlated over a longitudinal distance, ΔL, given by: $\Delta L = ka^2/2$. Since it has been assumed that $ka \gg 1$, it follows that $\Delta L \gg a$.

The transverse autocorrelation coefficient for the amplitude and phase fluctuations, computed between the two receivers shown in Fig. II-3, which are located at the coordinates $(L, 0, 0)$ and $(L, 0, \ell)$ was derived by Chernov (pp. 95-110). These two receivers are located in a plane which is transverse to the direction of propagation of the wave in the left half-space, i.e., the direction of the x-axis. The results for the case when the wave parameter is large, $D \gg 1$, i.e., Fraunhofer diffraction, are given by

$$R_b(\ell) = \overline{B_1 B_2}/\overline{B^2} = \frac{\exp\left(-\dfrac{\ell^2}{a^2}\right) - \dfrac{1}{D}\left[\dfrac{\pi}{2} - \text{Si}\left(\dfrac{\ell^2}{Da^2}\right)\right]}{1 - \dfrac{1}{D}\tan^{-1}(D)} \quad ,$$

$$R_s(\ell) = \overline{S_1 S_2}/\overline{S^2} = \frac{\exp\left(-\dfrac{\ell^2}{a^2}\right) + \dfrac{1}{D}\left[\dfrac{\pi}{2} - \text{Si}\left(\dfrac{\ell^2}{Da^2}\right)\right]}{1 + \dfrac{1}{D}\tan^{-1}(D)} \quad ,$$

where B_1, B_2, S_1, S_2 are the amplitude and phase fluctuations observed at the two receivers and $\text{Si}(\cdot)$ is the sine integral function defined as

$$\text{Si}(x) = \int_0^x \frac{\sin(u)}{u}\,du \quad .$$

It was also shown by Chernov that the values for these coefficients are near unity when $\ell \ll a$, and decrease to zero when $\ell \gg a$. Although this result is derived for the case of the Gaussian correlation coefficients, it has been shown to be true for a wide class of correlation coefficiency by Tatarski[7] (p. 146). Thus, the measurement of these coefficients can provide a powerful method for determining the correlation distance of the random medium, which is an important parameter.

An indication is now given of the manner in which Chernov's theory of wave propagation in a random medium was used to characterize random properties of the crust and upper mantle under LASA, using the P-wave anomaly data presented previously. Toward this end, it is necessary to investigate the way in which the P-wave, or compressional, velocity varies with depth beneath LASA. A series of seismic refraction profiles have been made at LASA by Borcherdt and Roller,[8] Warren, et al.,[9] and Gibbs.[10] In addition, there are studies of the velocity structure in the upper mantle for the western continental United States made by Niazi and Anderson,[11] Archambeau, et al.,[12] and Bolt and Nuttli.[13] If an attempt is made to combine all the preceding results about the velocity structure in the crust and upper mantle, a velocity structure such as

that in Fig. II-4(a) may be obtained. The hyperfine variations in the velocity structure have been placed there in order to explain the mechanism which causes the P-wave anomaly data at LASA, and do not exist in any of the preceding works. The results shown in Fig. II-4(a) pertain to a particular point on the surface of the earth, and the velocity structure (as a function of depth) will change as this point is allowed to vary. This variation between two sets of results will be small if the points are within a correlation distance of each other. This correlation distance was measured and found to be about 12 km, as will be discussed subsequently.

The velocity structure in Fig. II-4 shows the velocity varying randomly about 8 km/sec in the upper mantle, at approximately 60- to 200-km depth. The influence of the low-velocity zone at depths between 90 and 150 km is also noted. The velocity change due to the Mohorovicic discontinuity probably occurs at about 50 km, while there is another sudden change at about 20 km. In addition, there is a large change in velocity that occurs about 5 km beneath the surface due to sedimentary layers.

Unfortunately, the velocity structure shown in Fig. II-4(a) does not correspond to that which would be expected in a random medium which is spatially homogeneous and statistically isotropic. That is, the correlation function for the index of refraction of such a medium depends on position in the medium and not just on differences in position, as discussed previously. There appears to be no simple way to modify Chernov's results to take this nonhomogeneous and non-isotropic condition into account. Thus, in order to use the results given by Chernov, it is necessary to make some simplifying assumptions about the velocity structure, but yet retain the essence of this variation. Such a simplified velocity structure is shown in Fig. II-4(b). It is possible to replace the velocity structure in Fig. II-4(b) with that in Figs. II-4(c) and (d), which depict the velocity structure for a random and a deterministic medium, respectively. In other words, as a gross approximation, it is possible to consider the amplitude and phase fluctuations produced by propagation through the medium with velocity structure given in Fig. II-4(b) as equivalent to those produced by propagation through the medium whose velocity structure is given in Fig. II-4(c), followed by the medium whose structure is shown in Fig. II-4(d). An assumption has also been made that the sedimentary layers play a relatively minor role in causing the P-wave anomalies at LASA. This is a simplifying assumption that cannot be completely justified at this time.

Thus, the problem of considering the effect of the crust and upper mantle on P-waves was reduced to that of considering the random, or Chernov-type, medium in Fig. II-4(c), followed by the deterministic medium in Fig. II-4(d). The effect of the deterministic medium can be taken into account as follows. The x-axis in Fig. II-3 is oriented so that it lies along the direction of propagation of the P-wave defined by the refraction which takes place in the deterministic medium under LASA, as well as any other deterministic medium external to the LASA which lies along the propagation path, such as in the lower mantle (or source) region.

In order to use the results of Chernov on transverse autocorrelation coefficients to determine the correlation distance, it is necessary to measure the amplitude and phase fluctuations at the receivers located at the points P1' and P2 depicted in Fig. II-3; i.e., the two receivers should lie in the plane which is transverse to the direction of propagation of the wave in the left half-space, or x-axis. However, it is only possible to have receivers located at the surface of the earth at points P1 and P2, where P1 is the point of intersection of the surface with the line parallel to, and l km above, the x-axis, as shown in Fig. II-3. It can be shown that the correlation of the fluctuations between P1 and P2 is a good approximation for that between P1' and P2, since the correlation of the fluctuations between P1' and P1 is close to unity, as indicated previously.

35

It is now necessary to show how the amplitude and phase fluctuations, required in Chernov's theory, may be obtained from the P-wave anomaly data. In addition, it is also necessary to show how these quantities may be used to estimate the important parameters that characterize the random medium, which were discussed previously. A basic assumption is made that the P-waves for each event enter a random medium, which can be considered to be an independent realization from the ensemble of random media. In reality there is, of course, only a single random medium under LASA. However, this assumption is valid if the epicenters of the events are sufficiently separated from each other so that the P-wave trajectories for any given event, in the upper mantle, intersect a fixed horizontal plane, for example, about 200 km beneath LASA, at points which are more than a few correlation distances from those of any other event. Thus, the ensemble (or statistical) averages may be performed by averaging the results obtained for the individual events.

If the measurement for the relative power at the i-th subarray and j-th event is denoted by P_{ji}, then the amplitude fluctuation is defined as

$$B_{ji} = -c(P_{ji} - \hat{P}_i), \qquad j = 1, \ldots, 31 \quad ,$$

$$i = 1, \ldots, 9 \quad ,$$

where $c = \ln(10)/20$, and the average amplitude fluctuation is

$$\hat{P}_i = \left(\sum_{j=1}^{31} P_{ji} \right) \Big/ 31 \quad .$$

This definition for the amplitude fluctuation was found to give the best agreement of the experimental results with the theory given by Chernov. The estimate of the transverse autocorrelation coefficient for the amplitude fluctuations is obtained in the usual manner, cf., Cramer.[14]

In order to compute the phase fluctuation, it is necessary to know the phase, or time of arrival, of the diffracted wave at the receiver relative to that of a hypothetical homogeneous wave. The arrival time of this homogeneous wave is the time at which the wave in the left half-space, shown in Fig. II-3, would arrive at the receiver if the random medium in the right half-space were removed and replaced with a homogeneous medium similar to that in the left half-space. Thus, the phase fluctuation could be obtained if the equiphase (or isochron) contours for both the diffracted wave and the homogeneous wave were known for each event. However, the slowness anomaly data for each event can be used only to obtain the gradient of the equiphase contours at a particular point. Thus, it is necessary to obtain the equiphase contours from the value of its gradient evaluated at nine different points in space.

The equiphase contours were obtained by performing a least-squares fit of their gradients to the measured gradients. The phase fluctuation for the j-th event and at the i-th subarray, denoted S_{ji}, $j = 1, \ldots, 31$, $i = 1, \ldots, 9$, is then obtained from the equiphase contours in the usual manner. The estimate of the transverse autocorrelation coefficient for the phase fluctuations, as well as the crosscorrelation coefficient between the amplitude and phase fluctuations, is computed in a manner similar to that for the amplitude fluctuations. In addition, the estimate for $\overline{B^2}$ and $\overline{S^2}$, denoted by P_b and P_s, respectively, are computed in the standard manner, cf., Cramer.[14]

It is possible to plot the theoretical relationship between $\overline{B^2}/\overline{S^2}$ and R_{bs} for various values of the wave parameter, as shown in Fig. II-5. In addition, the 90-percent-confidence region is shown in this figure. It was found that $P_b = 0.14$, $P_s = 0.27$, so that $P_b/P_s = 0.52$, and that the estimate for the crosscorrelation coefficient is 0.23. This pair of measurements is shown in Fig. II-5, along with the 90-percent-confidence region for D = 6. Thus, the wave parameter D was estimated to be equal to six, as this appears to give the best correspondence between the data and the theory. The fact that the measurement lies so far from the theoretical curve in Fig. II-5 could be explained solely on the basis of the finite sample sizes used in the estimation procedures. However, it is quite likely that part of the reason for the departure of the measurement from the theoretical results is due to some of the basic assumptions not being satisfied. For example, the assumptions concerning the spatially homogeneous and statistically isotropic random medium are clearly not satisfied. In view of this, as well as some of the other assumptions which have been made, the agreement of the measurements with the theory can be considered to be quite good.

The results obtained for the estimates of the transverse autocorrelation coefficients of amplitude and phase fluctuations are shown in Figs. II-6(a) and -7(a), respectively. It is seen from these figures that the coefficients display a large amount of variation, so that some smoothing was employed to improve the stability of the results, as shown in Figs. II-6(b) and -7(b). Also depicted in these figures are the theoretical results given by Chernov[6] for $R_b(\ell)$ and $R_s(\ell)$, presented previously, for a wave parameter D equal to six and correlation distance a of 12 km. There seems to be reasonably good agreement between the experimental and theoretical results in these figures, so that it may be concluded that a good estimate for the correlation distance at LASA is 12 km.

It is now possible to compute an estimate for the extent of the random medium L. The mean velocity of the random medium is $c_o = 8$ km/sec, and the frequency f = 0.8 Hz, so that $\omega = 2\pi(0.8) = 5.02$ rad/sec. Hence, the wavenumber of the homogeneous wave is, $k = \omega/c_o = 2\pi(0.8)/8 = 0.63$ rad/km, and the wavelength $\lambda = 2\pi/k = c_o/f = 10$ km. Hence, using the defining equation for D we have

$$L = ka^2 D/4$$

$$= (0.63)(12)^2(6)/4$$

$$= 136 \text{ km} \quad .$$

It is also possible to compute an estimate for the standard deviation of the index of refraction, $(\overline{\mu^2})^{1/2}$, using the two relationships given by Chernov (pp. 82-83) for $\overline{B^2}$, $\overline{S^2}$. Each equation yields a different value, so that the procedure used was to average the two values to obtain the final estimate. Thus, it is obtained that an estimate of $(\overline{\mu^2})^{1/2}$ is 0.019. Hence, there appear to be variations in the index of refraction, on the order of 1.9 percent, distributed throughout the crust and upper mantle, to a depth of more than 100 km, as shown in Fig. II-8, which appear to be causing the P-wave slowness anomalies between subarrays at LASA. What can be inferred from these results? It must be emphasized that they in no sense prove the existence of a random medium under LASA. It may be possible to find a set of corrugated interfaces which can explain the amplitude and phase anomalies. This has not been possible for a single interface (see Sec. I-F). What has been presented is an estimate of random media parameters which are appropriate if we choose to describe the data in terms of Chernov theory. It should be mentioned

that similar results have been obtained recently by Aki.[15] A more detailed description of the present results will be presented in a forthcoming publication.[16]

<div align="right">J. Capon</div>

C. LIMITATIONS IMPOSED BY A RANDOM MEDIUM ON THE ABILITY TO MEASURE dT/dΔ WITH LASA

The LASA, as well as other array, data have been used in the past in attempts to determine various regions of heterogeneity within the earth. A discussion will now be presented of the capability of the LASA to determine such regions. In particular, we consider only those methods based on the analysis of the P-wave travel-time derivative, dT/dΔ. In these investigations dT/dΔ vs Δ is measured for a particular set of azimuths and compared with a standard, such as the Jeffreys-Bullen (J-B) curve, which is considered reasonably valid for all azimuths. Any significant differences between the two curves is interpreted as implying the existence of inhomogeneities in the earth, usually deeper in the mantle, c.f., Chinnery and Toksöz,[17] Johnson,[18] Corbishley.[19]

Consider the various sources of inhomogeneity. There may be various inhomogeneous regions within the earth that cause the curve for dT/dΔ vs Δ to be azimuthally dependent, when measured at a particular array. In addition, this curve will be different when measured at different arrays. These inhomogeneities may be described broadly as due to the following causes.

    (1)   Random part of local crust and upper mantle structure at the receiver.

    (2)   Deterministic part of local crustal structure at the receiver.

    (3)   Propagation path effects, primarily deeper in the lower mantle.

    (4)   Source region effects, due to structures such as dipping plates of lithosphere.

The description of the crust and upper mantle structure at LASA as a random medium, given in item (1), has been presented in Sec. II-B, along with a detailed description of its properties. This represents the first time that such a characterization has been attempted at LASA. The effects due to the structure in item (2) are approximately the same as those due to a plane-dipping interface. The inhomogeneities in the lower mantle, given in item (3), have been discussed by Chinnery and Toksöz[17] and Johnson,[18] while those in the source region, given in item (4), were discussed by Davies and McKenzie[20] and Jacob.[21] The only structure listed in items (1) − (4) which can cause amplitude and phase variations between subarrays, for a given event, is the random medium given in item (1). This is readily apparent and may be seen quite clearly from some of the ray tracing results in arbitrarily heterogeneous media given by Julian.[22] These results apply quite readily to the structures listed in items (2), (3) and (4), and show that these structures must produce amplitude and phase variations that are constant over the aperture of LASA, for a given event. It has been shown in the last SATS (Fig. III-3)[1] that the standard deviations of these variations are comparable, or larger, than their average for each event, which must, of course, be due to the structures in items (2), (3) and (4). Thus, it follows that the structure in item (1) could be one of the primary causes of the P-wave anomalies at LASA. However, contributions to the P-wave anomalies, as observed on individual sensors, due to the structures listed in (2), (3) and (4), are also significant. In other words, all of these structures may be of importance in contributing to P-wave anomalies observed on individual seismometers.

A method which has been used to measure dT/dΔ for the entire LASA is to note the P-wave arrival times at the center of the subarrays located in the three outer rings, D, E and F, and

to find the slowness of a plane wave whose arrival times best fit the measurements in a least-squares sense. We now consider the effect of the errors introduced by a random medium alone on this measurement. The standard deviation of the relative error in $dT/d\Delta$ for this method has been given by Kelly[23] as

$$\sigma_S = \sqrt{\frac{6}{N}} \frac{\sigma_\tau v}{\ell}$$

where N is the number of subarrays used, σ_τ is the standard deviation of the arrival time measurement (in sec), v is the horizontal phase velocity of the P-wave for a particular distance (in km/sec), and ℓ is the aperture of the array (in km). It can be shown that the effect of the random medium is to introduce timing errors whose standard deviation is about 0.10 sec. Thus, using v = 20 km/sec, corresponding to a distance of about 80°, N = 12 and ℓ = 200 km, we obtain

$$\sigma_S = \sqrt{\frac{6}{12}} \frac{(0.1)(20)}{200}$$

$$= 0.007 \quad .$$

Hence, the 95-percent-confidence limits, due to the effect of the random medium, for the measurement of $dT/d\Delta$ at LASA are about ±1.4 percent.

Thus, if random medium results are applicable, inferences from $dT/d\Delta$ data may not be significant to better than ±1.4 percent. In order to be able to say that such differences are due to velocity variations in the lower mantle, item (3), or in the source region, item (4), it is necessary to have differences that exceed ±1.4 percent, and the effect of the local crustal structure in item (2) must be adequately taken into account. However, this level of the difference was exceeded in the analysis of Chinnery and Toksöz,[17] so that it is probably that the differences they observed were due to velocity variations in the lower mantle, as they claim, and not due to the random medium. It is also possible to say that this same statement applies to Johnson,[18] since he used data at the Tonto Forest Observatory (TFO) and the effect of the random medium may be comparable to that at LASA.

The random medium has a small effect on the ability to measure $dT/d\Delta$ with LASA, and only contributes what may be termed a small experimental error. However, this may not be true if the aperture of the array used in the measurement of $dT/d\Delta$ is significantly less than the 200-km aperture of LASA. Some care must be exercised in ascribing the cause of differences between the measured, and the J-B, curve for $dT/d\Delta$, to any one of the structures listed in (2), (3) or (4).

J. Capon

D. BODY-WAVE MULTIPATHING

The two most fundamental requirements of an array of N sensors are that it should be capable of improving the SNR by something approaching $\sqrt{N}$ and that it should have a directional capability to discern signals arriving in different directions simultaneously. Much documentation exists for LASA's ability to meet these requirements, but a new and instructive example has arisen recently which is particularly relevant to the problem of detecting the body waves of events in the presence of interfering (and probably larger) signals.

A study has been made of directions of approach of P-waves at individual subarrays of LASA. Earliest results from it were reported by Capon in the last SATS.[1] More recent results are reported elsewhere in Sec. II-A. We selected a few events for further study, particularly for

frequency dependence of this approach angle. In most cases we found no systematic frequency
dependence, but one event was exceptional. Observations of an intermediate focus earthquake
in North Colombia (11 September 1966) which would have a theoretical $dT/d\Delta$ of 7.6 sec/deg and
an azimuth of 134°, showed that energy at the low frequency end of the spectrum (0.6 to 0.8 Hz)
consistently approached from a direction significantly different from that of the high frequency
(1.1 to 1.3 Hz) energy. In Fig. II-9 we show a high resolution plot of the frequency wave-number
spectrum at 0.8 and 1.2 Hz for subarray B4. Neither frequency approaches at the theoretical
direction, but the absolute position of individual power peaks means little, as geological structure
in the vicinity of a subarray may severely bias the arrival direction. However, differential posi-
tions should be significant. Thus, we have plotted for each subarray low and high frequency
points in an "array diagram." The vectors joining mean low frequency and mean high frequency
positions for all 9 subarrays within the C-ring are shown in Fig. II-10, where it is apparent that
they do not have a zero mean. The effect is dominantly an azimuthal one. (We infer that low and
high frequency energy approach LASA on azimuths differing by 10° to 20°.) We cannot tell whether
either direction of approach is the "correct" one without a detailed analysis of subarray structure,
but for the purpose of this study this is unnecessary. Both signals arrive at almost the same time
so the most reasonable explanation would be that both follow non-great circle paths, one each side
of the theoretical path. The spectra of these two signals are significantly different. Propagation
in regions of strong lateral velocity gradients could account for this, but this is speculation.

We have also analyzed the center seismometers of subarrays out to the C-ring and these
taken as a whole also show the same effect. Figures II-11(a) and (b) show the conventional
frequency-wave number plots at 0.6 and 1.2 Hz.

We believe that the source of this multipathing has to be sought beyond the immediate sub-
structure of the array, as the effect does not appear on events from other regions. We see pos-
sible causes as being restrained to be in the middle mantle where rays are traveling nearly hori-
zontally. Lateral velocity gradients at depths of up to 1200 km underneath Mexico, the Gulf of
Mexico and Florida might account for two refracted paths. Whatever the cause, it strongly
affects coherence of the P-wave across the array and leads to the need for a certain care in
describing array directional capability when the primary signal, at different frequencies, is
not from one unique direction.

D. Davies
J. Capon

E. VELOCITY VARIATIONS IN THE LOWER MANTLE

The June 1972 SATS[1] contained a description of a P-wave travel time experiment which was
conducted using data from deep focus earthquakes exclusively. One of the most significant con-
clusions was that data at distances beyond 70° or so were found to contain anomalies which could
be explained satisfactorily only in terms of lateral velocity variations in the deep mantle. These
data have now been analyzed in more detail, and a refined estimate of the nature of the variations
has been obtained.

Owing to the uneven distribution of seismological observatories and deep earthquakes, the
sampling of the mantle provided by these data is also quite uneven, and it is impossible to deter-
mine uniquely the complete three-dimensional velocity structure of the mantle. What can be
determined is the average travel time residual for each of a number of "bundles" of rays following
nearly identical paths from a seismic region to a group of stations. For each path, a Student's

t test was used to evaluate the hypothesis that the travel time (after station corrections were applied) is the value given by the overall travel time curve and that deviations from this curve can be attributed to random measuring errors. Those ray paths for which the hypothesis could be rejected at the 99.5 percent confidence level were found almost exclusively at distances beyond 70°, implying that velocity variations near the bottoming points of the rays produce the travel time anomalies. Other effects, such as near-source or near-receiver velocity anomalies or event mislocation, are incapable of explaining the pronounced distance dependence observed.

The actual details of the velocity distribution cannot, however, be determined precisely, because rays travel a great distance at approximately the same depth near their turning points. Figure II-12 shows the regions of the lower mantle sampled by the various ray bundles (defined arbitrarily by the middle 30° of the rays) and indicates which paths correspond to early and late arrivals. Several interesting features of this figure should be noted. First, where regions overlap on the figure, they are generally consistent with each other (e.g., regions 1-6 and 1-7, and regions 2-2 and 2-3). This consistency is encouraging, in that it supports our argument that the travel time anomalies originate in the deep mantle and are not the result of some other type of systematic error. An apparent inconsistency exists between regions 1-3 and 1-16, but this is not surprising in view of the uncertainty as to exactly where the travel time anomalies actually originate. In fact, the rays following path 1-3 also pass through regions 2-2 and 2-3 further to the north, and it is likely that the travel time anomaly actually originates there. Another interesting feature of Fig. II-12 is a correlation between the anomalies in the two distance ranges (e.g., regions 1-7 and 2-7, regions 1-4 and 2-4, and regions 1-5 and 2-6), suggesting that the structure in the deep mantle has a spatial "coherence" of at least a few hundred km, vertically.

The mean travel times for the various ray bundles show a variation of about 1.5 sec for rays bottoming below 2600 km. This number is, of course, subject to some uncertainty, but it is nearly certain that the true travel time varies by at least 1 sec. The amount by which the actual velocity in the mantle varies depends on the size of the regions within which the variations occur. Figure II-12 suggests that the size of some of the anomalies, at least, is about 1000 km or less, in which case the velocity must vary by at least 1 percent. This figure is a lower bound, both because we have probably overestimated the scale of the inhomogeneities and because we are measuring averages of the velocity in rather large regions and some cancellation of the effects of positive and negative velocity anomalies is to be expected. Combined interpretation of travel time and $dT/d\Delta$ measurements can probably improve the resolution of structural details.

<div align="right">

B. R. Julian
M. K. Sengupta

</div>

F. EFFECTS OF THE SEDIMENTS AT LASA ON SHORT-PERIOD TELESEISMS

Data showing that the boundary between the sediments and basement under LASA is a strong scatterer of S-waves were presented in the June 1972 SATS.[1] It was further indicated that the boundary was dipping and that the resulting structure might account for some of the short period waveform anomalies observed at the array. Further data have now been analyzed in order to detail the nature of the boundary so as to calculate its effect on emerging P-waves.

Figure II-13 shows the azimuthal dependence of the amplitude ratio of the scattered S-wave to the scattering P-wave. The pattern indicates that the boundary is essentially planar and dipping to the southeast. To determine the dip, the same ratio was measured for events in the down-dip direction at various distances. The data are shown in Fig. II-14. The theoretical

curves for the structure shown in the figure were computed using the Jeffreys-Bullen dT/dΔ vs Δ values and plane wave-plane interface reflection coefficients, an example of which is shown in Fig. II-15. The S-wave velocity in the sediments was determined by using the P-scattered S arrival times and the P-wave velocity and sediment thickness given by Brown and Poort[24] from well log data. The calculated S-wave velocity indicates a Poisson's ratio of 0.38. Such a value is indicative of the clastic sediments at LASA. The best fitting curve in Fig. II-14 is for a dip of 10 degrees. The technique is in fact quite sensitive to the dip of the layer.

To examine the effects of the structure, the amplitude and direction of the primary wave and higher order multiply reflected waves were calculated. Two examples are shown in Figs. II-16 and -17. For events whose P-waves emerge from the down-dip direction, a first multiple P-wave with an amplitude of about 0.4 of the primary wave (it will be out of phase) will be mixed with the primary at an offset equal to the two way travel time in the crust. Higher order multiples will be down by an order of magnitude as will the first order multiple for events whose P-waves emerge from the up-dip direction. The two-way travel time for a P-wave in the crust will be approximately 2.25 sec. Figure II-18 shows the P and SV components of 2 events from the down-dip direction. The SV components have been shifted so that they are directly beneath the scattering P-wave. P-wave motion without corresponding S-wave motion indicates that the P-wave motion was generated above the sediment-basement boundary and is not source motion. The arrivals marked P_r have the corresponding time amplitude and phase of the proposed first order multiple. Allowing for the fact that the depth of the boundary varies from 1800 to 3400 m over the array[24] and that its dip and direction is probably nearly random from subarray to subarray with magnitudes of at least 10 degrees,[24] the observed short-period waveform anomalies may be due to the influence of the layer. However, only about 30 percent of the amplitude anomalies at LASA can be explained by the structure. Thus, while the upper-crust has a significant effect on short-period waves, it is only partly responsible for the behavior of short-period P-waves observed at the array.

<div align="right">T. Landers</div>

REFERENCES

1. Seismic Discrimination SATS, Lincoln Laboratory, M.I.T. (30 June 1972), DDC AD-748304.

2. E. B. Manchee and D. H. Weichert, "Epicentral Uncertainties and Detection Probabilities from the Yellowknife Seismic Array Data," Bull. Seismol. Soc. Am. 58, 1359-1377 (1968).

3. L. P. Vinnik and A. V. Nikolayev, "The Velocity Profile of the Lower Mantle from Direct Measurements of dT/dΔ," Izv. Akad. Nauk. Fiz. Zemlya. 11, 24-40 (1970).

4. D. Davies and R. M. Sheppard, "Lateral Heterogeneity in the Earth's Mantle," Nature 239, 318-323 (1972).

5. M. Niazi, "Corrections to Apparent Azimuths and Travel-Time Gradients for a Dipping Mohorovicic Discontinuity," Bull. Seismol. Soc. Am. 56, 491-509 (1966).

6. L. A. Chernov, Wave Propagation in a Random Medium (McGraw-Hill, New York, 1960).

7. V. I. Tatarski, Wave Propagation in a Turbulent Medium (McGraw-Hill, New York, 1961).

8. C. A. Borcherdt and J. C. Roller, "Preliminary Interpretation of a Seismic-Refraction Profile Across the Large Aperture Seismic Array, Montana," NCER-2, U. S. Geological Survey, Menlo Park, California (1967).

9. D. H. Warren, J. H. Healy, J. Bohn and P. A. Marshall, "Crustal Calibration of the Large Aperture Seismic Array (LASA), Montana," NCER, U. S. Geological Survey, Menlo Park, California (1972).

10. J. F. Gibbs, "A Model for the Crust of the Earth under LASA from Crossed Seismic Refraction Profiles," NCER, U. S. Geological Survey, Menlo Park, California (1972).

11. M. Niazi and D. L. Anderson, "Upper Mantle Structure of Western North America from Apparent Velocities of P Waves," J. Geophys. Res. 70, 4633-4640 (1965).

12. C. B. Archambeau, E. A. Flinn and D. G. Lambert, "Fine Structure of the Upper Mantle," J. Geophys. Res. 74, 5825-5865 (1969).

13. B. A. Bolt and O. W. Nuttli, "P Wave Residuals as a Function of Azimuth, 2. Undulation of the Mantle Low-Velocity Layer as an Explanation," J. Geophys. Res. 74, 6594-6602 (1969).

14. H. Cramér, Mathematical Methods of Statistics (Princeton University Press, Princeton, New Jersey, 1946).

15. K. Aki, "Scattering of P-waves Under the Montana LASA," to be published.

16. J. Capon, "Characterization of Crust and Upper Mantle Structure Under LASA as a Random Medium," to be published.

17. M. A. Chinnery and M. N. Toksöz, "P-Wave Velocities in the Mantle Below 700 km," Bull. Seismol. Soc. Am. 57, 199-226 (1967).

18. L. R. Johnson, "Array Measurements of P Velocities in the Lower Mantle," Bull. Seismol. Soc. Am. 59, 973-1008 (1969).

19. D. J. Corbishley, "Multiple Array Measurements of the P-Wave Travel-Time Derivative," Geophys. J. Roy. Astron. Soc. 19, 1-14 (1970).

20. D. Davies and D. P. McKenzie, "Seismic Travel-Time Residuals and Plates," Geophys. J. Roy. Astron. Soc. 18, 51-63 (1969).

21. K. H. Jacob, "Global Tectonic Implications of Anomalous Seismic P Travel Times from the Nuclear Explosion Longshot," J. Geophys. Res. 77, 2556-2573 (1972).

22. B. R. Julian, "Ray Tracing in Arbitrarily Heterogeneous Media," Technical Note 1970-45, Lincoln Laboratory, M. I. T. (31 December 1970), DDC AD-720795.

23. E. J. Kelly, Jr., "Limited Network Processing of Seismic Signals," Group Report 1964-44, Lincoln Laboratory, M. I. T. (4 September 1964), DDC AD-447220.

24. T. Brown and J. Poort, "Subsurface Studies and Shallow Hole Preparation LASA Area, Eastern Montana," Technical Report No. 65-21, The Geotechnical Corporation (3 March 1965).
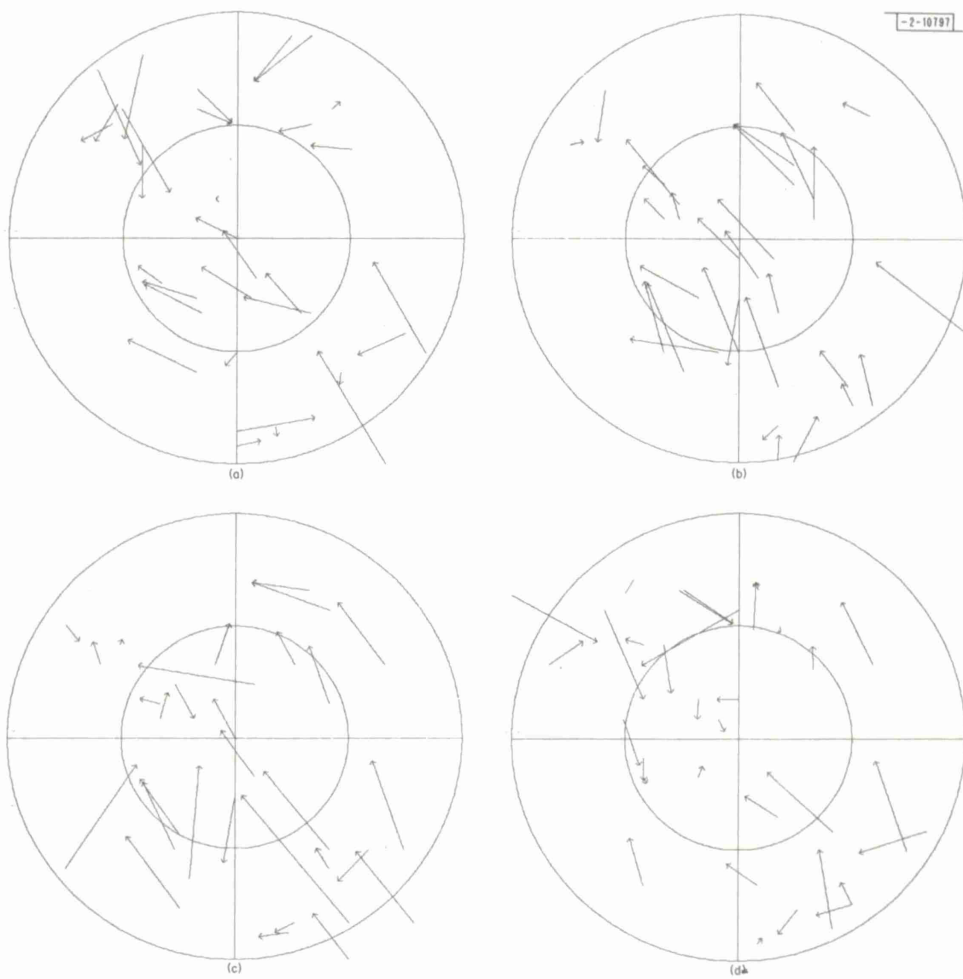
Fig. II-1. Subarray diagrams for B-ring at LASA: (a) site B1; (b) site B2; (c) site B3; (d) site B4. Outer circle radius is 10 sec/deg.

44
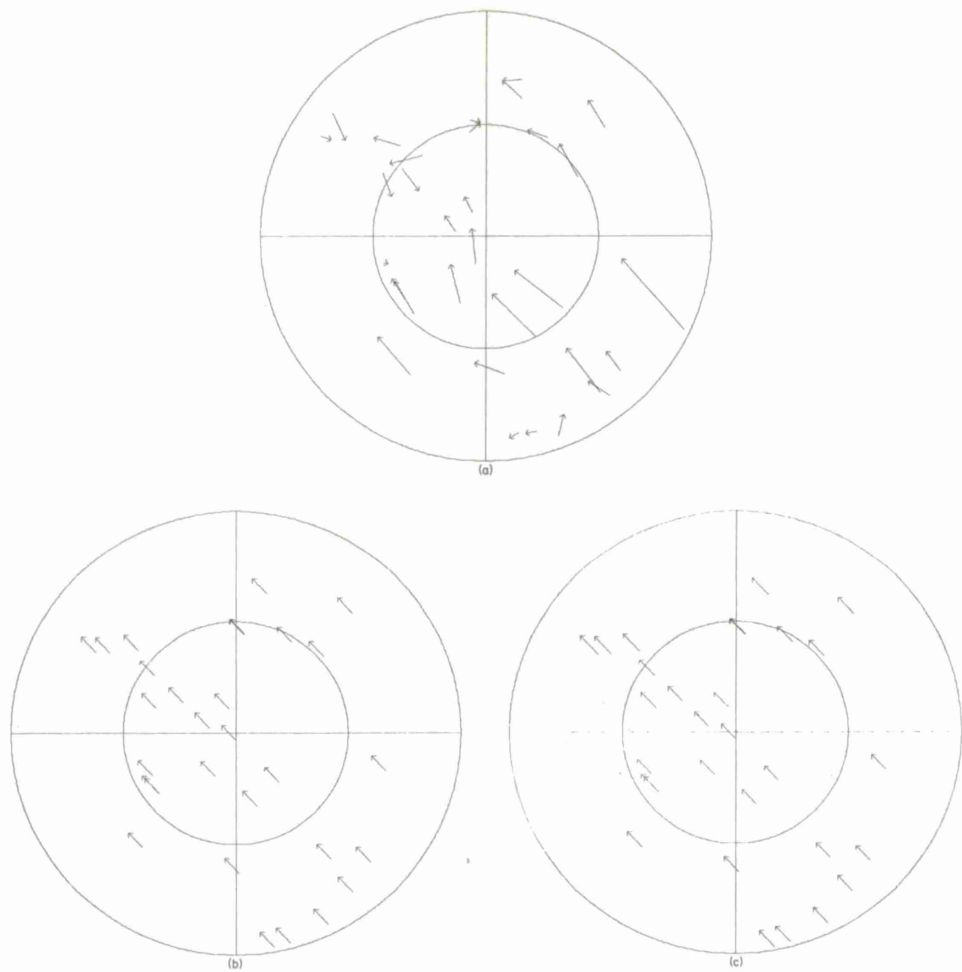
Fig. II-2. Subarray average (a), spatial average (b), and theoretical array diagram (c) for a plane-dipping interface. Outer circle radius is 10 sec/deg. For theoretical array diagram (c), dip = 11°, dip direction = 316°.
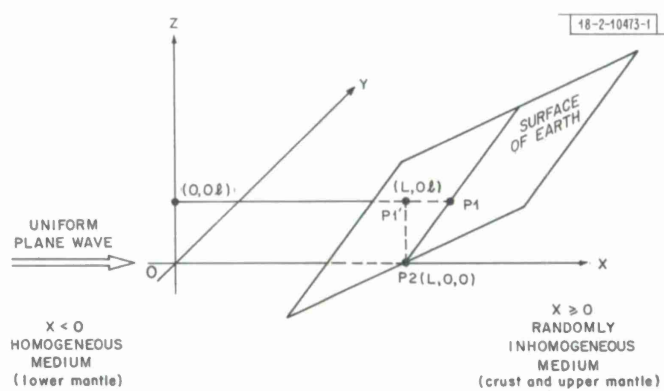

Fig. II-3. Illustration of model used by Chernov for wave propagation in a random medium.
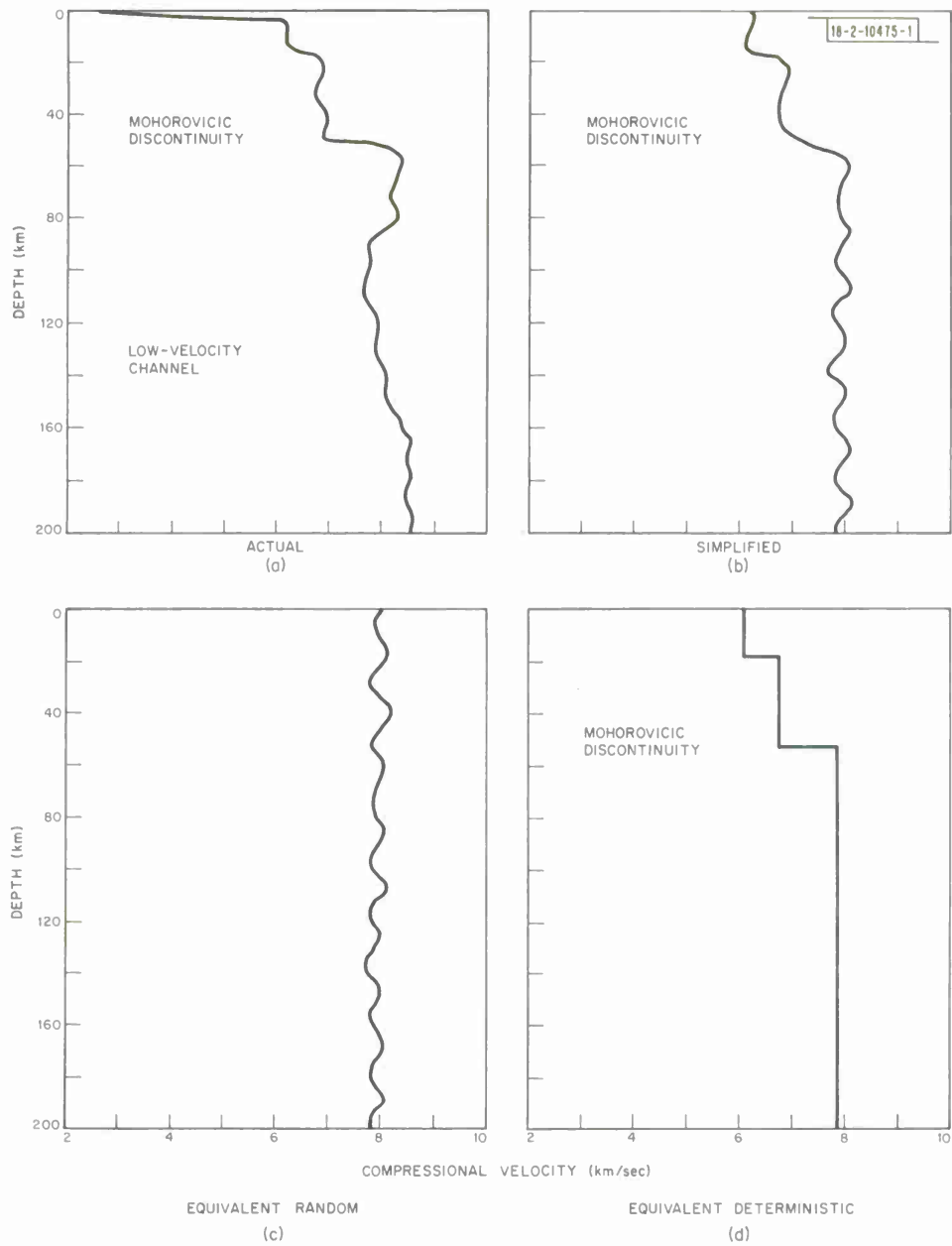
Fig. II-4.   Actual and simplified compressional velocity structures in the crust and upper mantle.
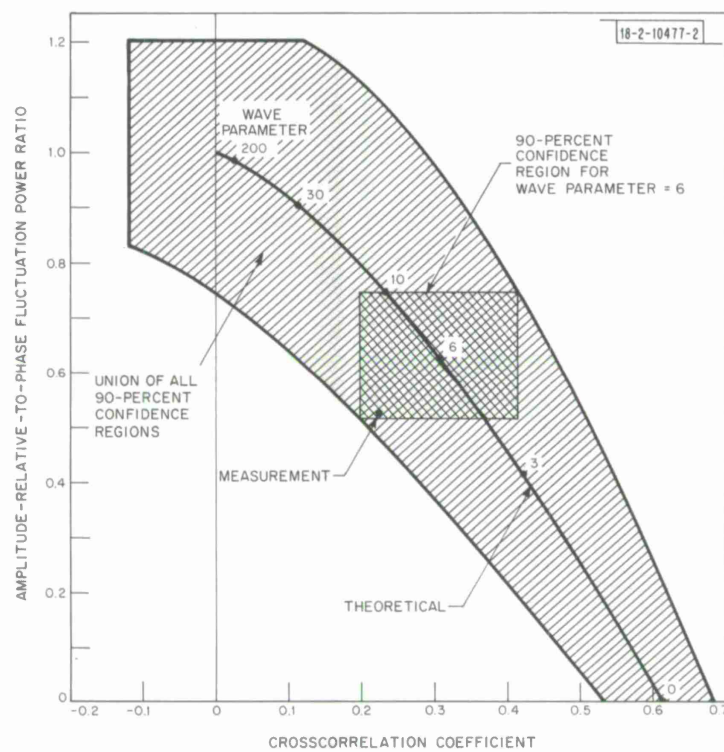
Fig. II-5. Theoretical relationship between amplitude-relative-to-phase fluctuation power ratio, and crosscorrelation coefficient between amplitude and phase fluctuation, and the 90 percent confidence limits of the measurement.
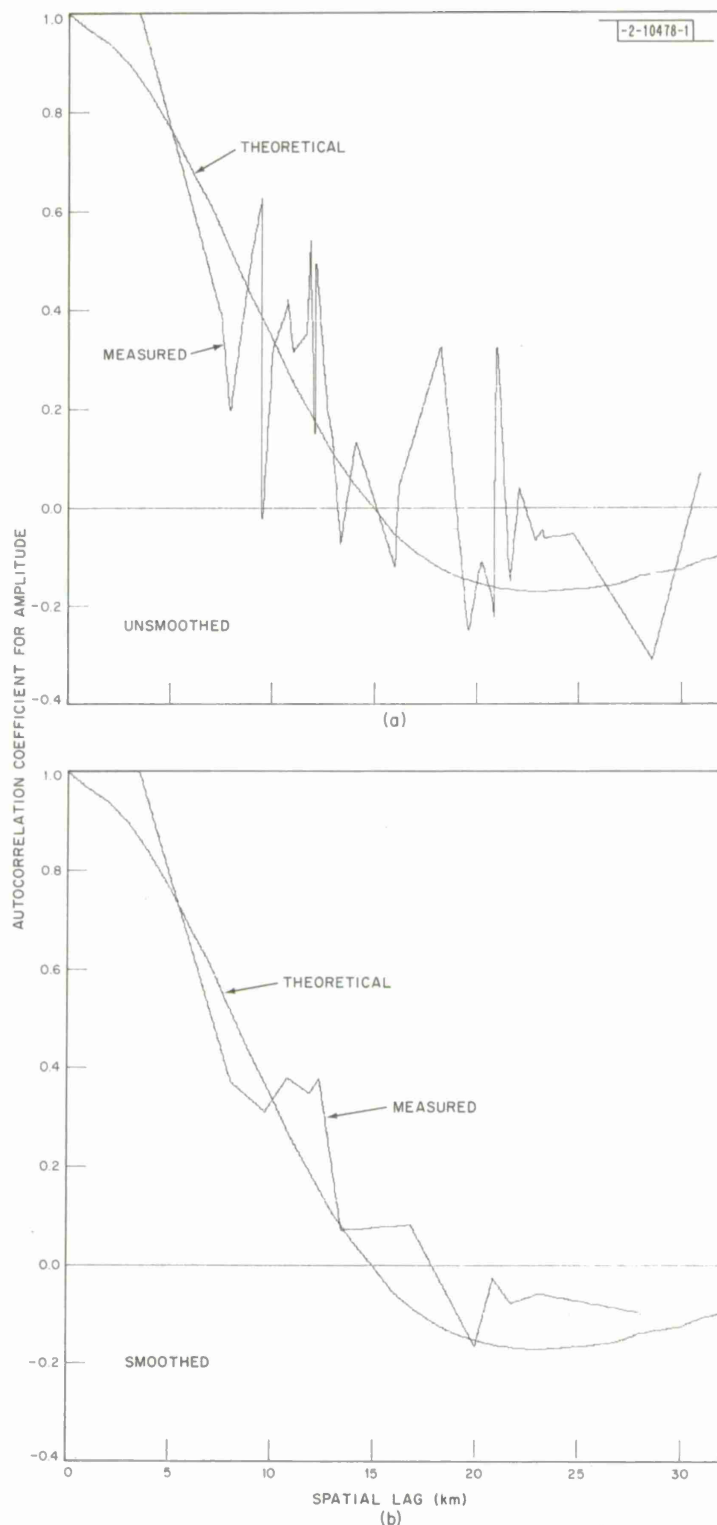
Fig. II-6. Comparison of unsmoothed and smoothed estimates with theoretical curve for transverse autocorrelation coefficient of amplitude fluctuations. Wave parameter = 6; correlation distance = 12 km.

48
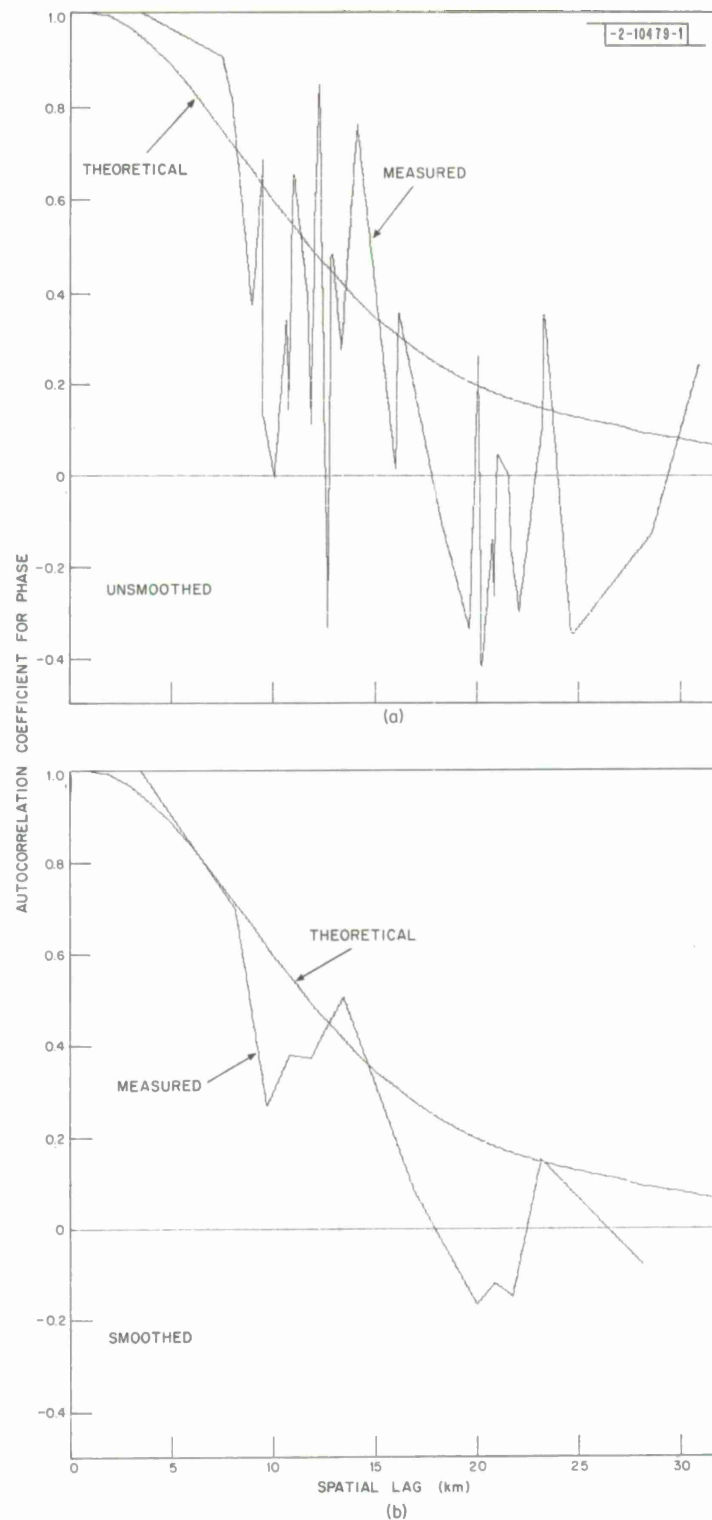
Fig. II-7. Comparison of unsmoothed and smoothed estimates with theoretical curve for transverse autocorrelation coefficient of phase fluctuations. Wave parameter = 6; correlation distance = 12 km.

COMPRESSIONAL VELOCITY

3.0 km/sec

6.1 km/sec

6.7 km/sec

MOHOROVICIC
DISCONTINUITY

1.9 PERCENT VARIATIONS
IN INDEX OF REFRACTION

8.2 km/sec

136 km

DEPTH (km)

18-2-10480-1
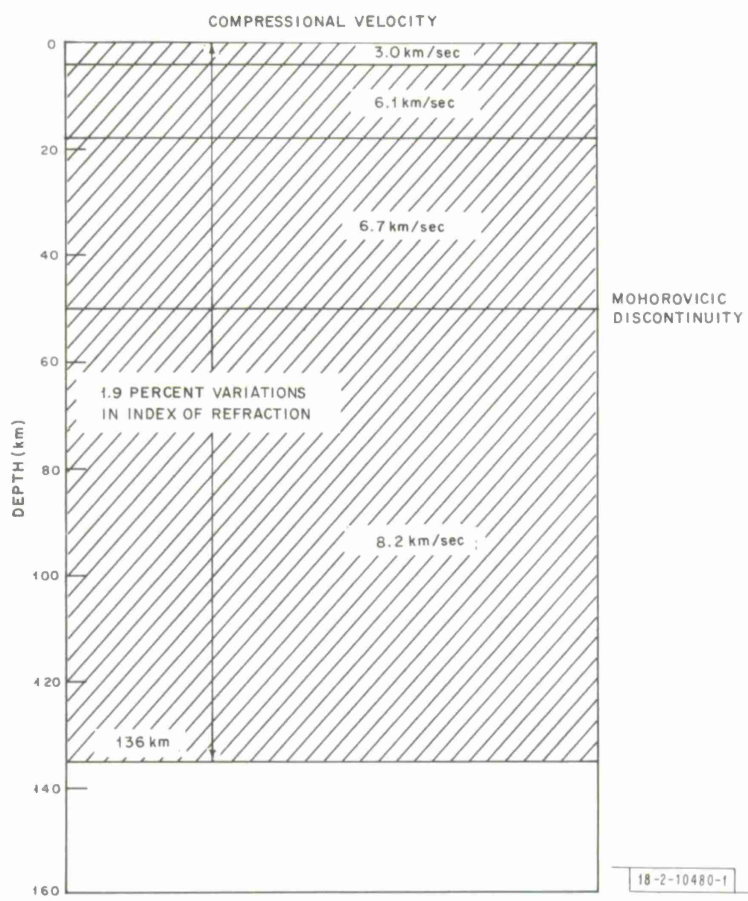
Fig. II-8.   Diagrammatic representation of crust and upper mantle
structure under LASA.
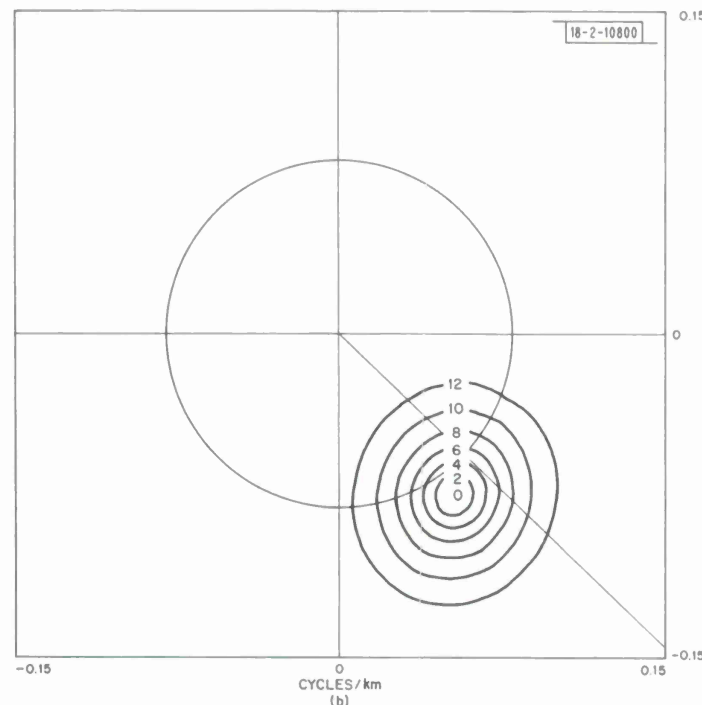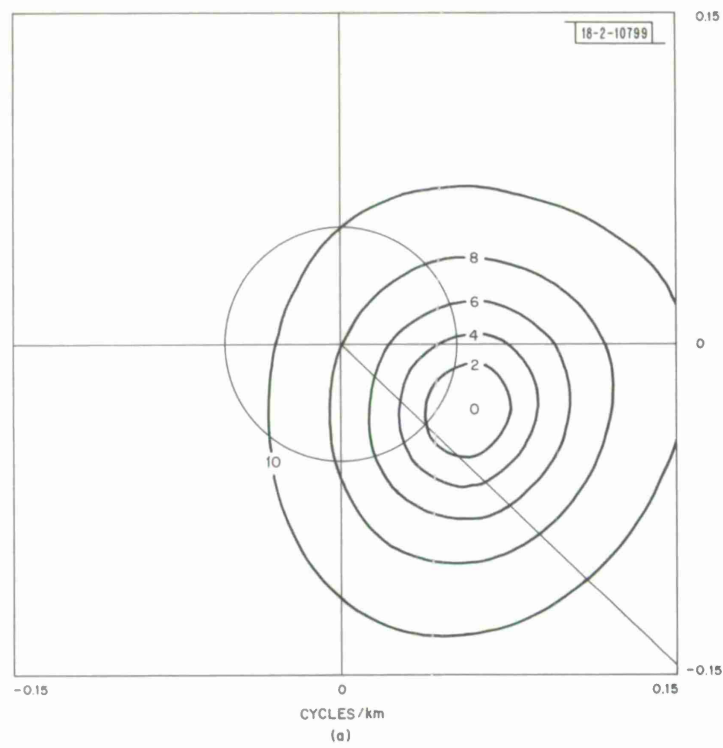
Fig. II-9. High resolution frequency-wavenumber spectra at 0.8 (a) and 1.2 Hz (b) for subarray B4 for a North Colombian event. Power peak is at 61.8, and 75.2 dB, respectively, above one quantum unit level. Contours are 2 dB apart.
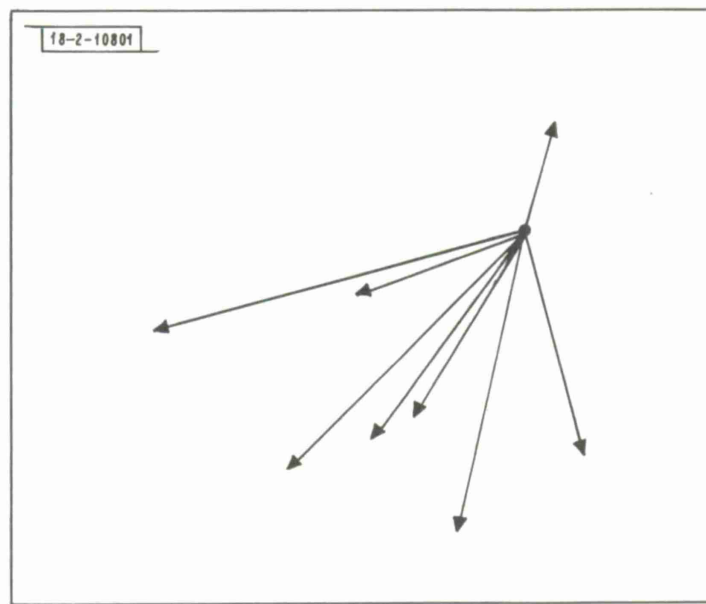
Fig. II-10. Distribution of vectors joining low to high frequency directions of approach in an array diagram for all subarrays within the C-ring. Mean implies an azimuthal separation of about 20°.
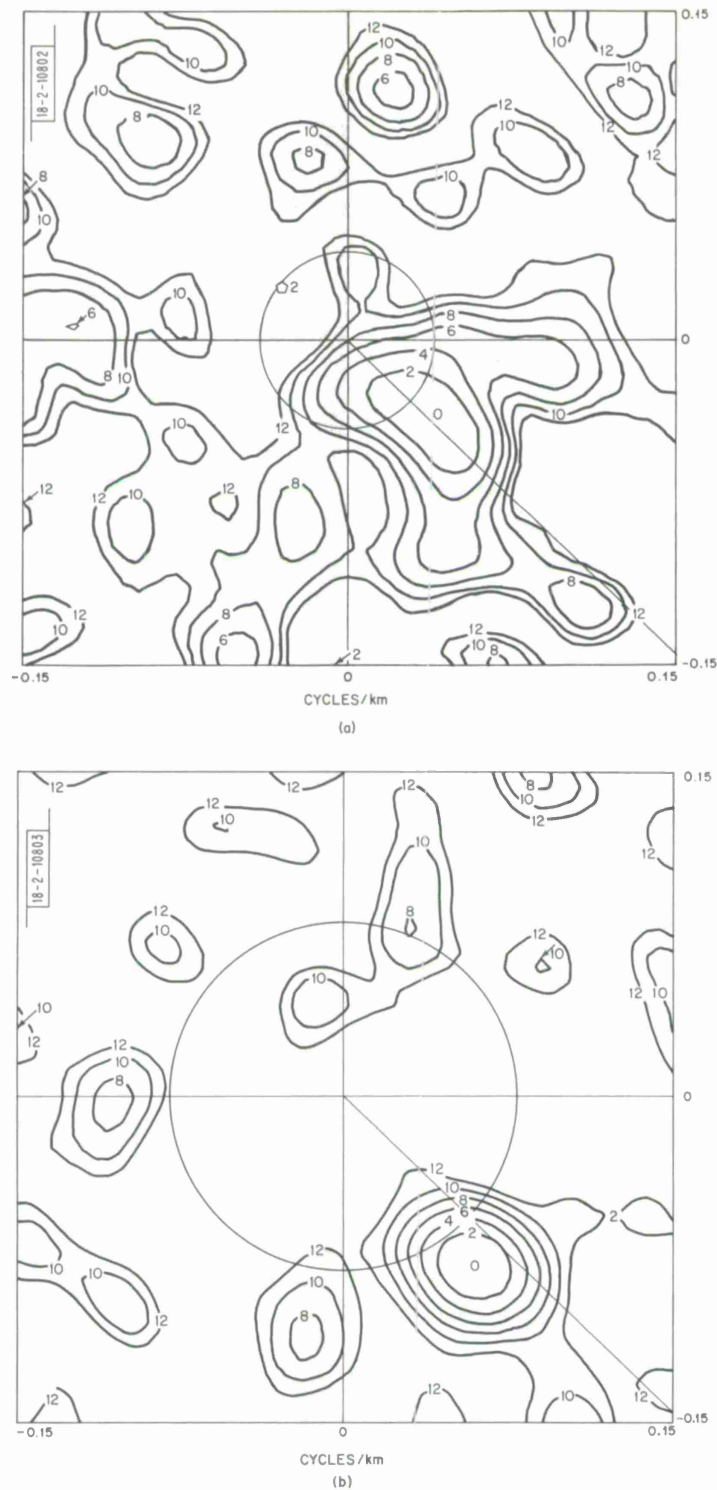
Fig. II-11. Conventional frequency-wave number spectra at 0.6 (a) and 1.2 Hz (b) for center seismometers of all subarrays out to the C-ring. Peaks are at (10.2, 131°) and (9.1, 142°), respectively. Intersection of circle and line is expected wavenumber.
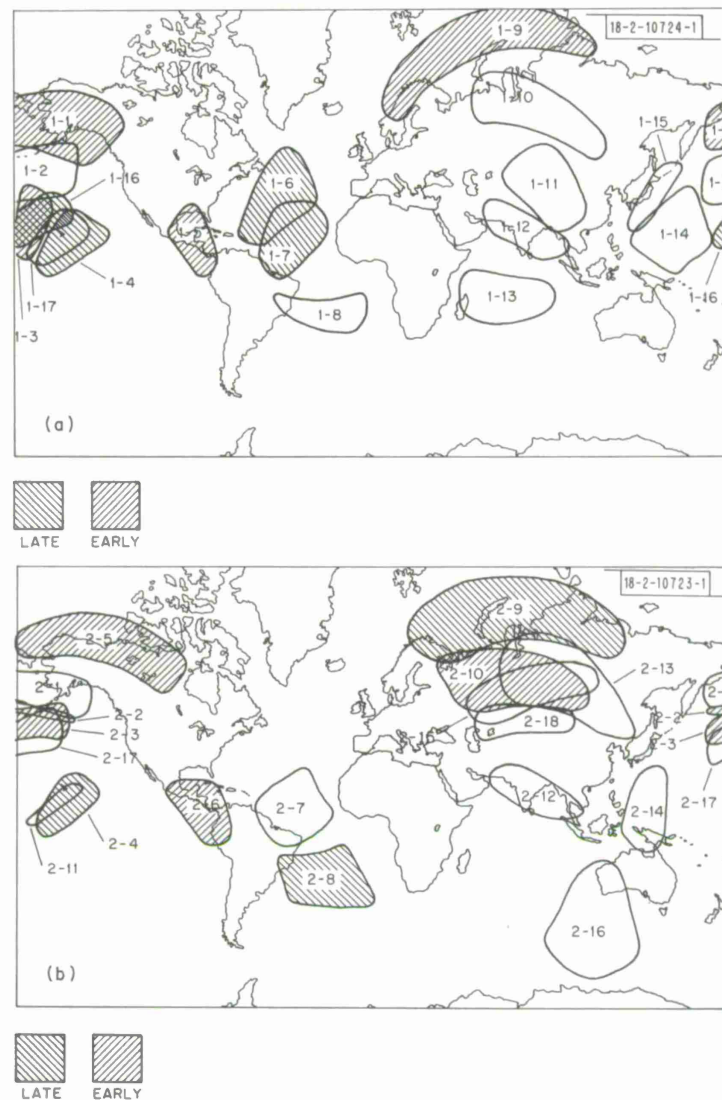
Fig. II-12. Regions of deep mantle sampled by "bundles" of observed rays. (a) 85° < Δ < 100° (depth 2600-2900 km); (b) 70° < Δ < 85° (depth 2000-2600 km).
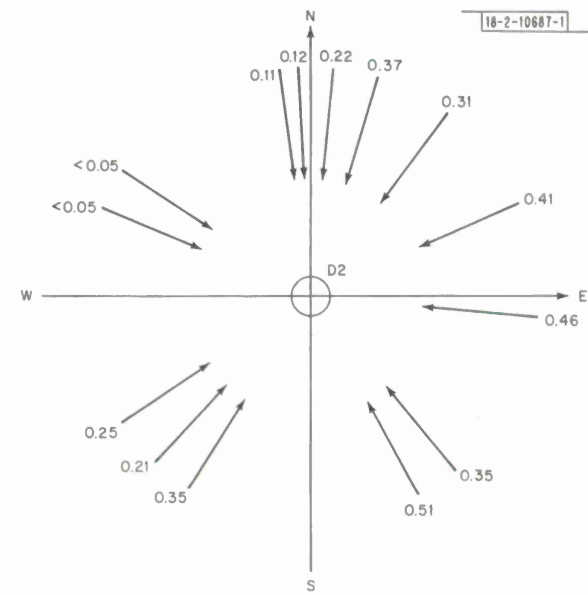
Fig. II-13. Azimuthal dependence of scattered S-wave amplitude indicating a layer dipping to the southeast.
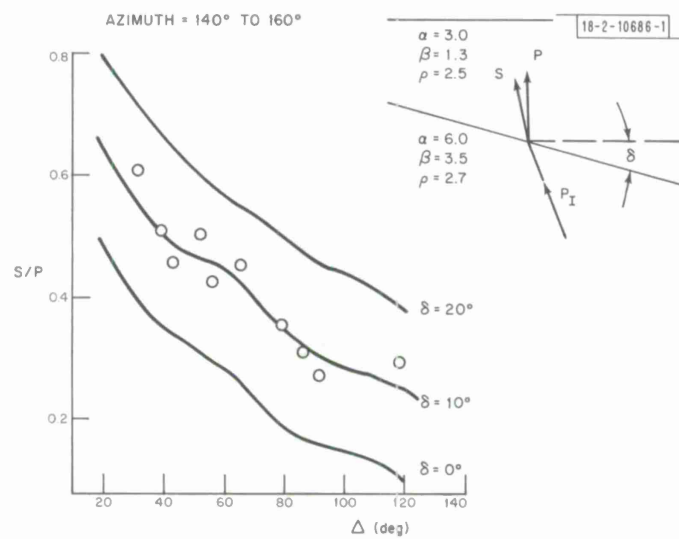

Fig. II-14. Distance dependence of scattered S-wave amplitude indicating a dip of 10 degrees exists at the scattering boundary.
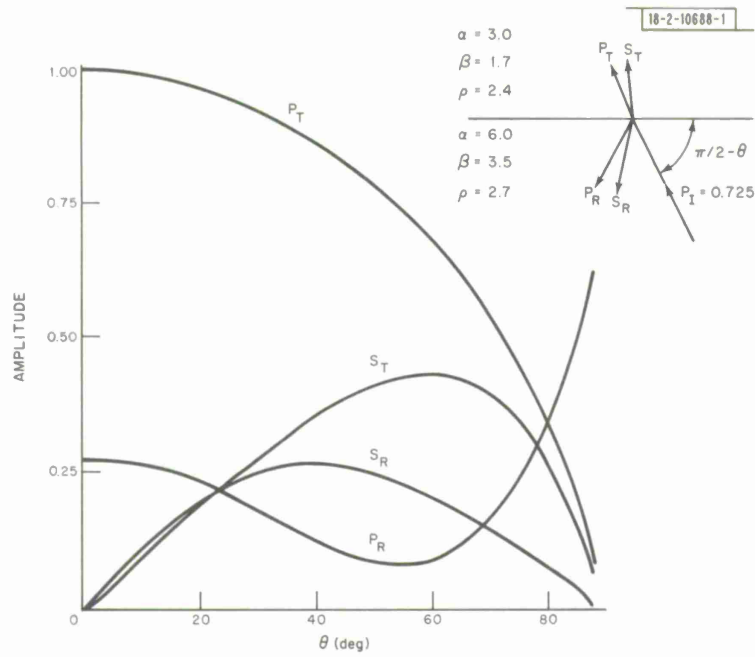
Fig. II-15. Amplitude of transmitted P- and S-waves and reflected P- and S-waves as a function of incidence angle for the structure shown.
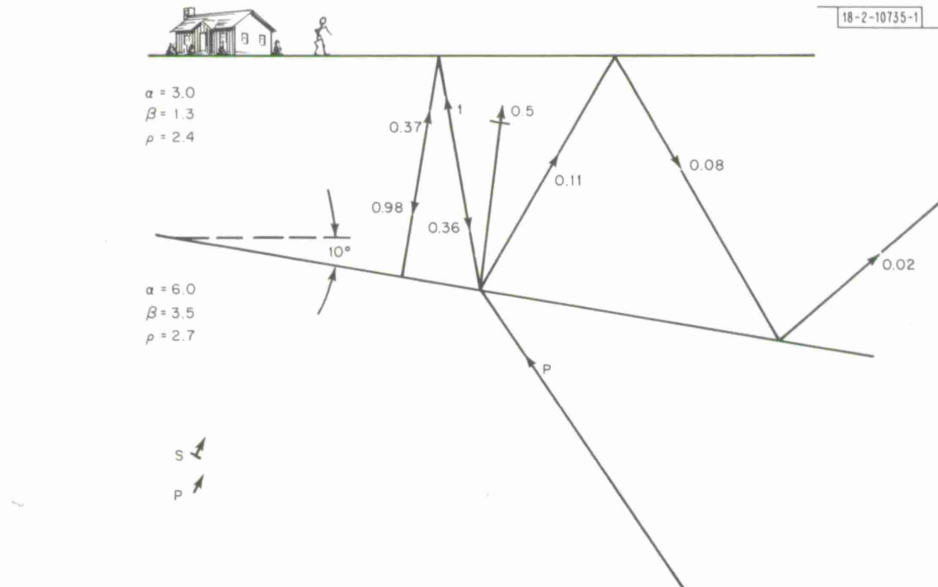
Fig. II-16. Ray paths and amplitudes of scattered waves for events emerging from down-dip direction.
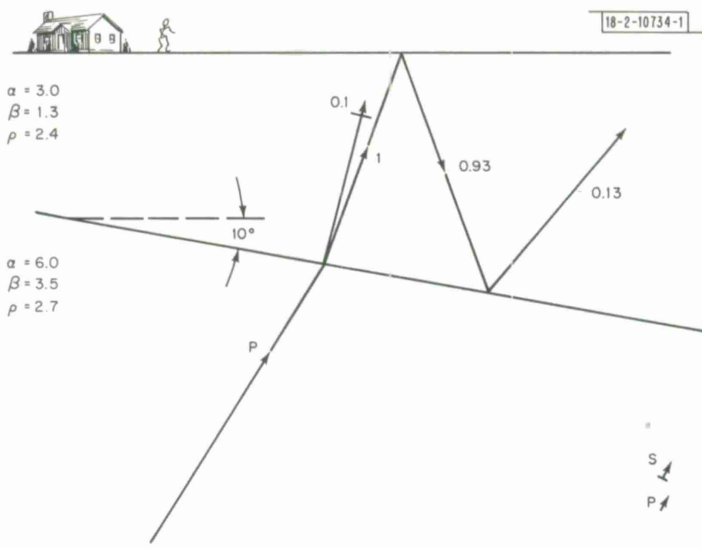
Fig. II-17.   Same as Fig. II-16 for events emerging from up-dip direction.
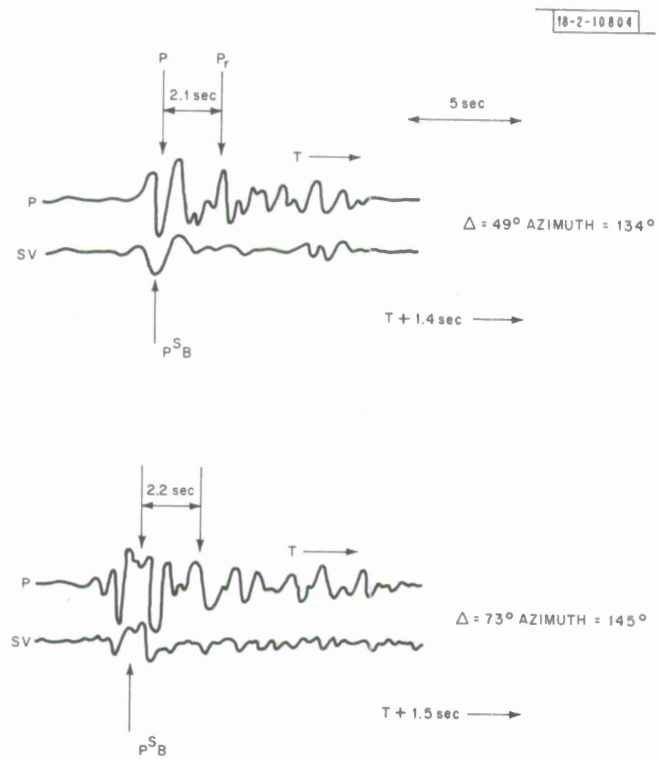
Fig. II-18.   Seismograms of P-waves from events in down-dip direction showing first order multiple (P_r).
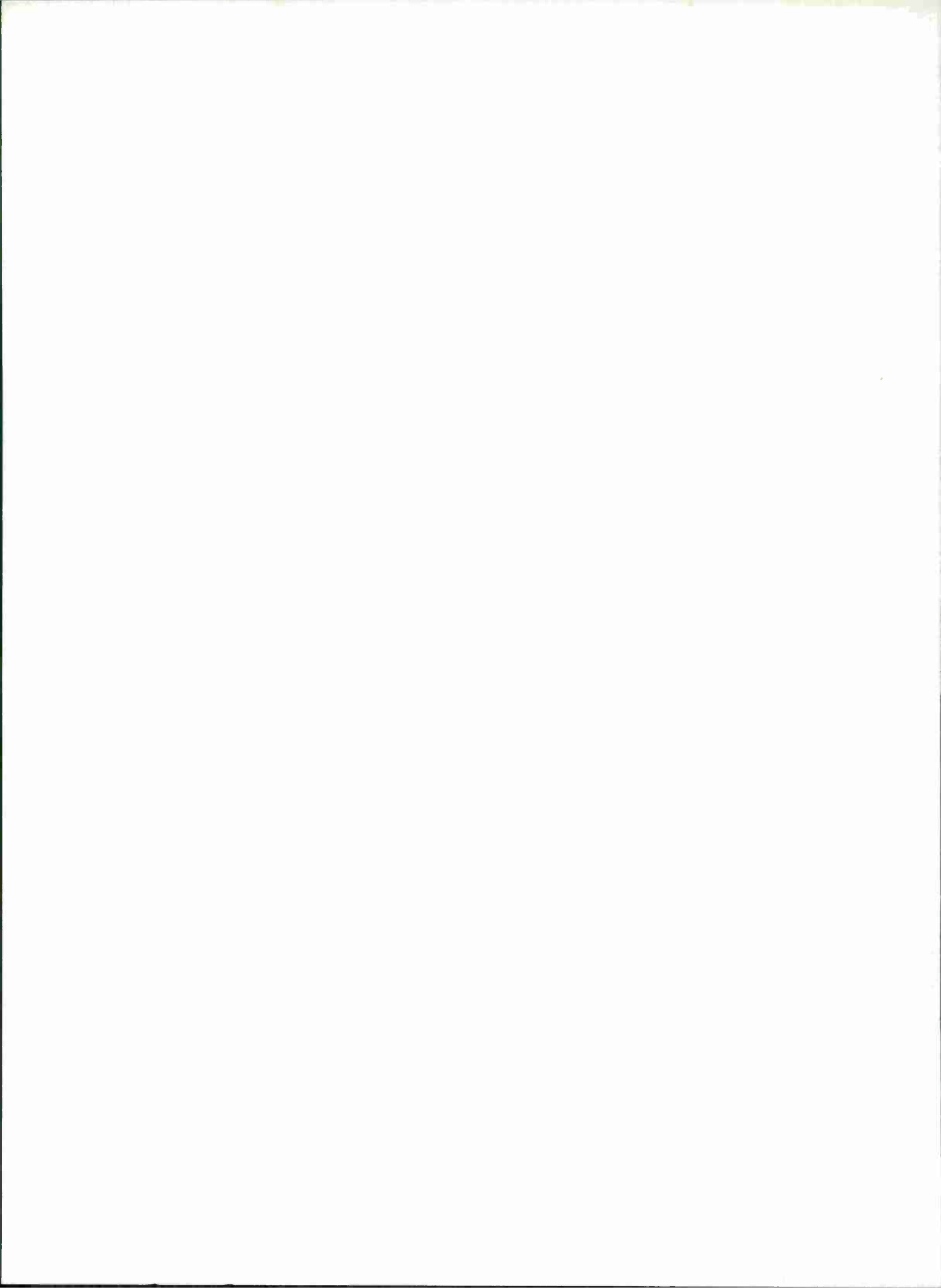
III. SOURCE STUDIES

A. FAULT PLANE SOLUTIONS IN ASIA

Because of the failure of certain Asian events (assumed to be earthquakes) to discriminate from explosions through the $m_b:M_s$ ratio (T. Landers in Ref. 1), we have begun a study into the seismicity and tectonics of central and eastern Asia.   In the initial phase of this study, we have collected first motion data in an effort to determine the orientation of various tectonic zones through fault plane solutions.   Since no clear, unique pattern has arisen to date, we shall only review our data and suggest tentative trends.

The seismicity map of the NOS, the base map of Figs. III-1 and -2, shows the location of earthquakes for the 1962-1969 period.   From this map it is clear that the seismicity of China, Tibet, Sinkiang, and the Mongolias shows no well defined trends.   Linear zones which characterize plate boundaries in other regions are not immediately evident here.   Rather the epicenters are widely scattered, except in a few regions where dense pockets of activity occur (37°N, 115°E near Peking, 37°N, 95°E in Tsinghai province, and 30°N, 95°E in eastern Tibet).   The historical record[2] shows a linear concentration (the Lanchow-Kunming Fault zone) of seismicity along the 103°E meridian, beginning at 24°N and running to 34°N where it disperses.   One branch of this activity then runs northeastward in an S-shaped pattern ending near Peking.   The fact that such patterns show only when historical data are considered indicates that the seismicity of these regions is a relatively low level when compared with the Hindu-Kush.   Further, the lack of earthquakes large enough for reliable fault-plane solutions at teleseismic distances makes the problem of tectonic interpretation more acute.

Using the first motions recorded on long period instruments of the WWSSN, we have constructed fault plane solutions of some 18 earthquakes.   The solutions, along with nine reported by Fitch[3] and five by Nowroozi,[4] are summarized in Fig. III-1.   The circles represent the lower hemispheres of equal area projections of the first motion data, the solid areas represent areas of compression.   The heavy lines on this map represent "main deep faults"[5] either traced (solid) or hypothetical (dashed).

In some cases these fault lines are parallel to possible fault planes suggested by the first motion data.   Earthquakes numbered 1, 2, 9, 14, 22, 23 and F6 are such examples.   Other solutions, however, such as 17 and F1, show fault planes nearly normal to the mapped faults.   Still others, notably 15 and 16, do not lie near any prominent surface fault feature.   As with the seismicity, these fault plane solutions yield no clear, simple pattern for the tectonics of this Asian region.   Most of Fitch's solution along the Himalayan front and Nowroozi's in the Hindu Kush indicate thrust faulting with compression from the south and west.   The solutions falling in northern Burma, eastern Tibet and southwestern China are quite a mixed bag.   Normal, thrust and strike-slip mechanisms are all present and we cannot, for discrimination purposes, exclude the possibility of any of these types.   Although Wilson[6] has suggested that the Lanchow-Kunming fault zone represents a plate boundary, our solutions in or near this zone do not indicate what the relative motions should be.

We have attempted to construe a motion pattern from poles of the auxiliary planes of the solution in Fig. III-1.   We start with a solution that shows a fault plane striking parallel to a mapped fault and then, in cases where neither plane is the obvious fault plane, pick that plane whose motion vector is most compatible with surrounding motion vectors.   Of course, such an exercise

does not yield a unique set of motions (or relative slip vectors). The motion vectors, which are pointing northerly near the bottom center of the map, swing to the west in the center of the map. These vectors are roughly parallel to the structural geologic trends of the region around the high angle intersection of the arcs representing the Himalayan and Burmese fronts. It appears as though this portion of Asia was being bent (or stretched) about a point in Assam.

Otherwise, the interpretation of Fig. III-2 indicates that northern China is subject to east-west, rather than north-south, shear. In these isolated fault plane solutions this is, at present, an arbitrary interpretation. More specifically, we feel we can state that the region of Tibet which yields explosion-like earthquakes is one of complicated tectonics not dominated by one type of focal mechanism.

<div align="right">J. Filson
S. Das</div>

B. A THRUST EVENT IN SOUTHERN IRAN

On 10 April 1972, a large destructive earthquake (NOS M_s 6.9) occurred near the town of Ghir, some 150 km south of Shiraz, Iran. The main shock was followed by many aftershocks, of which 25 were reported during the period 10 April to 25 May in the NOS Earthquake Data Reports.

Figure III-3 shows the fault-plane solution determined from the polarities of initial P-wave motions recorded at WWSSN stations. It proved impossible to draw two mutually orthogonal planes through the data when the focus was set in the upper mantle (P-wave velocity = 8.0 km-sec^{-1}), thus it was placed in the crust (6.8 km-sec^{-1}). This has the effect of plotting all stations closer to the center of the equal area projection, because of refraction at the Moho. It was then possible to draw two nodal planes through the data. Only two dilatations were recorded and a thrust-type event is clearly indicated. The upper plane (I) is well constrained: the lower one (II) is not. It can take any position between IIA and IIB and still satisfy both the data and the orthogonality condition.

The seismic moment was calculated from the ratio of observed to theoretical spectral amplitudes of the long-period vertical Rayleigh waves and the mean value obtained was $(1.5 \pm 0.4) \times 10^{26}$ dyne-cm. Theoretical spectra were calculated using the method of Saito in a flat continental earth model, with source depth assumed to be 30 km and source time dependence assumed to be that of a step function.

The main shock was relocated (28.51°N, 52.82°E) and the residuals used as station corrections in relocating the aftershocks. This proved to be remarkably successful in restricting these to a fairly narrow band (Fig. III-4) in comparison with the NOS locations, which were spread over an area of 5000 km^2. On the same diagram are shown the observed fault breaks on the surface. The trend of these agrees well with those of the aftershock distribution. There is no indication as to which of the nodal planes is the fault plane. To agree with the fault break/aftershock trend it could be either plane I or plane IIB, in which case the event has no strike-slip component.

The length of the aftershock distribution (85 km) is taken as that of the fault plane and the depth assumed (no depth phases were reported) to be 30 km. This gives the area of the fault plane A as $(85 \times 30)/\cos \delta$ km^2, where δ is the dip of the (unresolved) fault plane which can be either 54° (IIB) or 36° (I). Taking $\mu = 5 \times 10^{11}$ dyne-cm^{-2}, we have, since the seismic moment $M_o = \mu \bar{u} A = 1.5 \times 10^{26}$ dyne-cm (where μ is the shear modulus at the source depth), that the minimum value of mean relative displacement $\bar{u}$ along the fault plane is (12 cos 54°) = 7 cm.

Taking $E_S = 5.4 + 2.8\, m_b$ as a measure of the seismic energy release, we have, from $m_b =$ 6.1 and E, the total energy release $= \bar{\sigma}\,\bar{u}\,A$. Then the apparent average stress, the product of mean stress on the fault plane and the seismic efficiency factor is 10 bars.

R. North[*]

C. OBSERVATIONS OF DEPTH PHASES

The phases pP and sP are of the utmost importance in event location and identification. Depth determination by times of P arrivals is never entirely satisfactory. In particular, for small events, where less than 10 stations may be reporting, the depth estimate is necessarily unreliable, especially for shallow events. Under these circumstances the presence of pP or sP is most useful. In the last SATS,[1] for instance, Landers showed the impact that pP made on identifying an event which could not be ascribed a depth to within 50 kms by P-waves alone.

Unfortunately pP and sP are somewhat wayward phases. I do not have extensive statistics on depth phases, but based on limited experience it appears that frequently these phases are not recorded adequately enough to permit their confident identification. This may be because the phase occurs in a high coda level, but I present here some evidence to show that, at least for one event, pP and sP are absent in the short-period band in a case where the coda level is low and the focal mechanism gives no indication of any unusual circumstances. The event was a Hindu Kush earthquake (m_b about 6.0) of 20 January 1972. The locations from LASA and NORSAR were 36°N, 70°E and 34°N, 73°E, respectively. Neither of the arrays reported a depth phase (Fig. III-5) and the short-period P-waves were fairly simple. It could be argued that the LASA beam shows a signal about 53 sec after P and that this is in fact pP, but by the same token a signal about 20 sec after P could be called pP. In addition, surface waves were very poorly excited. Thus, on the face of it this event needed further investigation, especially as its array locations fell relatively close to the borders of the Soviet Union (Fig. III-6).

Hindsight, in the form of the NOS bulletin, tells us that the event was located at 36.4°N, 70.7°E and was 213 km deep, which explains the lack of surface waves. However, before a network depth determination became available there was no short-period body wave evidence that the event was not at the surface. In Fig. III-7 is a comparison between short-period P at College, Alaska, for this event and an event at 36.3°N, 70.4°E, h = 225 km on 29 January 1968. The clear pP for the latter event demonstrates the marked variability in reflectivity in this region. The problem in this case is not insoluble. Although no station among 40 or 50 WWSSN and array locations examined gave anything approaching a credible short-period pP, analysis of long-period records has revealed evidence for long-period sP, but nothing very conclusive for long-period pP. In Fig. III-8 are 6 long-period records showing P and sP and the limited evidence for pP (at Chiengmai, Thailand). Figure III-9 is a LASA beam showing rather clearly both sP and sPP.

It appears that this event displays an unusual combination of circumstances. The focal mechanism is an overthrust on a fault plane very nearly vertical or horizontal. Long-period pP to stations in the northern hemisphere is rather poorly excited being near a nodal plane. Short-period pP and sP are rendered unrecognizable, either because of strong scattering near the Earth's surface (topography is very marked in this region), or by some defocusing owing to lateral variations of elastic properties near source, or by both. Probably both. The event highlights the necessity to take a very broad view of the source.

D. Davies

---

[*] University of Cambridge.

D. A STOCHASTIC EARTHQUAKE SEQUENCE

Knopoff[7] has set down a stochastic model for earthquake occurrence in which the potential energy of deformation is taken as the appropriate state variable. The concept has recently been tested,[8] with favorable results, against a laboratory device built to model a seismic region. The stochastic model is described by the integrodifferential equation

$$\lambda_2 P + \alpha \, \frac{dP}{dE} = \int_E^{E_{MAX}} T(X, E) \, \lambda_2(X) \, P(X) \, dX \qquad \text{(III-1)}$$

where

> $P(E) \, dE$ is the probability that the system is in a state of deformation with energy between E and $E + dE$,

> $\lambda_2(E) \, dt$ is the probability that an event occurred in the time interval dt if the system is in energy state E,

> $T(X, E) \, dE$ is the conditional probability that, if the system is in the pre-shock state of deformation X and a shock does occur then the final state of deformation lies between E and $E + dE$.

> α is the rate at which deformation energy is added to the system and is taken to be constant,

and

> E_{MAX} is the maximum energy of deformation which the system can sustain.

Equation (III-1) is based on the assumption that the only way an energy state E can be reached is from below through the build-up of deformational energy or from above through the occurrence of an earthquake at some greater energy state. In Eq. (III-1) all the probabilities are taken to be stationary.

The verification of Eq. (III-1) in nature would be based on an earthquake catalog of an autonomous seismic region where the rate of deformational energy increase is known. The latter two conditions may not, in general, be frequently met. Tom Simkin (Smithsonian Institution) and I have recently completed a rather detailed study of an earthquake swarm which occurred during June of 1968 in the Galapagos Islands. We have attributed the source of the swarm to the collapse of the caldera of the island volcano Fernandina. From our seismicity lists we have computed the seismic energy release as a function of time using surface wave magnitudes (M_s) and the formula[9]

$$\log E_s = 11.8 + 1.5 \, M_s \qquad . \qquad \text{(III-2)}$$

Figure III-10 summarizes the seismicity of the Galapagos swarm. The histogram at the top of the figure indicates the number of events that occurred during each day, while the cumulative energy based on Eq. (III-2) is plotted in the lower part of the figure on both logarithmic and linear scales. It is clear from the linear energy vs time diagram that the rate of energy release is nearly constant over about a seven day period. We suggest that gravitational potential energy is supplied to the caldera block by the withdrawal of a supporting magma from below at a constant rate and that this phenomenon is reflected in the constant rate of seismic energy release. If these assertions are correct, then the physical conditions of autonomy and constant rate of deformational energy increase necessary for the verification of Eq. (III-1) are met.

Following Knopoff, we have tested Eq. (III-1) by evaluating the left and right hand sides at twenty equal energy increments from $E = 0$ to $E = E_{MAX}$ over the period 13-19 June 1968. We used a time increment of 1 min. and, from Fig. III-11 have set $\alpha = 0.6 \times 10^{17}$ ergs/min. Throughout this test we take the seismic energy, E_s, to represent the energy of deformation, E, through a seismic efficiency constant. We have set $E_{MAX} = 0.4 \times 10^{20}$ ergs, the seismic energy of the largest earthquake of the sequence. At each minute of the seven day period we have computed the deformational energy of the system, $E(t)$, using

$$E(t) = (\alpha_o + \alpha t) - \int_o^{t-1} E_s \, dt \qquad (III-3)$$

where α_o was set equal to 0.15×10^{20} ergs. Using our list of origin times and surface wave magnitudes for 341 earthquakes during the period and Eqs. (III-1 and -2), the evaluation of both sides of Eq. (III-1) is straightforward.

In Fig. III-11 the values of the right- and left-hand sides of Eq. (III-1) are plotted for the 20 energy increments used. The agreement between the two sets of values is good and Eq. (III-1) is taken as representative of the statistical aspects of the swarm. We have also evaluated Eq. (III-1) over sub-intervals of less than seven days and found that, although Eq. (III-1) is still satisfied, the shape of the probability density functions $P(E)$ and $\lambda_2(E)$ changes. This implies that although the statistics of the swarm are not time stationary they are, over any time interval, related through Eq. (III-1). That the swarm is nonstationary can easily be seen in Fig. III-12 where we show the detail of the first five days of the major portion of the swarm. It is clear from this figure that the swarm is not stationary, the size and frequency of occurrence of earth-quakes changing markedly early on 15 June. The periodicity of the large events during the 13th and 14th has led us to consider elsewhere various deterministic models, including tidal trigger-ing, in discussion of the cause for these earthquakes. Whatever the correct physical source model, it is clear that Knopoff's statistical model applies in this case where we found that the classical frequency-magnitude formula, $\log N = a + bM$, did not.

J. Filson

E. ENERGY-MOMENT RATIOS FROM LONG-PERIOD P WAVES

The analysis of the long-period P waves from a Siberian earthquake, discussed in the last SATS,[1] has been extended in order to consider the complete waveform. First motions and wave-form elongation had previously indicated that the source of this earthquake was a vertical, strike-slip fault, where the source of the rupture propagated to the northwest at an azimuth of 325°. Following Haskell,[10] the far field P-wave displacement (u_α) from a linear fault with unilateral rupture is represented as

$$u_\alpha = R_\alpha(r, \Theta, \varphi) \, M_o T^{-1} \, [G(t) - G(t - T)] \qquad (III-4)$$

In Eq. (III-4), R_α is a geometric term depending on the epicentral distance r and the orientation (Θ, φ) of the fault plane with respect to the recording station. M_o represents the moment, T a characteristic time and $G(t)$ the time variation of the slip across the fault. In Eq. (III-4) the characteristic time T is represented by

$$T = L \, [C^{-1} - \alpha^{-1} \cos(\Theta)] \qquad (III-5)$$

63

where L is the fault length, C the rupture velocity and α the apparent P-wave phase velocity. In the case of vertical strike-slip faulting, Θ is the azimuth to a recording station measured in the horizontal plane from the direction of fault propagation.

Figure III-13 shows how one might gain estimates of source parameters T, M_o and energy E in an idealized case. If $G(t)$ is a step function, then the apparent source duration would be measurable at a given station as the length of ground displacement u_α which varies as $G(t) - G(t-T)$. The integral of u_α should be proportional to the moment M_o at a given azimuth and the integral $\int \dot{u}_\alpha^2$ to the energy in the waveform. Ideally these integrals should vary with time, as shown in Fig. III-13. The product of the ratio E/M_o, the source rigidity, and a constant $K(r, \Theta, \varphi)$ should yield the apparent effective stress acting during the faulting process. Of course we cannot expect an actual seismic source to give rise to the simplified forms of these functions shown in Fig. III-13.

Figure III-14 shows the displacement impulse response $I(t)$ of the long period WWSSN instrument at BKS. $S(t)$ is the trace of the long-period vertical seismometer at BKS [Berkeley] and $u(t)$ is the ground motion gained through the deconvolution of $S(t)$ with $I(t)$. The integral of $u(t)$ with time is shown in the lower left of Fig. III-14. The long term level of this integral, if corrected for radiation and transmission effects, is proportional to M_o. It is pointed out that there is a base line problem in computing the integral of ground displacement. Out of some 30 waveforms to which this technique was applied, only about half showed a clear tendency to level off at some constant long term value.

In Fig. III-15, $H(t)$ represents the response of the instrument to an impulse in ground velocity, $S(t)$ is the same seismogram as in Fig. III-14, and $\dot{u}(t)$, the ground velocity, is gained through the deconvolution of $S(t)$ with $H(t)$. The time variation of the integral $\int \dot{u}(t)^2$ at stations BKS and NOR is shown in the lower left of Fig. III-15. These traces are quite well behaved, usually gaining some constant level within 20 sec of the initial motion. The NOR and BKS integrals are aligned in time with respect to the first detectable P motion. The more rapid rise of the NOR integral is taken to be the effect of source propagation previously discussed. The long term level of these integrals is proportional to the energy in these waveforms.

Although the displacement and energy integrals discussed above are yet to be scaled absolutely, their ratio $\int \dot{u}(t)^2 / \int u(t)$, should be proportional to $\sin(2\Theta)$ in the case of the Siberian earthquake and $\bar{\sigma}$ in general. In order to test the former hypothesis, the long term levels of the velocity/displacement (or energy/moment) integrals measured at 20 sites are plotted as a function of Θ in Fig. III-16. The solid curves in this figure are those of $\sin(2\Theta)$, drawn to approximate the azimuthal variation of the data points. To be consistent with the fault plane solution, these points should show a minimum along the strike of the fault, $325°$. This is not the case. The points are nearly a maximum at that azimuth and are more consistent with a fault plane striking due north (or due west).

In an attempt to resolve this contradiction, the amplitude of the Love wave was measured at 33 WWSSN stations. This phase was well dispersed and exhibited a clear 60-sec component on the east-west horizontal seismometer at many sites. These amplitudes, corrected for spreading and attenuation, are plotted in Fig. III-17 and should vary as $\cos(2\Theta)$ with azimuth. As the solid curves suggest, these amplitudes have a maximum near due north and west, consistent with the integral ratios but not the first motion data. At this stage in the study, it seems that the P-wave integrals and the Love-wave amplitudes are giving a consistent picture of the total faulting process, while the P-wave first motions, in this case, indicate only the orientation of the initial fault breakage.

J. Filson

REFERENCES

1. Seismic Discrimination SATS, Lincoln Laboratory, M.I.T. (30 June 1972), DDC AD-748304.

2. W.J. Lanz and R.J. Sun, Atlas of the Sino-Soviet Bloc to Support Detection of Underground Nuclear Testing. Vol. III. Seismicity, U.S. Geological Survey (1967).

3. T.J. Fitch, "Earthquake Mechanism in the Himalayan, Burmese, Andaman Regions and Continental Tectonics in Central Asia," J. Geophys. Res. 75, 2699-2708 (1970).

4. A.A. Nowroozi, "Focal Mechanism of Earthquakes in Persia, Turkey, West Pakistan, and Afghanistan and Plate Tectonics of the Middle East," Bull. Seismol. Soc. Am. 62, 823-850 (1972).

5. Tectonic Map of Eurasia, A.L. Yanshin, ed., Geological Institute of the Academy of Sciences, USSR, Moscow (1966).

6. J.T. Wilson, "Mao's Almanac: 3,000 Years of Killer Earthquakes," Saturday Review (19 February 1972).

7. L. Knopoff, "A Stochastic Model for the Occurrence of Main-Sequence Earthquakes," Rev. Geophys. Space Phys. 9, 175-188 (1971).

8. L. Knopoff, R. Mitchel and D. Jackson, "A Stochastic Analysis of a Model Earthquake Sequence," Geophys. J.R. Astr. Soc. 29, 255-261 (1972).

9. B. Gutenberg and C.F. Richter, "Magnitude and Energy of Earthquakes," Ann. Geofisica 9, 1-15 (1956).

10. N. Haskell, "Total Energy and Energy Spectral Density of Elastic Wave Radiation from Propagating Faults," Bull. Seismol. Soc. Am. 54, 1811-1842 (1964).
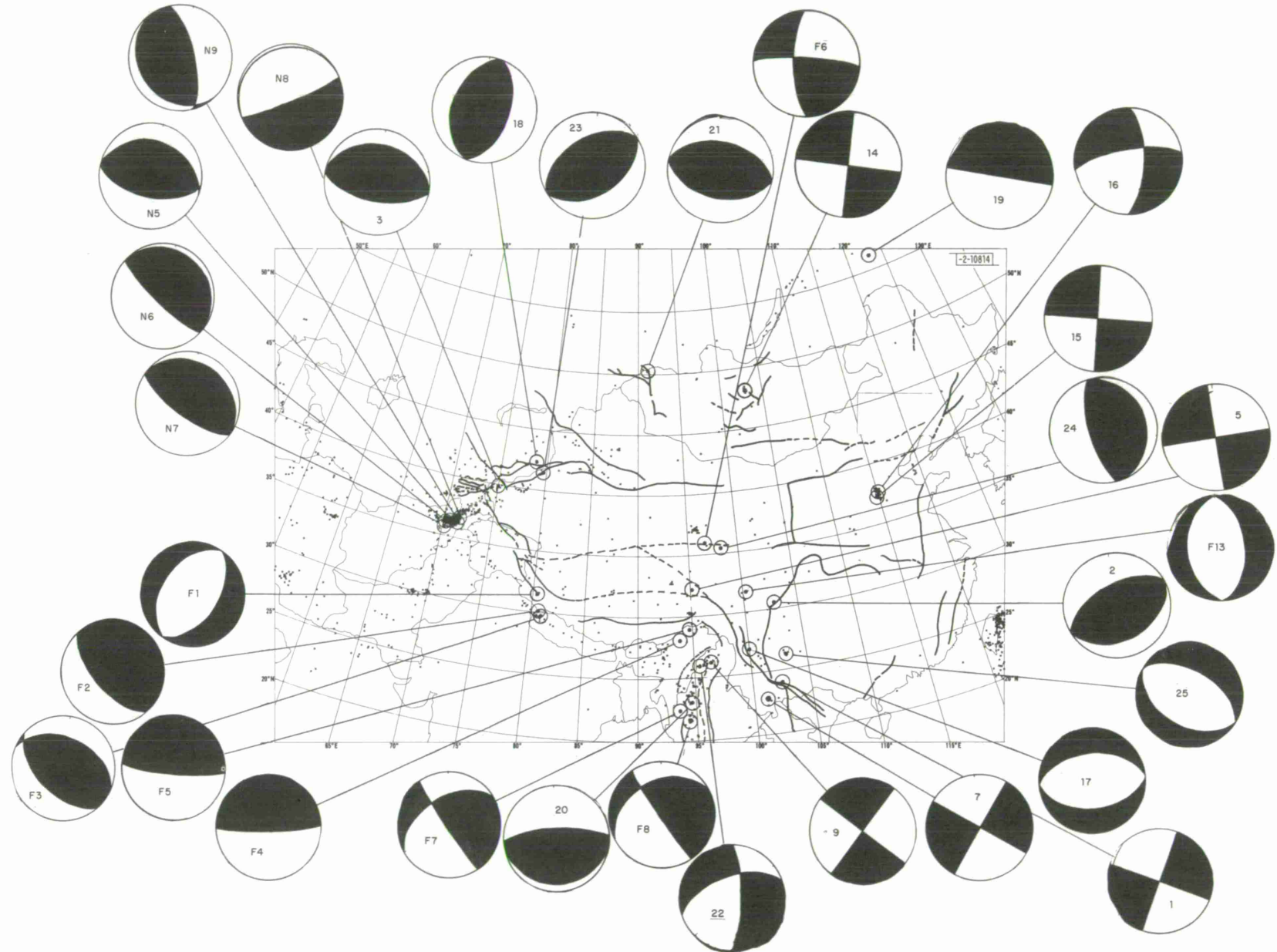
Fig. III-1.   Fault plane solutions of Asia.   F and N refer to solutions of Fitch[3] and Nowroozi.[4]   Base map is a seismicity map published by the National Ocean Survey of the Department of Commerce.   Faults are 'main deep faults' of Yanshin.[5]
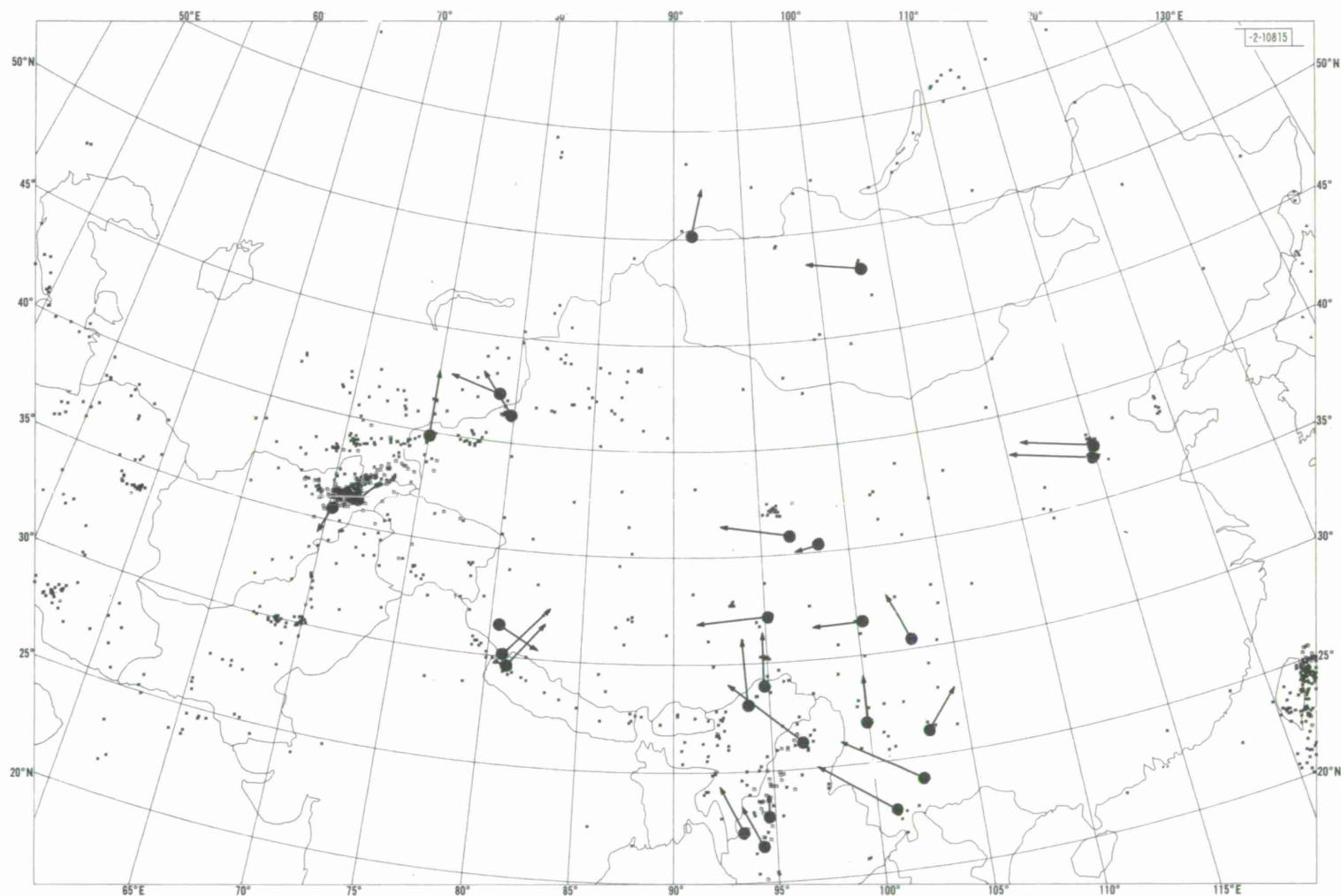
Fig. III-2.   Slip vectors inferred from Fig. III-1.   Base map same as Fig. III-1.
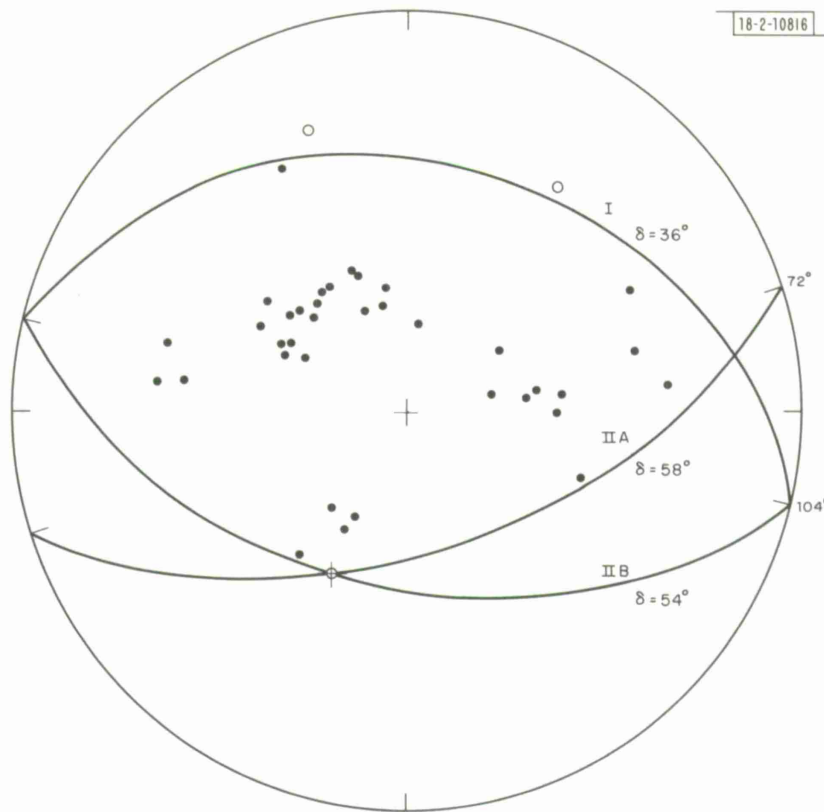
Fig. III-3.   Focal sphere for Iranian thrust event.   Dilatations are open circles, compressions closed circles.
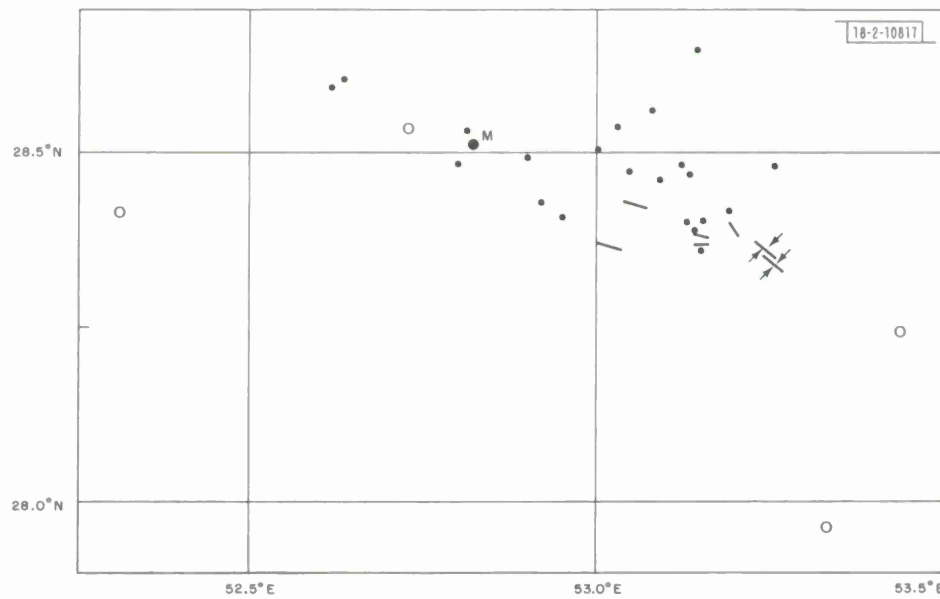
Fig. III-4.   Relocated earthquakes for Iranian sequence.   Surface breaks are also marked.   Open circles represent less reliable locations.   M is the main shock.
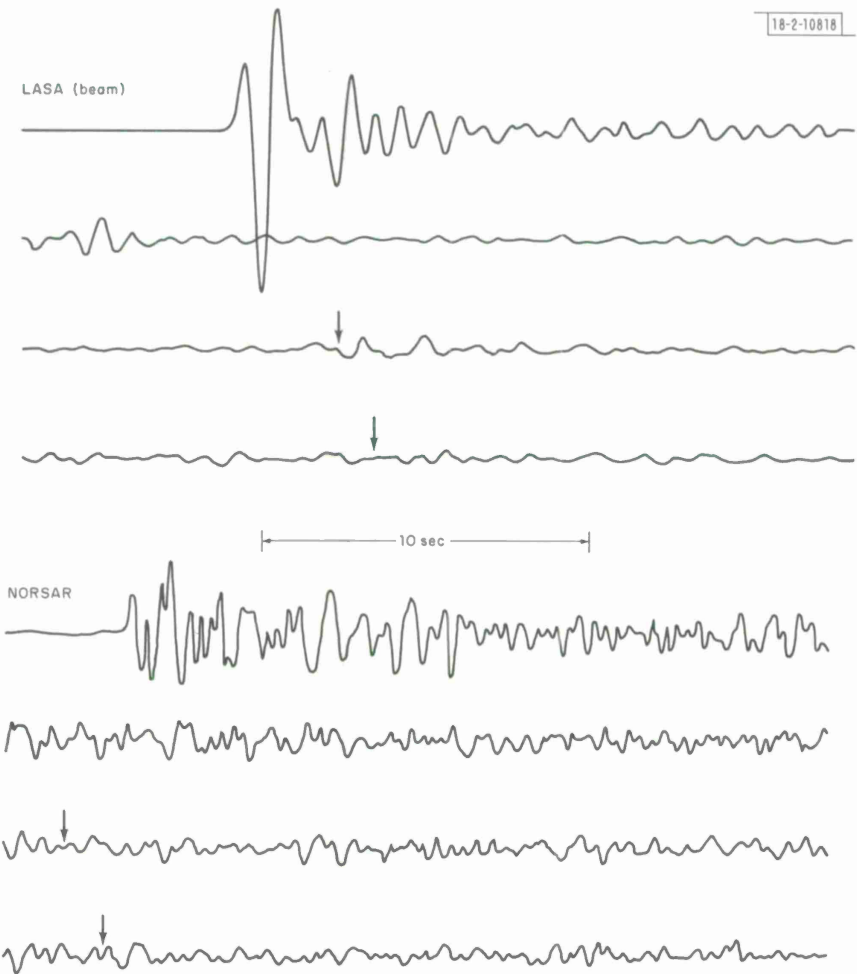
Fig. III-5. Short-period P-waveforms at LASA and NORSAR for the deep Hindu Kush event of 20 January 1972. The expected arrival times for pP and sP are marked. The records should be read like Western printing, left to right, top to bottom.
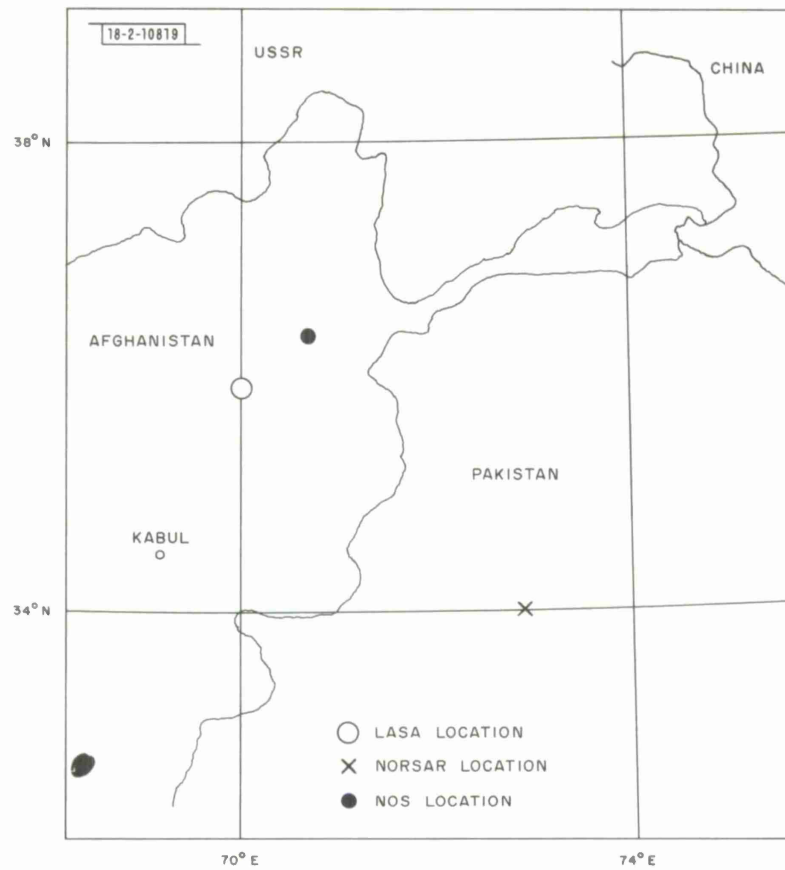
Fig. III-6. Locations of the 20 January 1972 event by LASA, NORSAR and NOS. The array locations are not, of course, claimed to be as accurate as the NOS location.
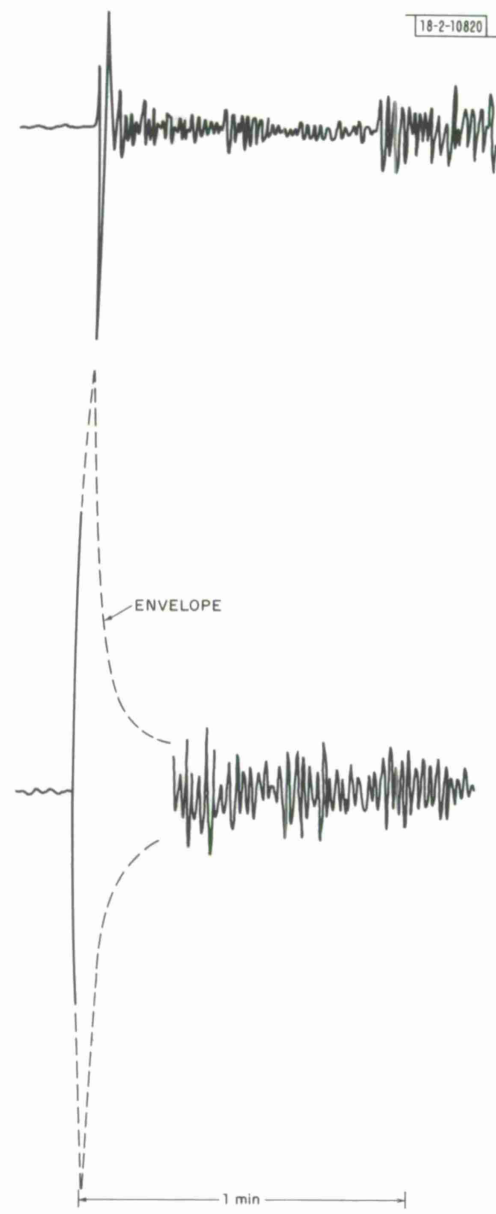
Fig. III-7.   Short-period P at College, Alaska ($\Delta = 75°$) for the events of 29 January 1968 (upper) and 20 January 1972 (lower).
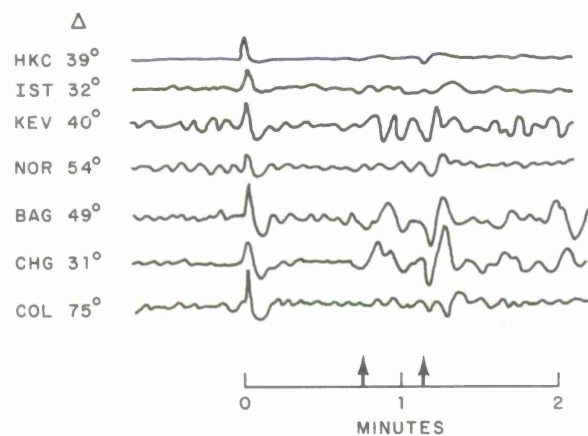
Fig. III-8. Long-period records of the 20 January 1972 event at Hong Kong (HKC), Istanbul (IST), Kevo (KEV), Nord (NOR), Baguio (BAG), Chiengmai (CHG) and College (COL). The expected arrival times (approximate) of pP and sP are marked by arrows.
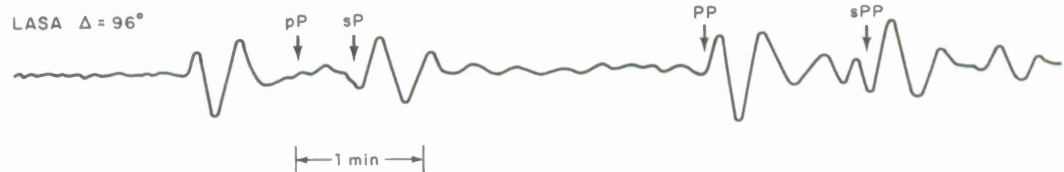
Fig. III-9. LASA long-period beam to the 20 January 1972 event.
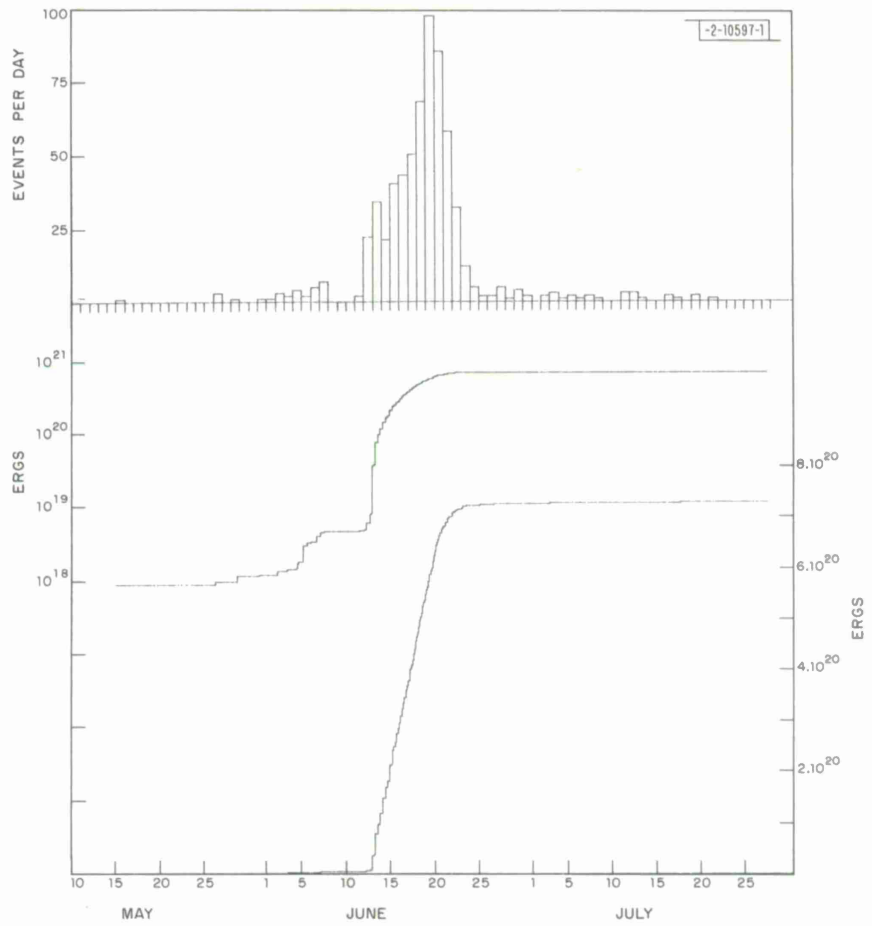
Fig. III-10. Summary of the seismicity of the Galapagos swarm. Histogram at top shows events per day ($M_s \geqslant 3.0$). Middle curve is seismic energy release on a logarithmic scale. Lower line is seismic energy release on a linear scale. Note linearity of energy release between 12 and 20 June.
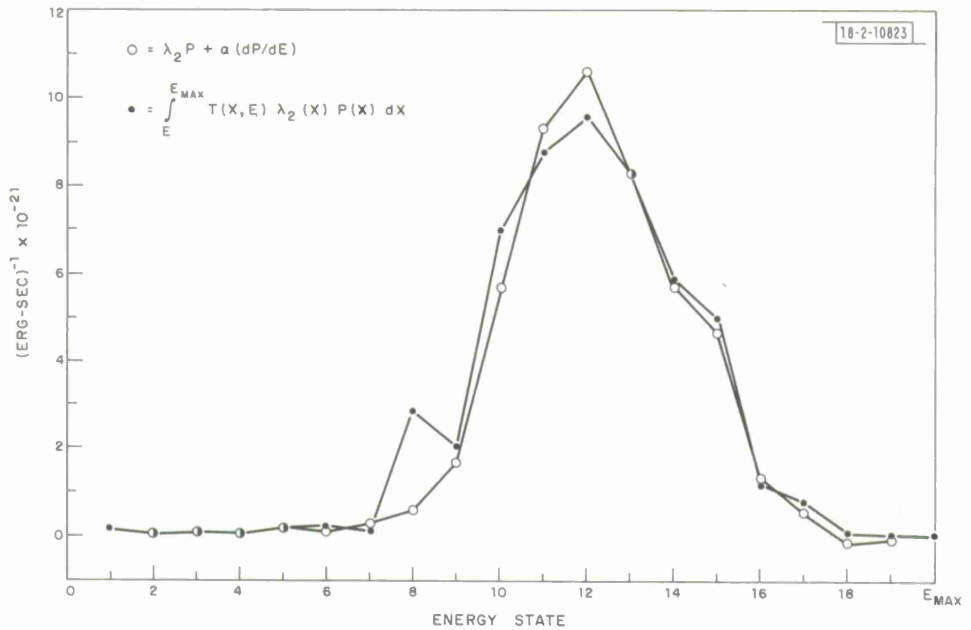
Fig. III-11. Results of numerical evaluation of left-hand side (open circles) and right-hand side (solid circles) of Eq. (III-1) over the period 13 to 19 June.
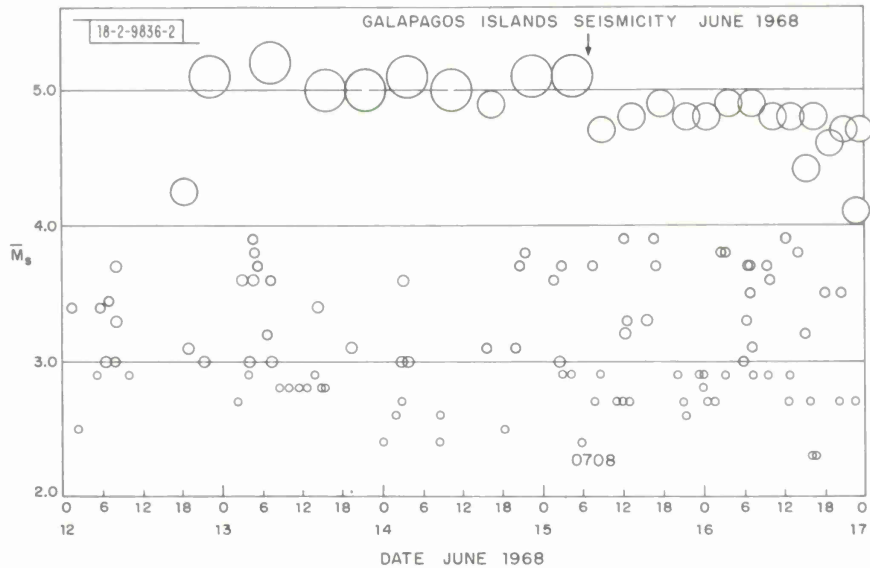

Fig. III-12. Details of seismicity of swarm for period 12 to 17 June. It is obvious from this diagram that statistics of swarm are not stationary.

a. $G(t) - G(t-T)$ =

b. $\int_0^T u_\alpha \, dt$ =

M_o

c. $\int_0^T (\dot{u}_\alpha)^2 \, dt$ =

E

d. $\bar{\sigma}$ = $K\mu \, E \, M_o^{-1}$
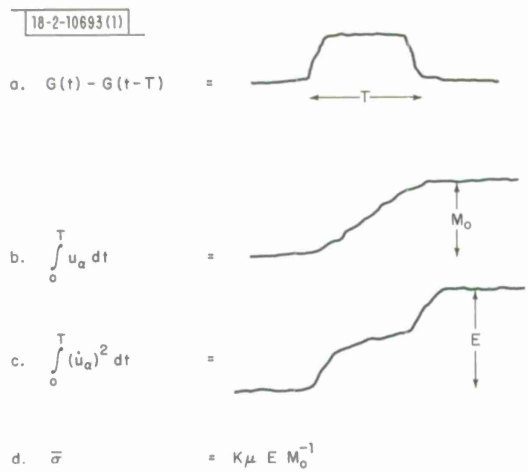
Fig. III-13. Displacement and velocity integrals from an idealized source. (a) $G(t) - G(t-T)$ represents idealized teleseismic ground motion (u_α) from a propagating Heaviside slip; (b) long-term level of integral of this ground motion should be proportional to the seismic moment; (c) long-term level of integral of ground velocity squared should be proportional to energy in the wave form; (d) ratio of these integrals is proportional to apparent effective stress.

$I(t)$

$u(t)$

$0-$

$0-$

20 sec

BKS

$S(t)$

$\int u(t)$

$0-$

$0-$
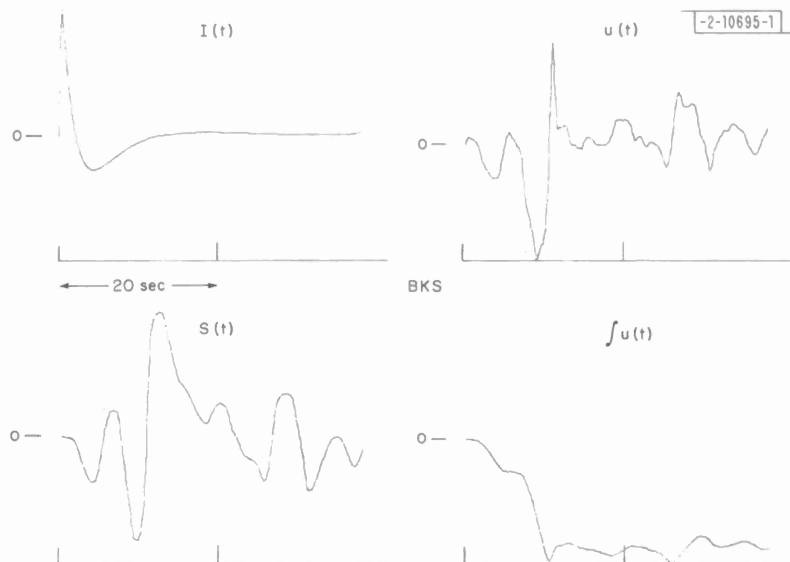
Fig. III-14. Computed displacement integral at BKS. $I(t)$ is displacement impulse response of long-period vertical seismometer; $S(t)$ is P-wave from a Siberian earthquake written by that instrument; $u(t)$ is vertical ground motion gained through deconvolution of $I(t)*u(t) = S(t)$.

75
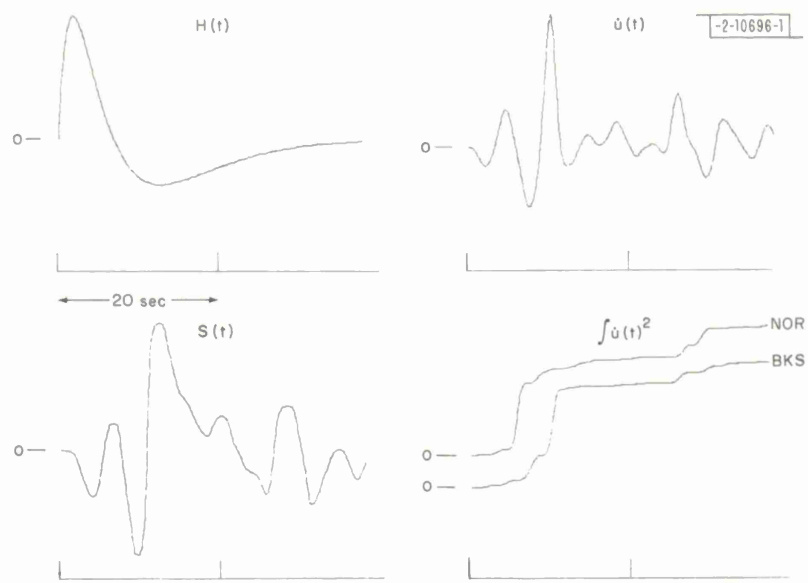
Fig. III-15. Computed velocity integral at BKS. H(t) is velocity impulse response of long-period vertical seismometer; S(t) is same as Fig. III-14; u̇(t) is vertical ground velocity gained through deconvolution H(t)*u(t) = S(t).
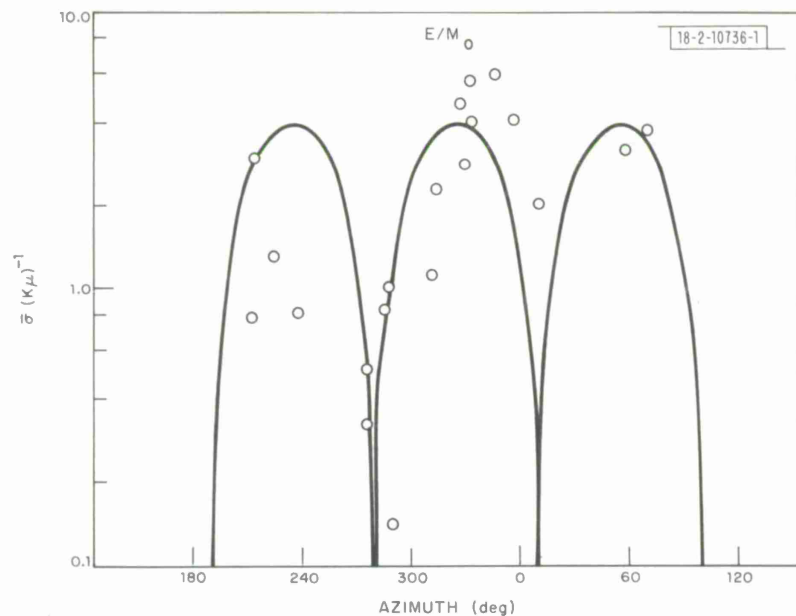
Fig. III-16. Velocity-displacement integral ratios as a function of azimuth. Open dots are measured ratios of velocity to displacement integrals; solid line shows theoretical variation of this ratio with azimuth.

76
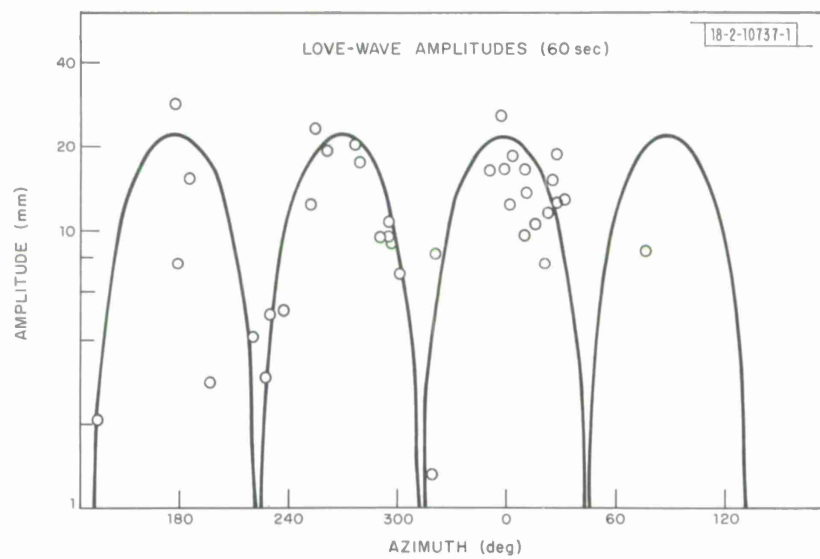
Fig. III-17. Corrected Love-wave amplitudes as a function of azimuth. Open
dots are Love-wave amplitudes corrected for spreading and attenuation. Solid
line shows theoretical variation of these amplitudes with azimuth.
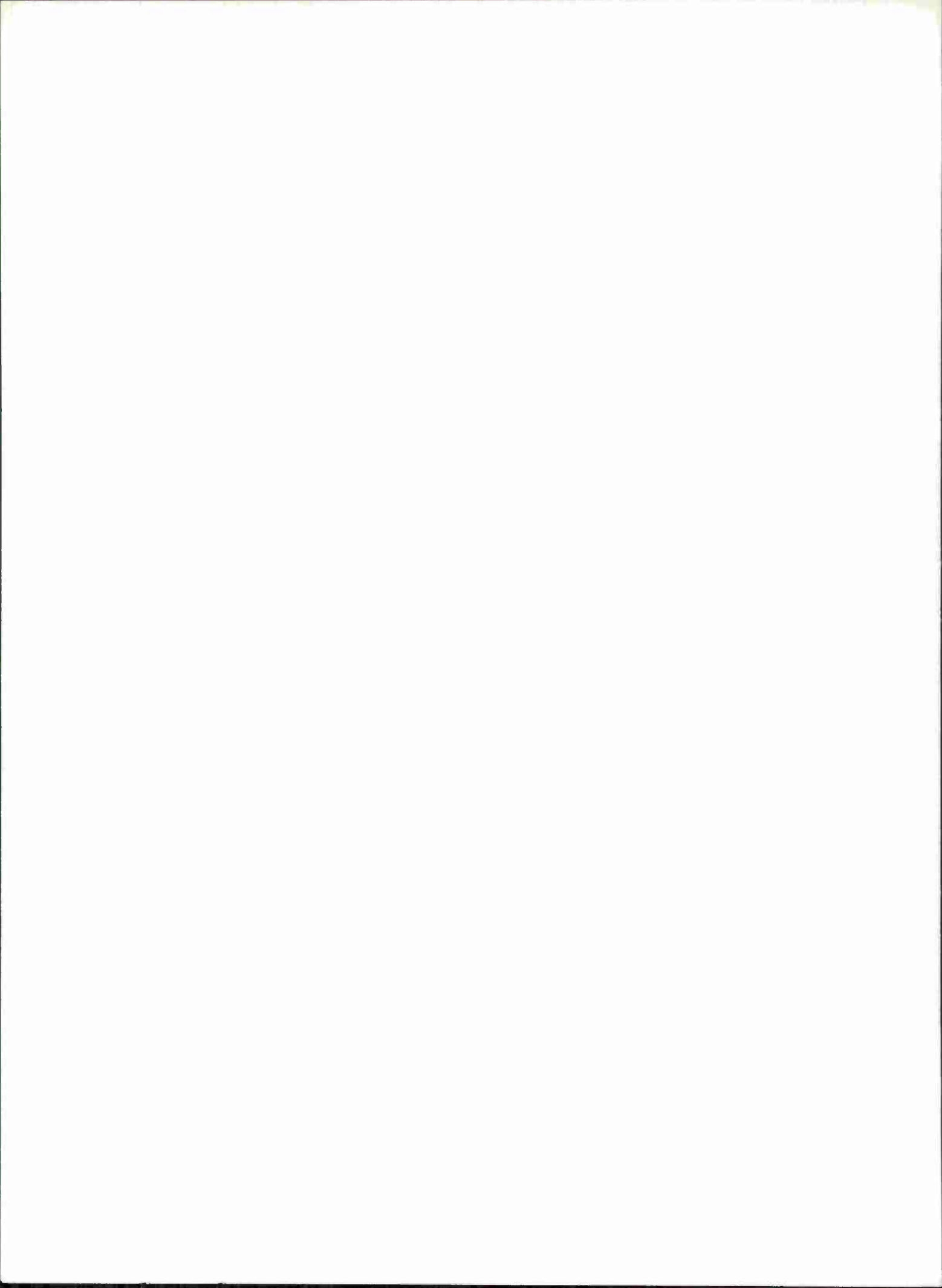
# IV. SIGNALS AND NOISE

A. SUPPRESSION OF LONG-PERIOD NONPROPAGATING NOISE

The work on the prediction and suppression of long-period nonpropagating noise described in the last two SATS[1,2] has now been completed and is more fully described elsewhere.[3] Outlined here are the main conclusions of this study.

Approximately half the noise observed by long-period seismometers at LASA is nonpropagating;[4] that is, it is incoherent over distances greater than a few kilometers. However, because it is often strongly coherent with microbarograph data recorded at the same site at the same time, a large proportion of it can be predicted by convolving the microbarogram with some transfer function. The reduction in noise level using this technique can be as high as 5 dB on the vertical seismometer and higher still on the horizontals. If the source of this noise observed on the vertical seismometer were predominantly buoyancy in the instrument, the same transfer function would be expected to predict the noise observed in the output of the same microbarograph at another time when the coherence between them is again high. Since it does not,[1] one is forced to conclude that the noise is caused by atmospheric deformation of the ground.

Since so much of this noise can be removed merely by subtracting that component which is correlated with the microbarogram recorded at the same site, the deformations must be caused largely by atmospheric pressure disturbances in the near vicinity of the seismometer. Any far-field atmospheric loading effects must be quite insignificant. In describing the loading process, therefore, we would expect that an elastic half-space might be an adequate model for the earth and, since the noise is nonpropagating, negligible error would be incurred by considering the deformation to be static. Inspection of the equations for the displacement due to a two-dimensional sinusoidal pressure distribution on the surface of a half-space shows that the displacement is directly proportional to the product of the amplitude of the pressure distribution and its wavelength. If the pressure distribution were stationary and moving relative to the ground with the wind speed, the wavelength of the noise observed by the seismometer at a given frequency would be directly proportional to the wind speed. One can see why the transfer function which works on one day does not work on another: the wind speeds are different.

A hope was expressed in the last SATS[2] that the deconvolved microbarograph data could be weighted with the deconvolved anemometer data at the same site to provide a time series from which the noise could be predicted with a time-invariant transfer function. After much effort, it was found[3] that this could not be done. The wind speed at any time is generally not the same over space even within the coherence distance of pressure variations. The atmosphere is too turbulent. In other words, the pressure distribution is not stationary in some frame of reference which moves relative to the ground at the mean wind speed.

Despite the turbulence, or rather, because of it, any point on the surface of a half-space is as good as any other for obtaining time-averages of the wind speed and of the fluctuations of microbarometric pressure. Using the half-space model and applying two arbitrarily-chosen filters, $(1 - e^{-\gamma c})$ and $e^{-\eta c}$, to remove any constant background and infinitely high wavenumbers, where c is the wavenumber, an expression has been derived[3] for estimating the noise power which would be observed by the vertical seismometer:

$$E\{u_z^2\} = \frac{\overline{P^2(t)} \cdot \overline{V^2(t)} \cdot T^2}{2\pi\mu^2} [(1 - \nu^2) I_1 + 2\pi z(1 - \nu) I_2 + \pi^2 z^2 I_3] \qquad (IV-1)$$

79

where

$$I_1 = -\log_e \left[\frac{4(2\pi z + \eta) \, (\gamma + 2\pi z + \eta)}{(\gamma + 4\pi z + 2\eta)^2} \right] \quad ,$$

$$I_2 = \frac{\gamma^2}{2(2\pi z + \eta) \, (\gamma + 4\pi z + 2\eta) \, (\gamma + 2\pi z + \eta)} \quad ,$$

$$I_3 = \frac{\gamma^2 [\gamma^2 + 6\gamma(2\pi z + \eta) + 6(2\pi z + \eta)^2]}{4(2\pi z + \eta)^2 \, (\gamma + 4\pi z + 2\eta)^2 \, (\gamma + 2\pi z + \eta)^2}$$

and

$\overline{P^2(t)}$ is the mean-square barometric pressure

$\overline{V^2(t)}$ is the mean-square wind speed

T is the period at which the nonpropagating noise peaks on the vertical seismometer

ν is Poisson's ratio for the half-space

z is the depth into the half-space

μ is the rigidity of the half-space

γ is the longest observable wavelength

η is the shortest observable wavelength.

It is clear that the logarithmic term, I_1, becomes infinite if γ is infinite or if η and z are both zero. In other words, in order to use the half-space model to explain band-limited observations of the driving forces, the pressure disturbances must also be band-limited in wave-number space.

Equation (IV-1) was tested using a sample of data lasting about $2\frac{1}{2}$ hrs beginning at 17h 20m 00s on 23 August 1967 and recorded at A0 at LASA. For these data, η and γ were estimated in the following way. The smallest and largest periods to which the seismometer can respond were chosen to be those at which the sensitivity of the instrument is down a factor of 10 from the peak. These periods are about 9 and 80 sec (see Fig. IV-1). η and γ are then assumed to be equal to these periods multiplied by the lowest and highest wind speeds, 5 and 10 msec^{-1}, recorded during this time. Thus, $\eta = 45$ m and $\gamma = 800$ m. This is consistent with measurements of coherence of atmospheric pressure disturbances made by Herron, et al.[5] From Landers'[6] measurements of P- and S-wave velocities in the sediments of LASA, Poisson's ratio ν is estimated to be about 0.3 and the rigidity μ to be about 3.5×10^{10} dyne cm^{-2}. From the microbarograph and anemometer outputs, it was found that $\overline{P^2(t)} = 62.6$ dyne^2 cm^{-4} and $\overline{V^2(t)} = 37$ m^2 sec^{-2}. From the coherence spectrum of the vertical seismometer and the microbarogram, it is found that T = 40 sec. Inserting all these numbers into the right-hand side of Eq. (IV-1) and setting z = 0, we find $E\{u_z^2\} = 723 \times 10^{-18}$ m^2. From the vertical seismogram, we find that $u_z^2 = 764 \times 10^{-18}$ m^2.

The agreement between the estimated and observed noise is obviously too good to be true. Uncertainties exist in the estimates of ν and μ[6] which may affect the result by a factor of 2. The factors I_1, I_2, and I_3 are somewhat arbitrary in that they are derived from arbitrary assumed filters. It should also be remembered that some of the noise is propagating: Capon[4] showed for this sample of data that the nonpropagating component contributed nearly 10 dB more

80

to the noise in the 20- to 40-sec band than did the propagating noise.   Therefore only about 70×10^{-18} m^2 of the observed noise can be propagating.

It is interesting from a practical viewpoint to find how much improvement could be obtained by burying the seismometer.   Figure IV-2 shows the estimated noise power $E\{u_z^2\}$ plotted as a function of depth z using the data discussed above.   It would seem from this example that the noise power of this particular nonpropagating noise, generated by atmospheric pressure disturbances with wavelengths on the order of 45 to 800 m, could have been reduced by an order of magnitude by burying the seismometer 150 m.

Sorrells, et al.,[7] describe a very careful experiment to measure noise caused by local atmospheric pressure changes.   The two 3-component seismometers, one at a surface site and one buried 183 m in a salt mine, were completely isolated from any measurable buoyancy effects.   During calm periods, the noise spectra of the two vertical instruments are virtually identical.   During a windy period when the rms pressure fluctuation was 12 μbars and the mean wind speed was 7.8 msec^{-1}, the noise level in the surface instrument increased by 10 dB in the 20- to 100-sec band, while that in the mine instrument remained the same.   This noise condition is approximately the same as discussed above, in particular the observable wavelengths of the pressure distribution are about the same — perhaps a little longer.   Figure IV-2 predicts that at 183 m one would expect to get a little over 11 dB decrease in noise level.   The results of Sorrells, et al.,[7] thus add some independent confirmation of the validity of Eq. (IV-1).

There would have been some future in predicting and eliminating this noise had it been possible to obtain a time-invariant transfer function.   Since this appears to be out of the question, due to the turbulence of the fickle wind, there remain two ways of suppressing this kind of noise. One method is to bury the seismometer at a depth of about 150 m, where the reduction in noise level would be about 10 dB.   The other method is to employ an array of seismometers placed no closer together than 1 km.   To achieve the same reduction in noise level as would be obtained with a single buried instrument would require 10 surface instruments.   At LASA, no additional measures need be taken to isolate the long-period instruments from buoyancy effects.

<div align="right">A. Ziolkowski</div>

B.   NOISE AND REGIONAL RAYLEIGH WAVES AT LASA

The question addressed was: does there exist a minimum in the long-period noise spectrum which would provide an optimum band for detecting Rayleigh waves from sources at regional distances? This question would be relevant to the design of the response of instruments to be used in a detection network located within say 20° of a seismic region.   I have attempted to answer this question by comparing the average long-period vertical noise spectrum recorded at LASA with the spectra of Rayleigh waves from explosions at NTS ($\Delta = 12.5°$).

Noise samples of 140-sec length were taken at sites D1 and F4 during each month of the year 1969.   The amplitude spectrum of each noise sample was computed and then an average noise spectrum taken at each of the two sites.   For comparison, the amplitude spectra of the Rayleigh waves from the NTS explosion PIPKIN (m_b = 5.5) were also computed from the long-period vertical recordings at both sites.   Both the signal and noise spectra were computed using exactly the same processing parameters, such as data length, sampling rate and taper length.   The LASA long-period instrument response was removed from all of the spectra in order to give a notion of relative ground motion in the long-period band.

The results of this analysis are shown in Figs. IV-3 and -4 (sites F4 and D1, respectively). Although some individual noise samples were bimodal with peaks at about 8 and 15 sec this, apparently, is not a significant, stationary condition at these sites on average. The average noise sample at site D1 shows a slight dip at 0.08 Hz (12 sec), but in general the noise field at both sites increases monotonically, or with slightly less than the square of the frequency between 0.04 and 0.15 Hz. The signal spectra at both sites are quite similar at longer periods, increasing as the first power of frequency in the band 0.02 to 0.1 Hz. At frequencies higher than 0.1 Hz, the shapes of the spectra vary significantly. The peak signal frequency at F4 is about 0.9 Hz, while at D1 it appears at 1.1 Hz.

The fact that the peak signal frequency at one site occurs at a dip in the average noise field at another site is not discounted, indeed on certain days under specific noise conditions it may be quite important. On average, however, the advantages of shaping the instrument recording response of a regional detection network expecting an inverse relation between signal and noise near a period of 12 sec, do not appear great.

J. Filson

REFERENCES

1. Seismic Discrimination SATS, Lincoln Laboratory, M.I.T. (31 December 1971), DDC AD-737092.

2. Seismic Discrimination SATS, Lincoln Laboratory, M.I.T. (30 June 1972), DDC AD-748304.

3. A. M. Ziolkowski, "Prediction and Suppression of Long Period Non-propagating Seismic Noise," Bull. Seismol. Soc. Am. (in press).

4. J. Capon, "Investigation of Long-Period Noise at the Large Aperture Seismic Array," J. Geophys. Res. 74, 3182-3194 (1969).

5. T. J. Herron, I. Tolstoy and D. W. Kraft, "Atmospheric Pressure Background Fluctuations in the Mesoscale Range," J. Geophys. Res. 74, 1321-1324 (1969).

6. T. E. Landers (Paper in preparation).

7. G. G. Sorrells, J. A. McDonald, Z. A. Der and E. Herrin, "Earth Motion Caused by Local Atmospheric Pressure Changes," Geophys. J. R. Astr. Soc. 26, 83-98 (1971).

AMPLITUDE (mV/μm of earth motion)

3-60-7092(4)

10^3

10^2

10

1.0

10^{-1}

10^{-3} 10^{-2} 10^{-1} 1.0

FREQUENCY (Hz)
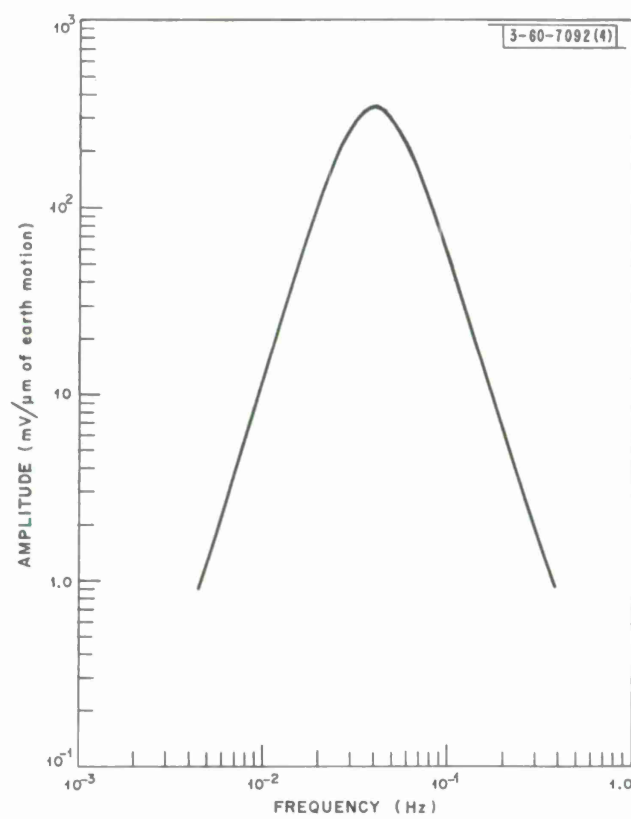
Fig. IV-1.   Long-period system transfer function.
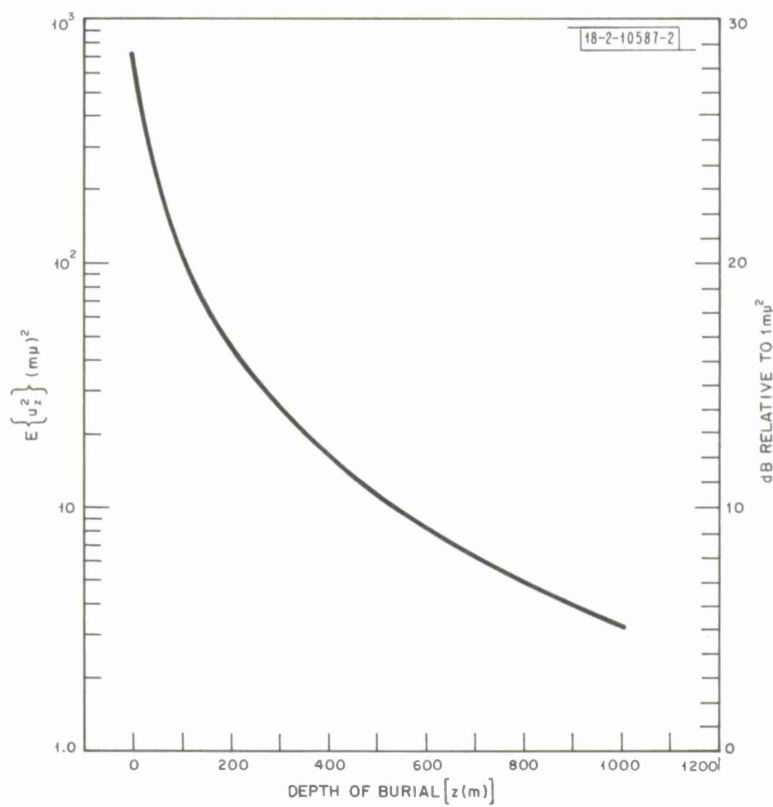
Fig. IV-2. $E\{u_z^2\}$, calculated from Eq. (IV-1), as a function of z using the following data: $\overline{P^2(t)}$ = 62.6 dyne^2 cm^{-4}; $\overline{V^2(t)}$ = 37 m^2 sec^{-2}; T = 40 sec; μ = 3.5 × 10^{10} dyne cm^{-2}; ν = 0.3; η = 45 m; γ = 800 m.
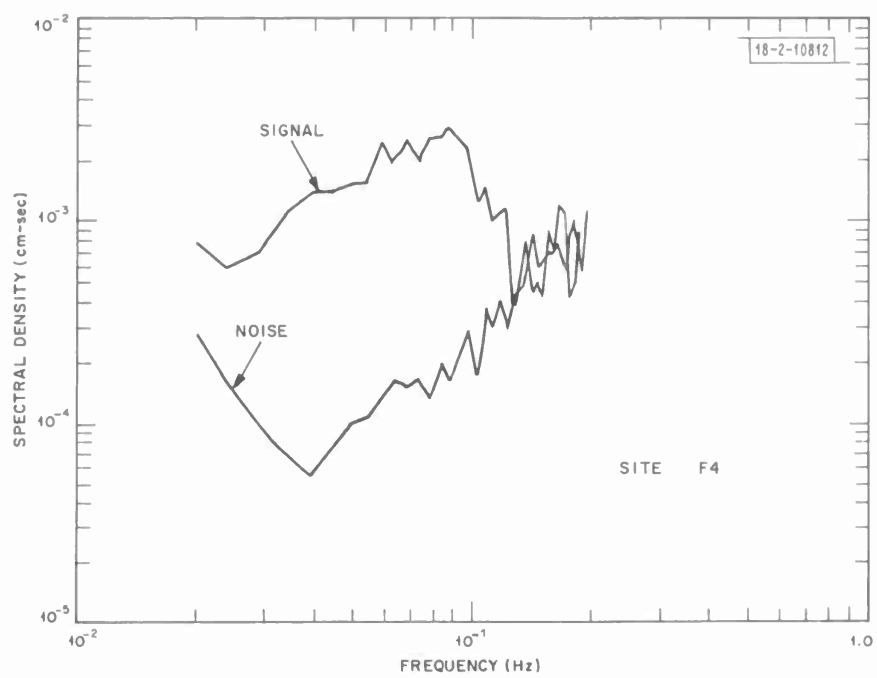
Fig. IV-3. Signal and average noise spectra based on vertical, long-period motion at LASA site F4.
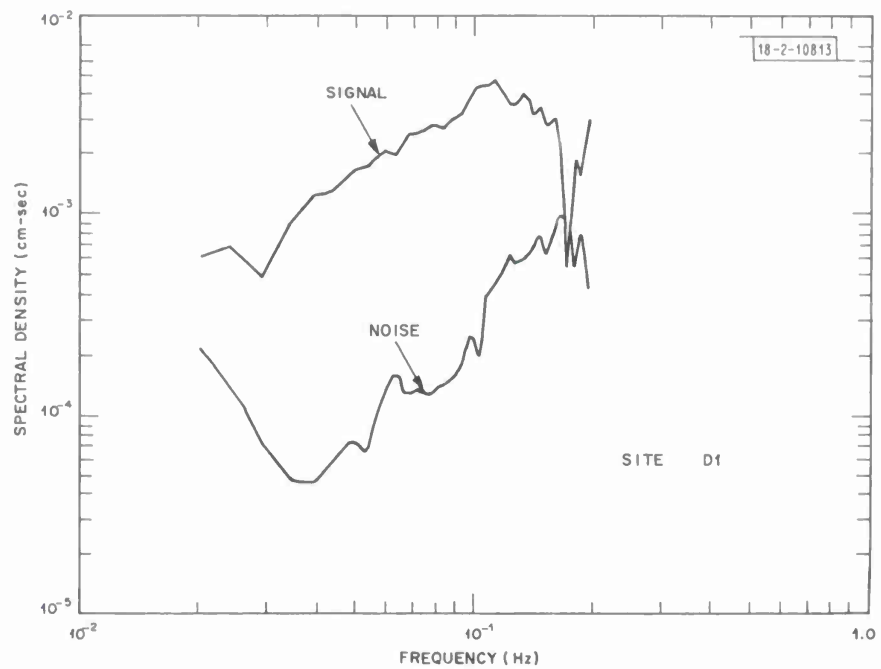
Fig. IV-4. Signal and average noise spectra based on vertical, long-period motion at LASA site D1.
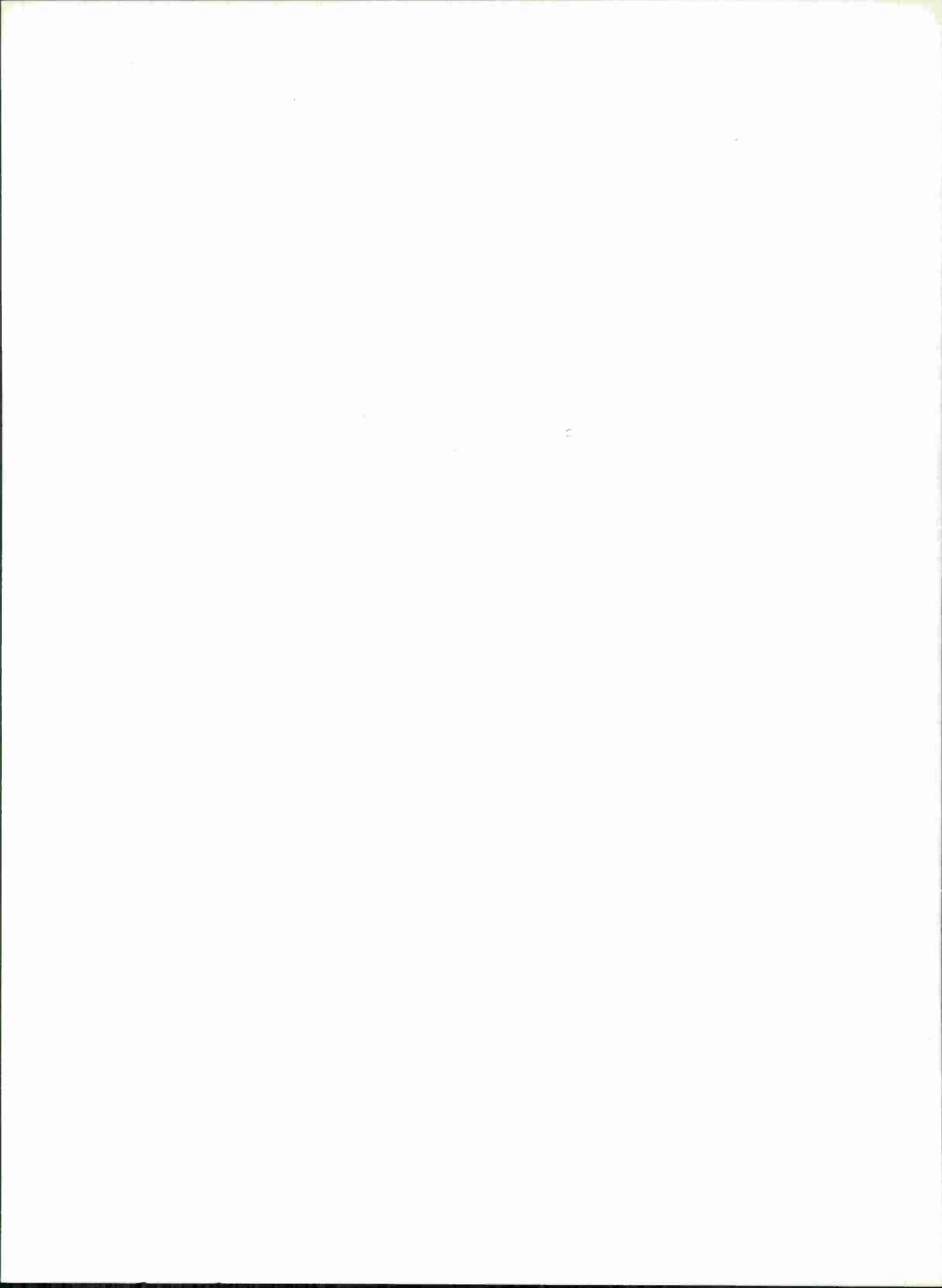
V. DATA HANDLING

A. INTERNATIONAL SEISMIC MONTH PROGRESS

Work has continued on the International Seismic Month[*] during the past six months. The 1152 events currently on the bulletin have been relocated using data supplied by participants and revised epicenter lists distributed. Participants have also been supplied with predicted body- and surface-wave arrival times at stations of particular interest to them. All the lists and basic data for these 1152 events, including all arrival times used to verify each event, have been combined and entered into the DADS system (see Sec. V-B). Future editing, addition of new data, calculation of new derived parameters, and listing of results should be greatly facilitated by this.

Of the 1152 events, 312 require further verification to be certain that they include no bogus events. These have been merged with an additional 2000 potential events suggested by the LASA and NORSAR detection logs. To obtain the 2000 detection log events, some automatic sifting of the basic logs was done to reduce them to about 3800 entries from each array. Then all entries apparently associated with one of our 840 verified events were removed. Also removed were obvious multiple detections and detections with insufficient signal-to-noise ratio. A serious attempt is now in progress to verify as many as possible of the more than 2000 entries on this merged list.

A large body of data has been assembled and more will be obtained to try to enlarge the number of verified events. All reports made to NOS have been obtained and sifted to remove reports associated with verified events and to remove entries from stations which reported fewer than fifty arrivals during the month. The current residual in this list is about 12,000 arrivals. Similar lists of several thousand as yet unassociated arrivals have been compiled from lists supplied by Canadian, Swedish and British colleagues. Also included are unassociated arrivals at selected WWSSN stations obtained by picking arrivals using film records rather than relying upon lists supplied to NOS.

The work of compiling, integrating, and organizing these lists of unverified detection log entries and arrival times is essentially completed.

Special digitizing and processing software have been written for FM analog tapes supplied to us by the United Kingdom Atomic Energy Authority. The objective is to do filtering and beam-forming of UK array data to aid in event verification. If possible and profitable, all available Warramunga, Australia data will be processed with these programs. Data from Gauribidanur, India may also be processed, if available. Other special software has been written to process event tapes from LASA and NORSAR. All beams and subarray beams are made available for visual examination with and without filtering. These are examined selectively as questions arise about specific events or detections.

<div align="right">R. T. Lacoss
R. E. Needham
R. M. Sheppard</div>

B. DATA ANALYSIS AND DISPLAY SYSTEM (DADS)

Development of a new interactive software system to display, edit, plot and otherwise ma-nipulate tabular data is well advanced. Current applications, or applications under development,

---

[*] Seismic Discrimination SATS, Lincoln Laboratory, M.I.T. (30 June 1972), DDC AD-748304.

include management of ISM data and of our entire digital tape library catalog. It is also being used to help develop NORSAR station corrections for our computer system.

The system is designed to deal with data which can be arranged in a matrix with N rows and M columns. Size limitations are $NM \leqslant 400,000$, $N \leqslant 8,000$, and $M \leqslant 500$. The data are stored on a magnetic tape and transferred to a drum at the start of each session with the data. All changes, additions or deletions are done on the drum, and the modified data base is stored on tape at the end of the session.

Each column of the matrix is assigned a name by the user. For example "DATE," "TIME," "LAT," "LONG," and "MB" could refer to columns which contain date, origin time, latitude, longitude and m_b values for seismic events. Each row of the matrix could represent a distinct event, in such a case, and entries in each column could delineate some specific seismic parameter. Parameters can be dates, times, integers, floating point or alphanumeric. The user deals with parameter columns by their names. The user can operate with all columns of the matrix or, by listing names, select any subset of columns to be actively manipulated and displayed during a session with the data.

Some columns of the matrix are denoted selectors and serve a special purpose. Specifically, a selector defines a subset of the rows of the matrix by taking on a special value (+1) only for rows to be included in the subset. For example, a selector might identify all events in a list which have m_b values above 6.0. Listing, display and editing can all be done subject to a selector, so that extraneous rows do not obscure the process. Selectors can currently be constructed row by row manually, or by specifying rows to include via card inputs. Fortran subroutines now exist to allow users to contruct selectors by operating on other parameters and a general search routine will be added shortly to expedite this.

Figure V-1 shows the hierarchy of data matrices in the DADS system. A large matrix of N rows and M columns is stored on our drum. An active submatrix is defined by a list of parameter names and a selector. A display submatrix of the active submatrix is normally visible on a CRT display. Finally, one element of the display submatrix may be singled out and put into a small box. The box can be moved and the data in the box can be edited at will from a teletype. The location of the display submatrix within the active submatrix can be moved by teletype commands or via analog knobs which move the display window up, down, left and right.

Figure V-2 is a photograph of the system in use. In the figure, the basic data display program, which is the heart of the system, is being used. In general, all other programs are called from the display mode via teletype commands and they return to the display mode upon completion. Currently the user can call general programs to:

(1) Create space for new rows or columns and assign names to the columns.

(2) Enter data from cards into any active submatrix to allow batch updates or additions to the data base.

(3) Specify a set of columns to define an active submatrix by entering the list of names from cards.

(4) Define a subset of rows via a selector by entering a list from cards.

(5) Print any active submatrix on a line printer in a standard system format.

(6) Output any active submatrix to tape, or line printer, or teletype in a format specified by the user.

(7) Merge two-ordered list into a single-ordered list by switching rows in the data matrix.

(8) Generate a selector which defines a set of rows as the union of other subsets.

(9) Delete rows or columns from the data matrix.

In addition to general data management routines, several seismic routines have been incorporated into the system. These are:

(1) /ATVEL to generate a matrix column which gives event arrival times at a fixed station.

(2) /ARRIV to obtain body wave arrival times.

(3) /DELAZ to calculate distance and azimuth to a station.

(4) /MB to calculate body wave magnitudes from amplitude, distance and period columns.

L. J. Turek
A. A. Sholl
R. T. Lacoss

PARAMETER AND SELECTOR NAMES (<500)

A B C D E F G H I J K L M N O P Q R S T U V W X Y Z   ALL S1 S2 S3 S4 S5
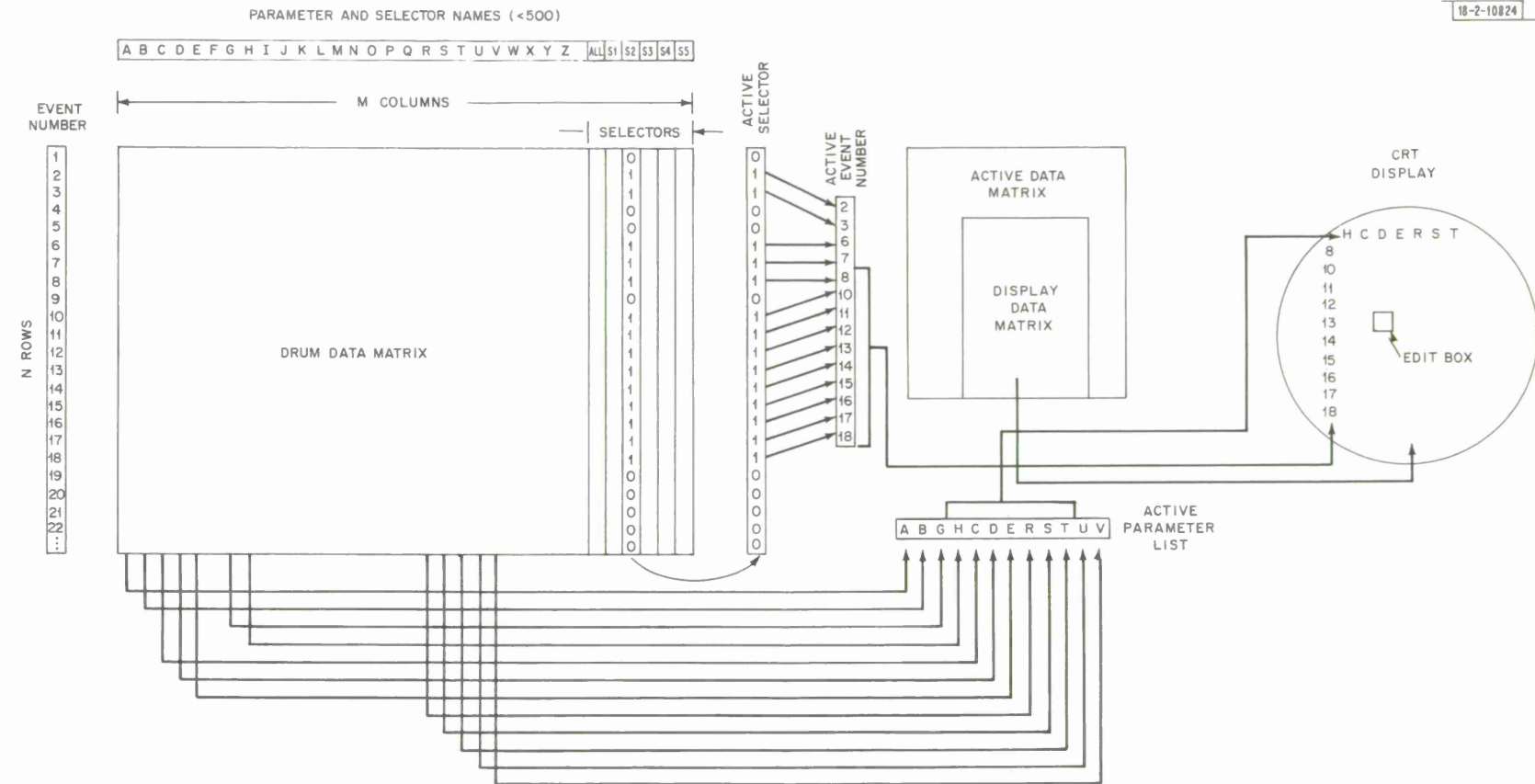
Fig. V-1.   Data matrix structure of Lincoln DADS.

90

Fig. V-2.   DADS in use.
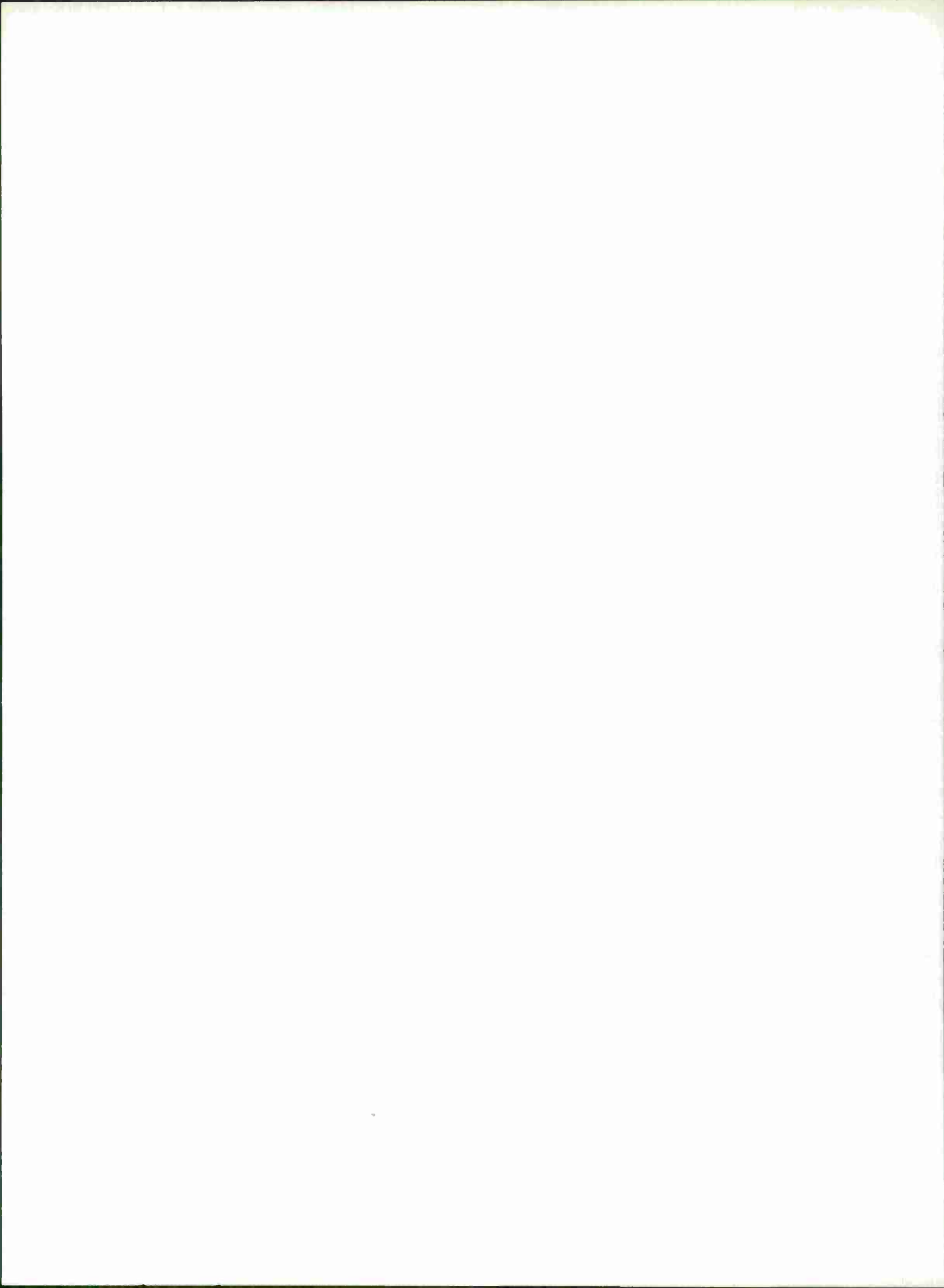
VI. GENERAL SEISMOLOGY

A. OBSERVATIONS OF PcP AND P PHASES AT LASA AT DISTANCES FROM 26° TO 40°

Steered beams of short-period P and PcP phases at LASA are being studied to determine the nature of the core-mantle boundary of the Earth.   In spite of the accumulation of vast amounts of short-period data at single, isolated stations, the large scatter of PcP relative to P amplitudes prevents a clear look at the core-mantle boundary.

A controversial model of the core-mantle boundary has been suggested by Buchbinder.[1] He reported cases of reversed polarity of PcP phases relative to P at single stations for epicentral distances less than 32°, where PcP passed through a minimum.   Based on these observations, Buchbinder suggested a new model having a core-to-mantle density ratio of ~1.0.

Here we report our observations of beamed LASA data for events between 26° and 40°, and compare them to theoretical predictions based on two core-mantle models, one given by Bullen and Haddon,[2] the other by Buchbinder.[1]

The results of the analysis of forty-five events recorded digitally from short-period, vertical component seismographs at LASA are reported.   Only those events with clean P and PcP arrivals, and having nearly equal periods were selected for study.   The purpose of this was to eliminate those events with clearly unequal transmission effects or radiation patterns along the P and PcP takeoff directions.

For each event, steered beams across the entire LASA were formed for both P and PcP phases.   The peak-to-trough amplitudes divided by period (A/T) were calculated for each beam. By measuring these parameters on the beams, the local amplitude variations[3] caused by near surface structure below LASA are minimized.

Figure VI-1 shows the P and PcP phases on the beams for 4 typical events.   The similarity of P and PcP phases is quite marked, indicating that the mantle-core boundary is very sharp where sampled by our data.   P and PcP beams for a selection of events were scaled to NOS magnitude 6.0 by multiplying each amplitude by $10^{\Delta m_b}$, where Δm_b equals 6.0 minus the NOS magnitude of the event.   Figure VI-2 is a plot of the normalized P amplitudes (A/T) in mμ/sec as a function of epicentral distances.   In this figure and all others, triangles identify events from the north, and circles, those from the south of LASA.   Assuming a spherical radiation pattern at the source, theoretical P and PcF amplitude curves were calculated for earth model CIT208 of Johnson.[4]   The amplitudes were smoothed and corrected for attenuation at 1.0 sec in the mantle using the short-period Q model of Archambeau, Flinn and Lambert[5] and for reflection at the free surface.   The P amplitude curve normalized to give A/T values for NOS magnitude 6.0, is shown as a solid line in Fig. VI-2.   The observed P amplitudes show large scatter, and generally are larger than the theoretical P amplitudes.   Lacoss[6] observed this effect for a large population of events recorded at LASA.

Figure VI-3 shows the observed, as well as theoretical PcP amplitudes (A/T) normalized by the same scale factors used for the P amplitudes.   Curve 1 is the PcP amplitude (A/T) corrected for geometric spreading and mantle attenuation at 1.0-sec period, but with a reflection coefficient of 1.0 at the core-mantle boundary.   The effect of two core-mantle boundary models is shown by curves B1 and BK.   The parameters for these models are listed in Table VI-1. Curve B1 is the PcP amplitude predicted by model B1 of Bullen and Haddon.[2] This model, with minor modifications, has been utilized in many core studies as a standard model.   Curve BK is

TABLE VI-1
CORE-MANTLE MODELS

Model		P Velocity (km/sec)	S Velocity (km/sec)	Core-to-Mantle Density Ratio
BK-Buchbinder (1968)	mantle	13.64	7.29	1
	core	7.51	0.00	
B1-Bullen and Haddon (1967)	mantle	13.64	7.30	1.74
	core	8.13	0.00	
BH1-Modified B1	mantle	13.64	7.80	1.94
	core	8.63	0.00	
BH2-Modified B1	mantle	13.64	8.30	2.14
	core	9.13	0.00	

the amplitude predicted by the core-mantle boundary of Buchbinder.[1] The negative sign on curve BK for $\Delta \leqslant 32°$ indicates a negative reflection coefficient at the core-mantle boundary.

The observed data in Fig. VI-3 are widely scattered and are above curve B1, but the trend clearly favors model B1 over model BK. The slight minimum around $\Delta = 36.5°$ cannot be considered reliable in view of the observed scatter in the data. We neither observe any minimum around $\Delta = 32°$, nor the change in polarity below 32°, as predicted by Buchbinder.

In Fig. VI-4, the observed and theoretical PcP/P ratios are shown. The questionable minimum at ∼36° cannot correspond to a zero reflection coefficient at the core-mantle boundary, because the data on either side of 36° have the same polarity. Except for the five indicated events, the data show no change of polarity or amplitude trend with distance from 26° to 40°. A similar conclusion was reached by Bufe[7] in a study of PcP phases from explosions recorded at WWSSN stations.

There are two ways to obtain theoretical curves for PcP/P ratios which are slightly higher than curve B1. One is to modify the Bullen-Haddon model to obtain a higher reflection coefficient at the core-mantle boundary. Two examples, BH1 and BH2, are shown. These models have the parameters given in Table VI-1. Any small increase in mantle shear velocity, core density, or core compressional velocity, will produce an increase in the core-mantle reflection response. Curves BH1 and BH2 show the effect of increasing all three of these parameters simultaneously. Another way to raise the PcP/P ratio is to increase the attenuation of P relative to PcP. The Q model of Archambeau, et al.,[4] used for the theoretical curves, is based on short-period P data from explosions, and is much less attenuative than models based on long-period data. Between 25° and 40° distance, the theoretical curve B1 can be scaled up by a factor of 2.0 by using more attenuative earth models such as those suggested by Kanamori[8] and Ibrahim[9] in their PcP studies.

In Fig. VI-5, the PcP/P ratios are plotted against NOS depth of focus. The wide scatter of data above 100 km probably reflects the complexity of shallow events, as well as uncertainties in source depth and attenuation. Below 100 km, the data scatter appears to be less, but this is deceptive because the density of points is also less.

In conclusion, our observations of PcP/P amplitude ratios at LASA between $\Delta = 26°$ to 40° agree with theoretical ratios calculated using the B1 core-mantle boundary of Bullen and Haddon,[2]

94

and a Q structure more attenuative than the short-period Q model of Archambeau, et al.[5] The wide scatter of amplitudes on the beamed P and PcP phases prohibits the precise determination of the core-mantle boundary parameters.

C. W. Frasier
D. K. Chowdhury*

B. OBSERVATION OF FREE OSCILLATIONS OF THE EARTH

The excitation criterion[10] for identification of spectral peaks of normal modes of the earth enables us to measure the eigenperiods for modes which could not be identified using former techniques.   Figure VI-6 shows the result of using this technique to identify the $_5S_{39}$ mode, excited by the Colombian deep shock of 31 July 1970.

An exhaustive analysis of the data available for this shock has been undertaken and approximately 100 new modes have been identified.   The standard deviation of the eigenperiods measured for the $_0S_n$ modes is approximately the same as the standard error of the mean found for the Alaskan earthquake of 28 March 1964, using a comparable number of stations[11] (Fig. VI-7). Derr's eigenperiods[12] are used as a reference in Fig. VI-7.

In the case of the $_0S_n$ modes, it was found that the eigenperiods are systematically smaller for the Colombian earthquake than those measured for the Alaskan event.   The difference is, in general, smaller than 0.1 percent.   It is within the standard deviation of the measurements at individual stations, but larger than the standard error of the mean (s.e.m.).   A preliminary conclusion of this result is that the lateral heterogeneities of the earth are such that for a given epicenter and the actual distribution of observing stations (the WWSSN) the average eigenperiod over all the stations depends on the epicenter location, and it may be different from the degenerate eigenfrequency of an ideal laterally homogeneous earth by an amount larger than the s.e.m. For the $_0T_n$ modes, the difference is about 3 times larger than for $_0S_n$ modes, but in this case the eigenperiods for the Colombian shock are systematically larger than those found for the Alaskan shock (Fig. VI-8).

Those results clearly imply that it will be necessary to measure eigenperiods of free oscillations excited by earthquakes in different regions of the world in order to estimate the degenerate eigenfrequency of the ideal laterally homogeneous earth, and in order to study the spatial distribution of the lateral heterogeneities.

J. Mendiguren

REFERENCES

1. G. G. R. Buchbinder, "Properties of the Core-Mantle Boundary and Observations of PcP," J. Geophys. Res. 73, 5901-5923 (1968).

2. K. E. Bullen and R. A. W. Haddon, "Earth Models Based on Compressibility Theory," Phys. Earth Planet. Interiors 1, 1-13 (1967).

3. C. W. Frasier, "Amplitudes of P and PcP Phases at LASA (Abstract)," EOS Trans., AGU 53, 600 (1972).

4. L. R. Johnson, "Array Measurements of P Velocities in the Lower Mantle," Bull. Seismol. Soc. Am. 59, 973-1008 (1969).

5. C. B. Archambeau, E. A. Flinn and D. G. Lambert, "Fine Structure of the Upper Mantle," J. Geophys. Res. 74, 5825-5865 (1969).

6. R. T. Lacoss, "A Large-Population LASA Discrimination Experiment," Technical Note 1969-24, Lincoln Laboratory, M.I.T. (8 April 1969), DDC AD-687478.

7. C. G. Bufe and D. S. Carder, "Nature of the Core-Mantle Interface from Surface-Focus PcP Observations (Abstract)," EOS Trans., AGU 53, 600, 1972.

8. H. Kanamori, "Spectrum of P and PcP in Relation to the Mantle-Core Boundary and Attenuation in the Mantle," J. Geophys. Res. 72, 559-571 (1967).

9. A. K. Ibrahim, "The Amplitude Ratio PcP/P and the Core-Mantle Boundary," Pure Appl. Geophys. 91, 114-133 (1971).

10. J. Mendiguren, "Source Mechanism of a Deep Earthquake from Analysis of Worldwide Observations of Free Oscillations," Ph.D. Thesis, Dept. of Earth and Planetary Sciences, M.I.T. (August 1972).

11. A. Dziewonski and F. Gilbert, "Observation of Normal Modes from 84 Recordings of the Alaskan Earthquake of 1964 March 28," Geophys. J. R. Astr. Soc. 27, 393-413 (1972).

12. J. Derr, "Free Oscillations Observations Through 1968," Bull. Seismol. Soc. Am. 59, 2079-2099 (1969).
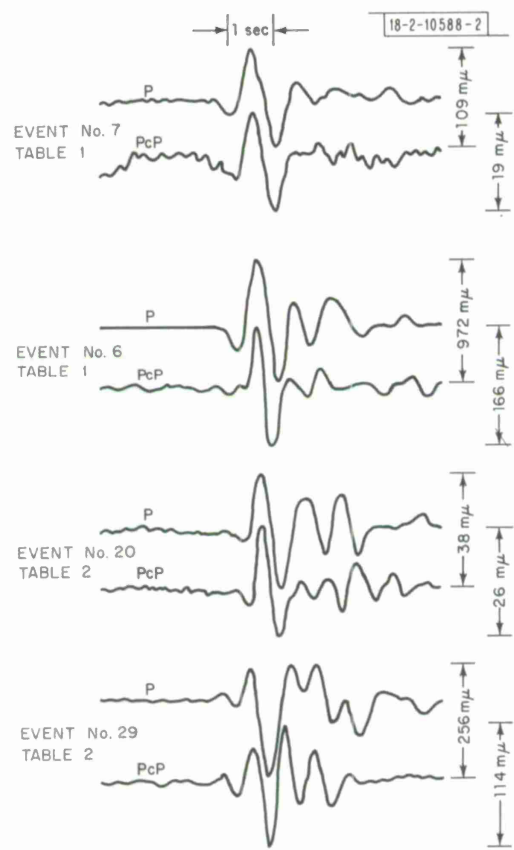
Fig. VI-1. Steered LASA beams of P and PcP phases for 4 events. Amplitudes of P and PcP phases have been equalized to demonstrate the similarity of wave shape for each event.

97
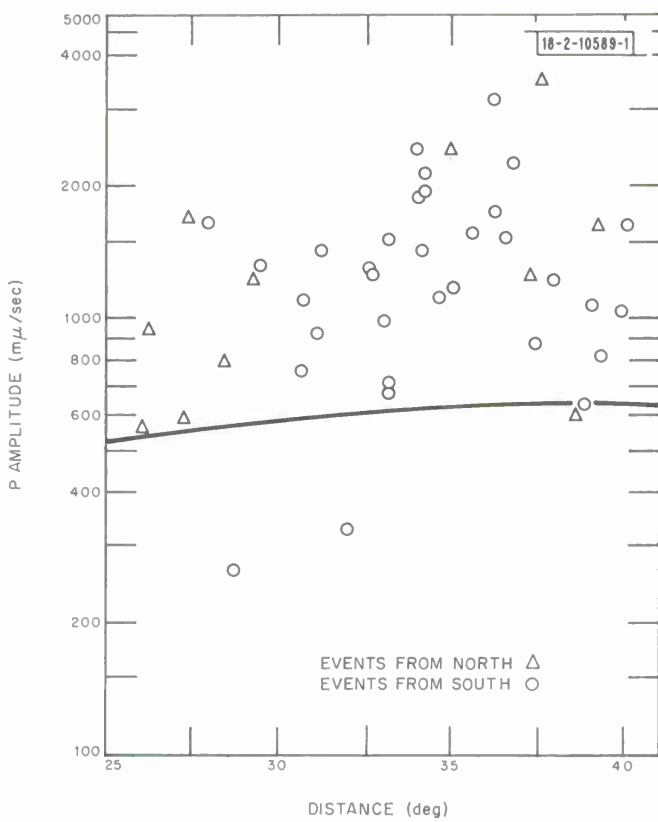
Fig. VI-2. Comparison of theoretical and observed P amplitudes (A/T), normalized to NOS magnitude 6.0. Theoretical curve (solid line) represents vertical component of displacement/period at surface after corrections for geometric spreading, attenuation and effect of free surface.
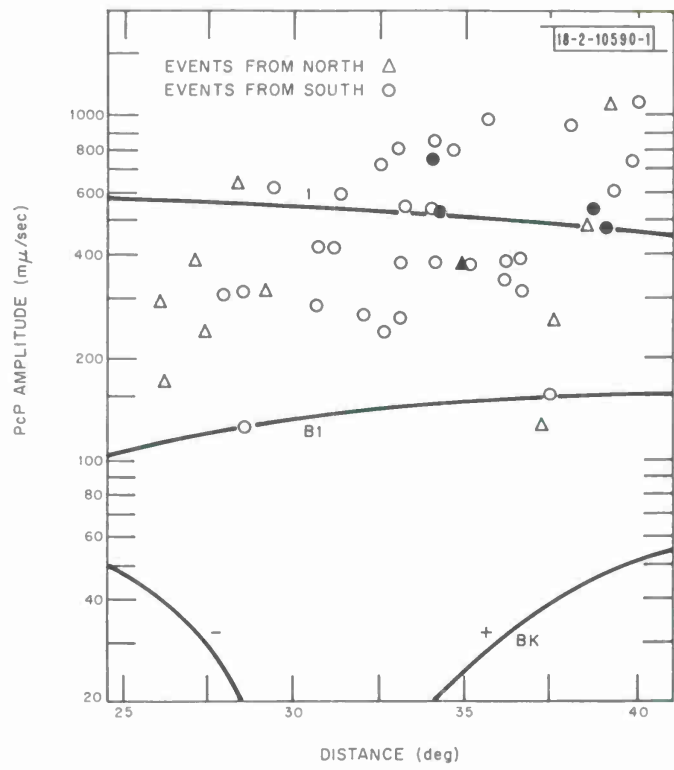
Fig. VI-3. Comparison of theoretical and observed PcP amplitudes (A/T) normalized to NOS magnitude 6.0. Curve 1 is for unit reflection coefficient at core-mantle boundary, curves B1 and BK are for core-mantle models of Bullen and Haddon (1967) and Buchbinder (1968). Negative sign on BK curve implies a reversed polarity of PcP from P. Solid symbols indicate observed PcP phases with opposite polarity to P.
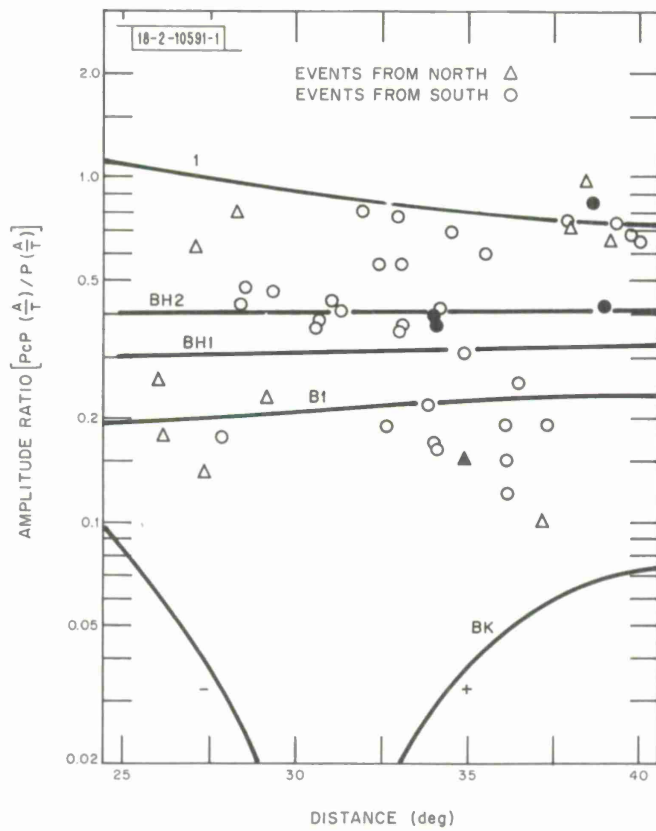
Fig. VI-4. Comparison of theoretical and observed PcP/P amplitude ratios. Curves 1, B1, and BK are for the same models described in Fig. VI-3. Also shown are two modified B1 models, curves BH1 and BH2, with parameters given in the text.
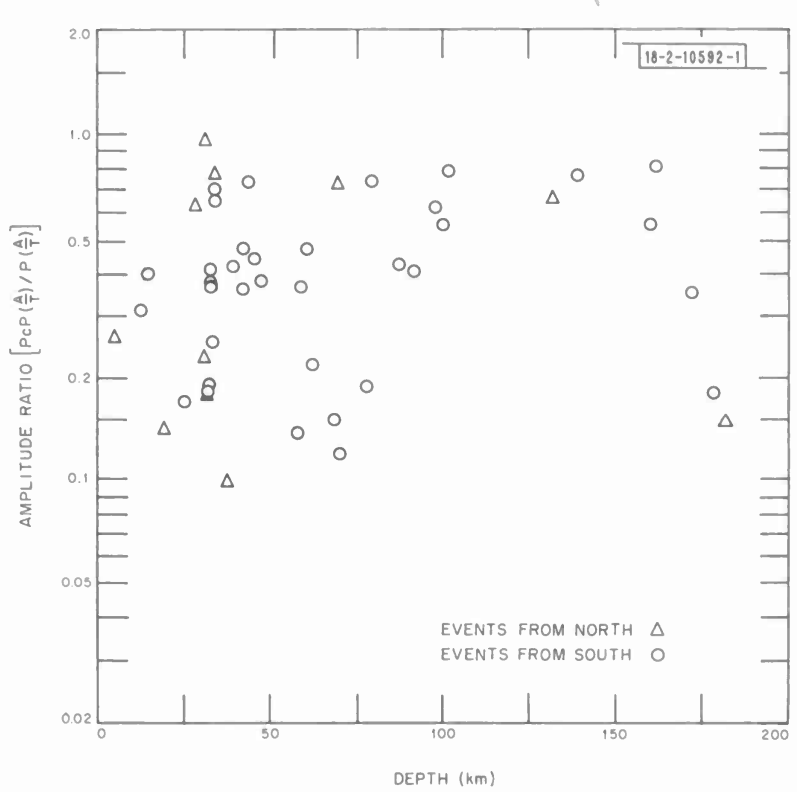
Fig. VI-5.   PcP/P ratios plotted against depth of focus.
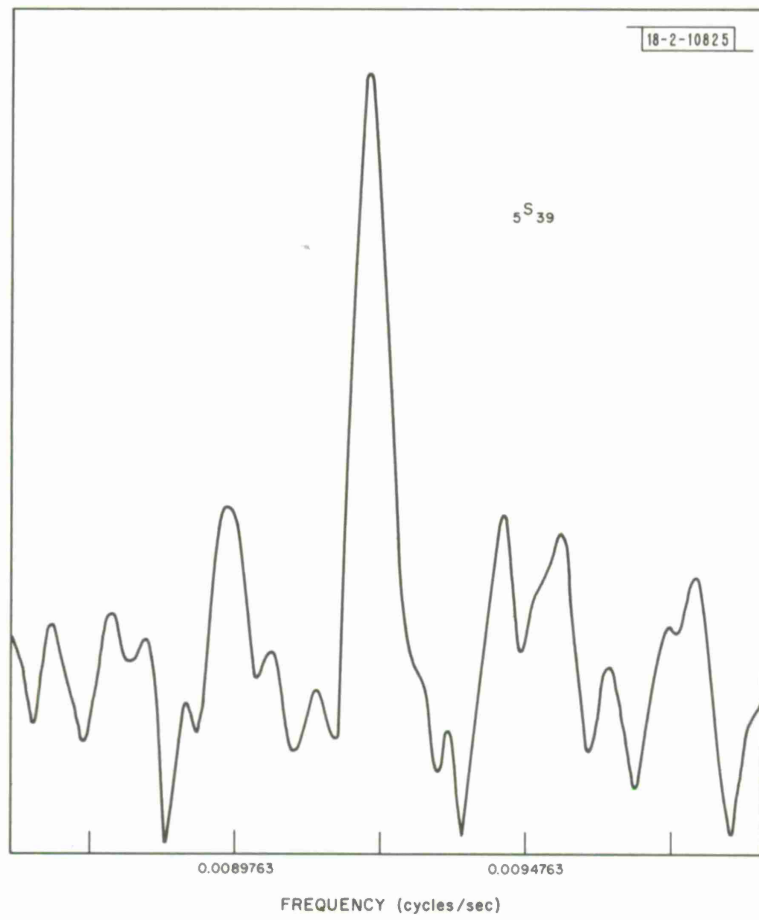
Fig. VI-6. Result of application of excitation criterion to identify $_5S_{39}$ mode on colatitudinal component.
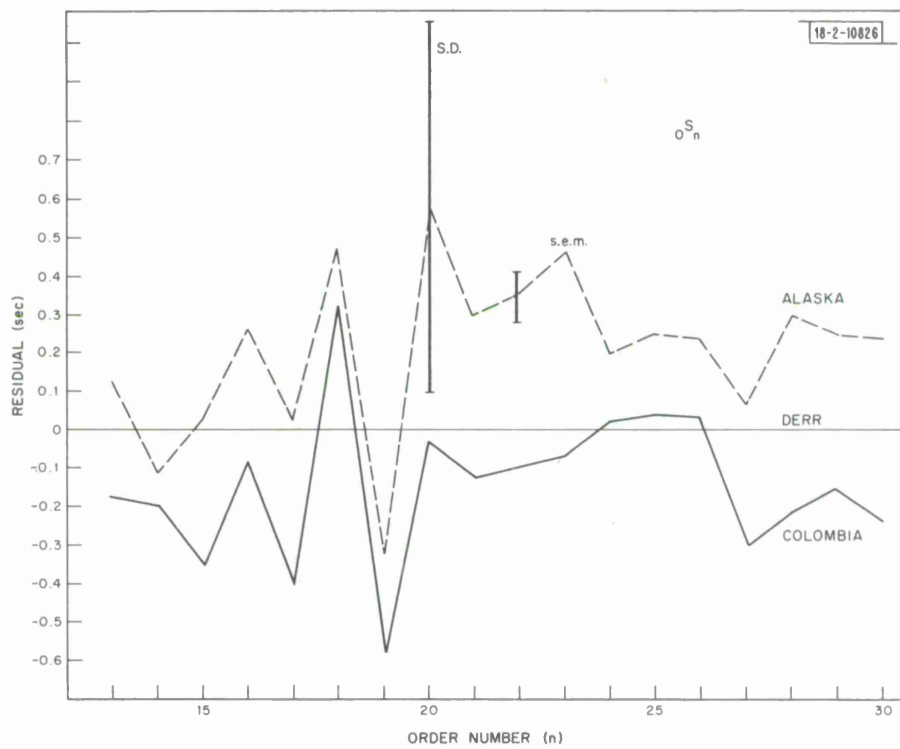
Fig. VI-7. Fundamental spheroidal modes $_0S_n$. Difference between eigenperiods measured for Alaskan[11] and Colombian earthquakes and average eigenperiods published by Derr.[12] S. D. and s.e.m. indicate standard deviation and standard error of the mean found for Alaskan earthquake measurements.
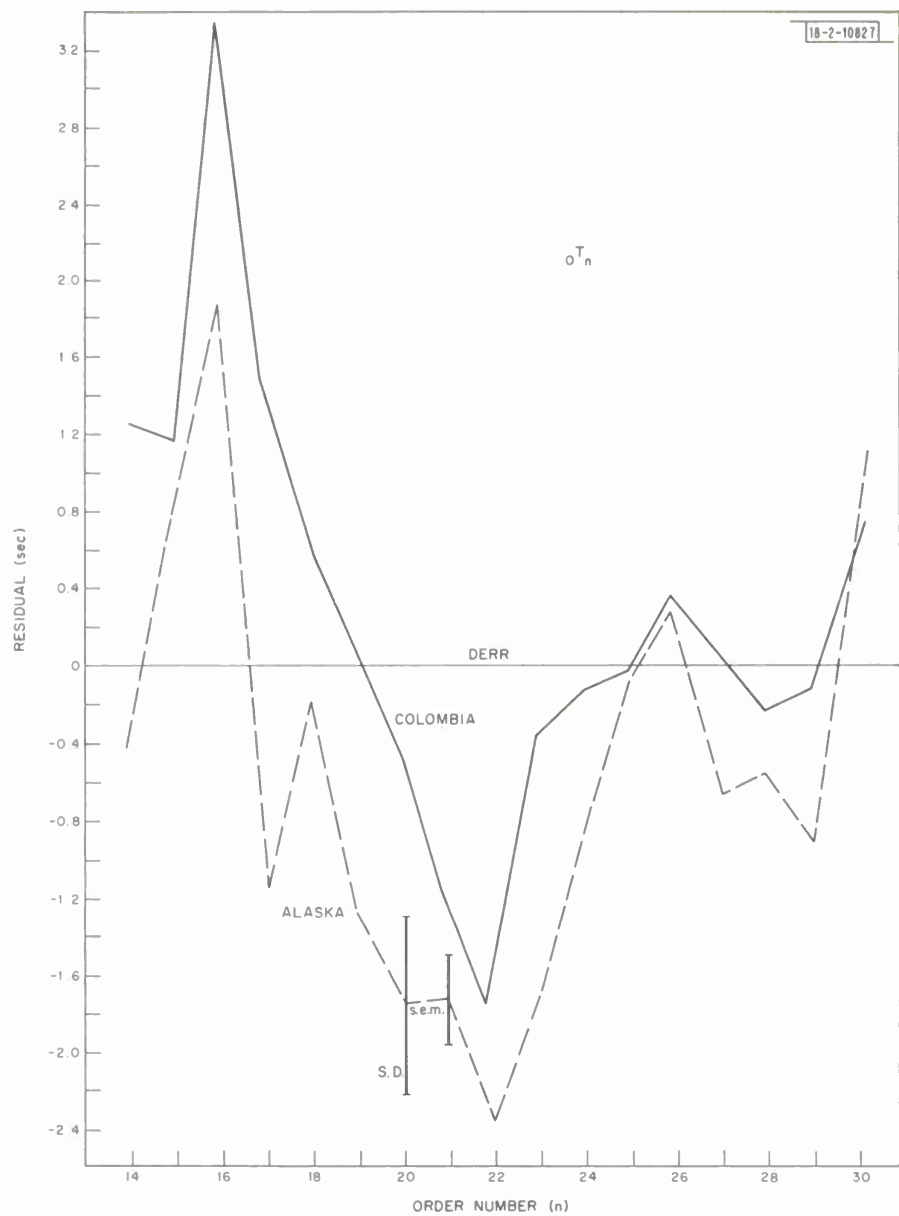
Fig. VI-8. Fundamental torsional modes $_0T_n$ (see Fig. VI-7 caption).

DOCUMENT CONTROL DATA – R&D

(Security classification of title, body of abstract and indexing annotation must be entered when the overall report is classified)

1. ORIGINATING ACTIVITY (Corporate author)	2a. REPORT SECURITY CLASSIFICATION
Lincoln Laboratory, M.I.T.	Unclassified
	2b. GROUP None

3. REPORT TITLE

Seismic Discrimination

4. DESCRIPTIVE NOTES *(Type of report and inclusive dates)*

Semiannual Technical Summary Report — 1 July through 31 December 1972

5. AUTHOR(S) *(Last name, first name, initial)*

Davies, David

6. REPORT DATE	7a. TOTAL NO. OF PAGES	7b. NO. OF REFS
31 December 1972	114	66

8a. CONTRACT OR GRANT NO. F19628-73-C-0002 AF 49(638)-1763	9a. ORIGINATOR'S REPORT NUMBER(S) Semiannual Technical Summary, 31 December 1972
b. PROJECT NO. ARPA Order 512	9b. OTHER REPORT NO(S) (Any other numbers that may be assigned this report)
c. d.	ESD-TR-72-354

10. AVAILABILITY/LIMITATION NOTICES

Approved for public release: distribution unlimited.

11. SUPPLEMENTARY NOTES	12. SPONSORING MILITARY ACTIVITY
None	Advanced Research Projects Agency, Department of Defense

13. ABSTRACT

Studies of new array data are reported, with particular emphasis on the array NORSAR. Models for approach angle anomalies at LASA are presented. Further evidence for deep mantle lateral heterogeneity is given. Detailed analyses have been made of earthquakes in Eurasia. A microbarographic noise study has been completed. Continued progress is reported in the bulletin production from the month of intensive seismic analysis.

14. KEY WORDS

seismic discrimination seismic array	LASA NORSAR